NORTHWESTERN UNIVERSITY

Rat Whisker Mechanics for Neuroscience and Bio-Inspired Sensors

A DISSERTATION

SUBMITTED TO THE GRADUATE SCHOOL

IN PARTIAL FULFILLMENT OF THE REQUIREMENTS

for the degree

DOCTOR OF PHILOSOPHY

Field of Mechanical Engineering

By

Anne En-Tzu Yang

EVANSTON, ILLINOIS

September 2018

ABSTRACT

Rat Whisker Mechanics for Neuroscience and Bio-Inspired Sensors

Anne En-Tzu Yang

Research on rat whiskers offers knowledge in neuroscience analogous to humans' sense of touch and inspiration for efficient sensing robotics. The present work investigates the rat whisker system from a mechanical engineering perspective. First, key quasi-static and dynamic properties were quantified in Chapter 2 for individual whiskers in an array, which were modeled as tapered cones and based on their anatomic and geometric properties. Second, integrating an existing mechanical model with careful coordinate transformations, simulations of two experiments were conducted. Chapter 3 details evidence that single whiskers contain sufficient mechanical information for localization, as a result of their characteristic whisking kinematics. The results aligned with behavioral experimental observations. Chapter 4 of this work computes the whisker's mechanical responses to piezoelectric stimuli and successfully predicts the neural responses in primary afferents temporally associated with the stimuli during electro-physiological experiments. The predictions also lay an important groundwork for continued investigations in the dynamics of follicles and mechanoreceptors. Finally, inspired by the principles of whisker neuro-mechanics, a robotic sensor incorporating a biological ("real") rat whisker is featured in Chapter 5. The sensor is capable of sensing tactile and airflow magnitudes and directions in four axes. The whisker sensor possesses great potential as a soft, bio-inspired electronic whisker ("e-whisker") for haptic technology as well as health monitoring. The sensor also provides true-to-scale biomimetics, which is directly translatable to the mechanics of whiskers in biological systems.

Acknowledgements

I thank my advisor, Dr. Mitra Hartmann, for leading me into the interdisciplinary research of rat whiskers and for supervising me throughout the course of my PhD. Working with her and the group in the collaborative and encouraging environment she cultivated has made tremendously positive impact on my career development. I also learned a lot from her great measure of creativity and empathy.

I thank my committee members for their guidance along my way. Specifically, I thank Dr. Sarah Bergbreiter for hosting me for a month of visiting research and continuing sharing her expertise for our micro sensor work. I thank Dr. Ed Colgate for introducing me to human haptics and human subject experiments and willingly offering career advice and industry connections. I thank Dr. John Rudnicki for an enjoyable TAing experience and many helpful discussions on beam mechanics and vibrations.

I thank my mentors Sharon Wen for suggesting pursuing a PhD and Dr. Andrew Wo and Dr. Jyh-Jone Lee for providing pointers and letters of recommendation.

I thank my senior and fellow lab members– Dr. Chris Schroeder, Dr. Jen Hobbs, Dr. Lucie Huet, Dr. Matt Graff, Dr. Hayley Belli, Dr. Yan Yu, Chris Bresee, Nick Bush– for their depth and breadth of knowledge and all the good memories with "WAFLL" and the inflatable palm tree. I especially thank Lucie and Hayley for being the most supportive and caring colleagues I could ask for. I also thank Dr. Anastasia Mavrommati for being my school buddy for five years.

I thank my friends from Taiwan who are now scattered around the world but manage to stay in close touch and sustain me even during my terminal year– NuNu Chen, Ruby Lee, Ann Hsiao, Wei-En Wang, Wei-En Cheng, I-Yun Chen, Biing-Chwen Chang, Dr. Hua-Yi Hsu.

I thank my friends from GCF with whom I developed and maintained a solid focus throughout this journey– Dr. Steve Lee, Dr. Yuki Ohigashi, Dr. Esther Liu, Dr. Janet Bourne, Dr. Lauren Sturdy, Lois

Lin, Dr. Lindsay Oakley, Nayo Hill, Miranda So, Dr. Heather Zupancic, Vienet Romero, Nancy Jiang. Special thanks to Lindsay for her professional and thoughtful editorial support.

I thank Josh for cheering me on from the other side of the world with his inspirational work ethic, thoughtful encouragement, and geeky conversations.

Most importantly, I thank my family for always being there for me, though scattered in three different time zones around the world. I thank my parents for bringing me up, ingraining me with a firm foundation of true identity and a deep sense of intrinsic worth, and letting me go $\sim$8000 miles away from home for this degree. Their abundant love and constant prayer are my greatest treasure.

Table of Contents

ABSTRACT 3

Acknowledgements 4

Table of Contents 6

List of Tables 12

List of Figures 13

Chapter 1. Introduction 16

1.1. Motivation 16

1.2. Contributions 18

1.2.1. The quantification of individual whisker mechanical properties 18

1.2.2. The implementation of mechanical modeling in laboratory coordinates 19

1.2.3. The design and fabrication of a tactile and airflow sensor using biological whiskers 19

Chapter 2. Variations in vibrissal mechanical properties across the rat mystacial pad 22

Abstract 22

New and Noteworthy 23

2.1. Introduction 23

2.2. Methods 25

2.2.1. Data collection and data reduction 25

2.2.2. Mechanical properties of a hollow, tapered whisker 29

2.2.2.1. Mass moment of inertia as a function of whisker geometry 30

2.2.2.2. Area moment of inertia at the whisker base 31

2.2.2.3. The vertical deflection of the whisker under the influence of gravity reflects a tradeoff between whisker mass and stiffness 32

2.3. Results 36

2.3.1. The importance of mechanical properties to the study of rat whiskers 36

2.3.2. Density varies along the whisker length 38

2.3.3. Mechanical advantages conferred by the medulla 41

2.3.4. The intrinsic curvature of the whisker has a much larger influence on I_{Mass} than does variation in whisker slope 44

2.3.5. Variations in mechanical parameters across the vibrissal array 46

2.4. discussion 49

2.4.1. Advantages of the whisker morphology over hypothetical alternatives 49

2.4.2. Center of mass and radius of gyration 50

2.4.3. Summary and future work 51

Acknowledgments 53

Chapter 3. Whisking kinematics enables object localization in head-centered coordinates based on tactile information from a single vibrissa 54

Abstract 54

3.1. Introduction 55

3.2. Materials and Methods 57

3.2.1. Position and orientation of the head and the pegs surrounding the head 57

3.2.2. Simulating whisking kinematics 57

3.2.3. Choice of protraction amplitude 61

3.2.4. Coordinate systems: whisker-centered vs. head centered coordinates 62

3.2.5. Computing mechanical signals as the whisker protracts against a peg 64

3.2.6. The average minimum distance as metric to quantify the resolution of the mappings 65

3.3. Results 67

3.3.1. Mechanical signals at the whisker base in whisker-centered coordinates vary with the pegs location in head-centered coordinates 67

3.3.2. Bending magnitude and direction vary with peg location for all whiskers 68

3.3.3. Most whiskers show unique mappings 69

3.3.4. Both elevation and roll contribute to the uniqueness and the resolution of the mappings 72

3.3.5. Localization of a peg using a row vs. a column of whiskers 75

3.4. Discussions 78

3.4.1. Cues for orienting to an object 78

3.4.2. Potential mechanisms for neural coding 79

3.4.3. Effects of variable whisking kinematics and friction 80

3.4.4. The effects of head pitch and 3D mappings in whisker-centered coordinates 81

Acknowledgments 83

Chapter 4. Response characteristics of identified primary afferents in the rat vibrissal system 84

4.1. Introduction 84

4.2. Results 87

4.2.1. The morphology of four types of mechanoreceptors in the vibrissal follicle 87

4.2.2. Intra-axonal labeling and recording of primary afferents 88

4.2.3. The angular tuning of the neural response cannot be explained solely by the location of the nerve endings within the follicle 92

4.2.4. The simplest mechanoreceptor model: an overview 95

4.2.5. Simulated responses are a good match to experimental data across all axons 99

4.2.6. The anatomy associated with the differential mechanics of RS-Merkel and lanceolate responses 103

4.2.7. Confirming the importance of vibrissa curvature 105

4.3. Discussion 108

4.3.1. Associating receptor type with response profile 108
4.3.1.1. Lanceolate endings 108
4.3.1.2. Merkel endings 109
4.3.2. The importance of 3D vibrissal geometry 109
4.3.3. Advantages and limitations of the simple spring-mass-damper model 111
4.3.4. The vibrissal system offers unique advantages for the study of mechanoreceptor responses 112
Author Contributions 113
Acknowledgments 113
Supplemental Figures 114
4.4. SUPPLEMENTAL EXPERIMENTAL PROCEDURES 115
4.4.1. Data analysis 115
4.4.2. Simulating the piezoelectric displacement of the vibrissa 116
4.4.3. Mechanoreceptor models 118
4.4.3.1. Accounting for the angular location of mechanoreceptors 118
4.4.3.2. Optimizing simulated response magnitudes (finding the weights for Eq. 4.1 119
4.4.3.3. Optimizing simulated response latencies (finding m, c, k, for Eq. 4.2) 120

Chapter 5. Contact-resistive sensing of touch and airflow using a rat whisker 122
5.1. Introduction 122
5.2. Methods 124
5.2.1. Materials preparation 124
5.2.2. Mechanical simulation on sensor deformation 125
5.2.3. Fabrication 125
5.2.4. Whisker attachment 126
5.2.5. Voltage divider for contact resistive sensing 127
5.3. Results 127

5.3.1. Geometry and contact quality 127
5.3.2. Tactile signals and bending moment conversion 129
5.3.3. Response to airflow 133
5.4. Discussions 135
5.5. Conclusions 136
Acknowledgment 136

Chapter 6. Summary and Future Outlooks 137
6.1. Summary 137
6.2. Future outlooks 138
6.2.1. Future work on mechanical properties 138
6.2.2. Future work on head-centered localization 138
6.2.3. Future work on mechanoreceptor mechanics 138
6.2.4. Future work on whisker sensor 139
Conclusion 140

References 141

Appendix A. Method of superposition for mass moment of inertia (straight, taper cones with zero tip diameter, two slopes, and a hollow proximal portion) 150
A.1. General expression for I_{Mass} of a cone rotating about the vertical axis at it base, and rotating about the vertical axis at a distance L from its base 152
A.2. Calculating I_{Mass} for the four imaginary whisker sections 153
A.3. Superposition of I_{Mass} of the four imaginary whisker sections to compute I_{Mass} for each of the three whisker shapes shown in Results 154

Appendix B. Method of integral for mass moment of inertia (curved, tapered cones with zero tip diameter and one slope) for all three Cartesian axes. 156
B.1. Assumptions of the calculation 156

B.2. Dividing the whisker into disks and calculating the I_Mass of each 157

B.3. Additional steps to set up the integral of disks over the whole whisker length 159

B.4. Integrating unit cross-sectional I_{Mass} over the entire whisker 160

B.5. Convergence of a whiskers two mass moments of inertia (I_{Mass}) derived using two different approaches 161

Appendix C. Beam bending of a Maltese cross subject to a concentrated load under different boundary conditions 162

C.1. Background 162

C.2. Clamped on one end 163

C.3. Clamped on both ends 164

C.4. Comparison between two boundary conditions 165

C.5. Conclusion 166

List of Tables

2.1	Measured and computed whisker variables.	26
2.2	Whisker parameters used in the present study.	27
2.3	Whisker mass did not vary significantly up to 15 days post-cutting.	28
2.4	Equations used to compute the geometry of all whiskers in the array.	42
2.5	Effect of the medulla on the mechanical properties of the whisker.	43
3.1	Equations used to simulate whisking kinematics.	60
3.2	Number of pegs reached and the percent of mapping that is unique	72
3.3	The effect of elevation and roll on the number of pegs reached and the mapping resolution.	75

List of Figures

1.1 The outline of the dissertation encompassing main contributions 18

1.2 The number of publications associated with relevant keywords 20

2.1 A schematic of the structural elements of the whisker 25

2.2 Computing whisker deflection under its own weight, including the effects of different proximal and distal slopes 30

2.3 Variability between proximal and distal densities and its effect on whiskers center of mass 39

2.4 Comparison of actual whisker morphology to two alternative hypothetical geometries 42

2.5 Effects of curvature and nonlinear slope on the whiskers mass moment of inertia 46

2.6 Mechanical and material properties as a function of whisker identity 47

3.1 Coordinate systems, variables, and parameters used in the simulations 58

3.2 2D intuition for head-centered and whisker-centered coordinate systems. 63

3.3 Mechanical signals vary with the (x,y) location of contact. 68

3.4 Magnitude and direction of bending moment at the whisker base after a 5° rotation against pegs placed at different (x, y) locations relative to the rats head. 70

3.5 Mappings for the Column-2 whiskers are generally unique, typical of all whiskers of the array. 71

3.6 Mappings between bending magnitude and direction (M_B, M_D) and peg location (x,y) as whisking kinematics are altered. 73

3.7	Mechanical signals within rows and columns of whiskers.	77
4.1	Bulk tracer injections reveal mechanoreceptor morphology and location within the follicle	87
4.2	Representative axons and endings	89
4.3	Response properties of primary afferents when the whisker is deflected in the afferents best direction	90
4.4	Correlation between location of endings and preferred angle	93
4.5	Axons exhibit a diversity of angular tuning profiles	94
4.6	Geometry and mechanics of the present modeling of vibrissae in the array	97
4.7	Simulation results compared to experiment in detail	100
4.8	Summary plots showing simulated responses closely matching experimental data.	101
4.9	Ultrastructure of RS-Merkel and lanceolate endings	104
4.10	Effect of modifying vibrissa shape	107
4.11	Angular tuning curves for the 21 primary afferents recorded in the present study are shown as “radar plots”	114
4.12	Simulation of piezoelectric displacement of the vibrissa	117
4.13	Models of mechanoreceptors	118
5.1	The inspiration and design of the sensor	124
5.2	The fabrication flow chart of the sensor.	126
5.3	An illustration accompanying beam theory derivation	128
5.4	FEM simulation results explain the choice of sensor geometry	130
5.5	The three- and four-axis versions of the sensors were fabricated and tested	132
5.6	A single axis responds to an airflow of constant and varying airspeeds.	134

6.1	Preliminary data from capacitive sensing	139
A.1	Calculation of mass moment of inertia using superposition	151
B.1	Calculation of mass moment of inertia using integral	157
C.1	Abaqus output of maximum principle strain (ϵ_{max}) of a Maltese cross under axial force	165
C.2	Strains as a function of x-location under two different assumptions.	166
C.3	Deflections as a function of x-location under two different assumptions.	166

CHAPTER 1

Introduction

1.1. Motivation

Quantifying the input to the neural pathway of the rat has been of interest in neuroscience for a long history. Dating back as far as 1909, when a study on the sensory control in the rat was published (Richardson, 1909), rat whiskers (vibrissae) have long been a model system for neuroscientists to investigate how the brain processes the sense of touch. Rat whiskers are preferable for such investigation because it has relatively simply structural components. In addition, the neural pathway originating from the mechanoreceptors within the follicle at the base of a rat whisker is highly analogous to the neural pathway from the mechanoreceptors under the skin of human hands. Therefore, knowledge of the neural pathway of rat whiskers would inform understanding of the neural pathway of human hands. When investigating rat whiskers, neuroscientists seek to answer "How is the mechanical input to the pathway translated into the electrical output?" or, more generically, "How does the rat obtain information about its surroundings based on the neural activities resulting from the mechanics at the base of its whiskers?" Despite the continued effort of engineering approaches, one of the biggest challenges in this field of research remains to be reliable quantification of the mechanics occurring at the whisker base– the very first stage of the signal transmission along the neural pathway.

In the discipline of robotics, knowledge of rat whisker mechanics is also crucial when designing bio-inspired tactile sensors. Tactile sensors have been of increasing importance to roboticists, especially since excellent sensing capability is an essential step towards safety around robots. Rat whiskers offer an inspiration for efficient tactile sensing. However, successful constructions of bio-mimicking sensors require profound understanding of the underlying mechanical principles in biological systems.

The in-depth mechanical modeling presented in this work highlights the important contributions mechanical engineering can make to research on rat whiskers. Moreover, the mechanical perspective drives collaborative, inter-disciplinary efforts in neuroscience and robotics. Proper implementations of mechanics leads to a deeper understanding of the excellence of animal sensing capability and its reproduction in the form of novel robotic devices.

Employing the fundamentals of mechanics, the two aims driving the this dissertation are as follows:

- The quantification of the early-stage inputs to the neural pathway of the rat's tactile sensing
- The design and signal acquisition and interpretation of tactile sensors

Meeting the aims led to three important contributions detailed in the following section.

1.2. Contributions

The primary contributions of this dissertation are:

(1) The quantification of individual whisker mechanical properties (*"rat whisker mechanics"* in Fig. 1.1; Chapter 2).

(2) The implementation of mechanical modeling in laboratory coordinates (*"behavioral neuroscience"* and *"neurophysiology"* in Fig. 1.1; Chapters 3 and 4).

(3) The design and fabrication of a tactile and airflow sensor using biological whiskers (*"sensing"* in Fig. 1.1; Chapter 5).

These contributions together showcase that advancement in the disciplines of neuroscience and robotics is highly interconnected and mutually inspirational.

1.2.1. The quantification of individual whisker mechanical properties

Similar to how humans have five fingers, canonically, rats have 31 whiskers arranged as an arrays on each side of their face. Each array contains whiskers of different sizes, aspect ratios, and orientations.

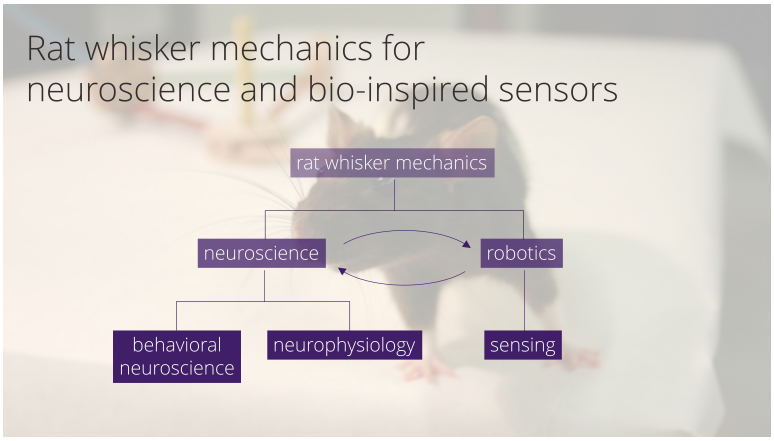

Figure 1.1. The outline of the dissertation encompassing main contributions
The fundamentals of rat whisker mechanics were applied to two disciplines– neuroscience and robotics. Particularly, this dissertation encapsulates such applications in the context of three projects. From a broader viewpoint, this work exemplifies that neuroscience inspires robotics, and that robotics advances knowledge in neuroscience. The background of this figure is photographed by Lucie A. Huet.

During active sensing behaviors, rats rhythmically move their whiskers back and forth at approximately 5 to 12 Hz. This characteristic motion is called "whisking". There are a few striking aspects of whisking. First, whiskers only have receptors (called "mechanoreceptors") within the follicle which is embedded under the skin (Ebara et al., 2002). In other words, whiskers are merely simple hairs with no sensors anywhere along their lengths. Second, these mechanoreceptors have no proprioception (i.e. the rats have no information for the position and orientation of its whisker, follicle, and receptors). However, the rats are still able to acquire information about their surroundings. The perceived sophistication underlying mechanical signal transmission and the spatial information translation make the whisker system especially worth investigating.

Whiskers have a unique geometry, often characterized by its taper and curvature. Moreover, when quantifying the mechanics of each whisker, it is essential to account for the effect of its intrinsic, individual geometry. Chapter 2 of this dissertation quantifies critical mechanical properties associated with whisking and shows the variation of these properties across different whiskers within the array. Particularly, the calculation of mass moment of inertia is reported for taper beams with curvature or piecewise slope variation.

1.2.2. The implementation of mechanical modeling in laboratory coordinates

Numerical simulations of isolated whiskers have been widely implemented. However, it is non-trivial to simulate the mechanics in laboratory frame, in which rats actively explore and/or electro-physiology experiments are performed. In chapters 3 and 4, mechanical signals calculated for isolated whiskers were integrated into laboratory (global) frame through coordinate transformations to simulate mechanics for whiskers undergoing active whisks and passive displacements, respectively.

1.2.3. The design and fabrication of a tactile and airflow sensor using biological whiskers

There have been a growing number of whisker-themed bio-inspired sensors published in recent decades (see the middle and right panels in Fig. 1.2). Typically, the whisker sensors developed by groups in the rat whisker community are at scales significantly larger than the size of the rat.

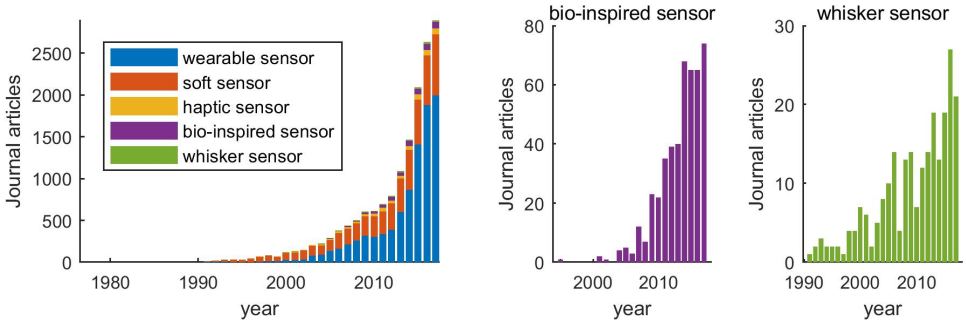

Figure 1.2. The number of publications associated with relevant keywords
Publication counts on a stacked bar plot *(left)* and individual bar plots *(right)*. Results are generated by *Web of Science (https://webofknowledge.com/)* using these keywords for "topic" searches.

Even outside of the rat whisker research community, researchers in soft electronics and micro-electro-mechanical systems have published sensing devices resembling whiskers. Particularly, the resemblance between these devices and rat whiskers are in the following aspects:

- at the same scale of rat whiskers (approximately from 10 μm to 10 mm scale).
- with the main sensing feature perpendicular (or flexible enough to become perpendicular) to the surface it is mounted to
- for the sensing of tactile signals (in some cases, in addition to other sensing capabilities)

Harada et al. (2014) developed a fully-printed "e-whisker" (electronic whisker) for strain and temperature sensing. Strain is reflected on the change in resistance of a conductive material made from carbon nanotube and silver nanoparticles. When the e-whisker undergoes a strain, the distance between nanoparticles changes, causing a detectable change in resistance. The greatest dimension of these e-whiskers is about 1 cm.

In a similar structure but with different materials, the e-whisker designed by Hua et al., (2016) uses paper as the flexible material and graphite from pencil trace as the conductive. In this case, positive and negative strains induce cracks and overlaps between graphite flakes, leading to change increase and decrease in resistance, respectively. These e-whiskers are approximately $5 \times 20mm$ in width and length.

Quite differently, Zhang et al., (2016) fabricated a cobalt-based ferromagnetic sensor which features array of hair-like structure (microwires). The array senses force-induced displacements in the form of

electrical potential, which changes with the configuration of two current-filled microwires (serving as coils for magnetic flux). The length of each wire is about 2 mm.

Most recently, Reeder et al., (2018) published shape memory polymer based whisker sensing arrays that is also capable of sensing temperature and strain. Gold strain gages are patterned on the polymer to enable changes in resistance with strain. Each whisker is about 1 mm long.

The above four publications illustrate the latest development on whisker sensors at the actual scale of a real whisker. They also stress the significant role whisker sensors potentially play in wearable, health-monitoring technologies. However, to the best of our knowledge, none of the currently published works features a "real" rat whisker.

The work in Chapter 5 complements this area of research with the design and fabrication of a sensor made specifically to work with biological rat whiskers. The sensor thus benefits from the unique geometric and material properties that a rat whisker possesses. Furthermore, experiments conducted using a micro-sensor tailored for a "real" rat whisker has the advantage of reflecting the mechanical properties and sensor behaviors of a whisker on a living rat. The sensor is also wearable, soft, and haptic, all of which are traits of growing importance, as observed in the rising number of publications over the past several decades (left panel in Fig. 1.2).

Lastly, another example demonstrating the importance of knowledge of mechanics in sensor design is described in Appendix C for the readers' interest. In some of the large-scale whiskers, a Maltese cross design is often implemented to transmit mechanical signals. However, previous work placed little emphasis on how the mechanics of the Maltese cross affects the strain gage signals. The derivation in the appendix is based on beam bending theory and should be kept in mind when fabricating robotic whiskers of this kind as it will strongly alter the signals processed.

CHAPTER 2

Variations in vibrissal mechanical properties across the rat mystacial pad

A version of this chapter has been submitted to the Journal of Neurophysiology and is currently in review as "Yang AET, Belli HM, and Hartmann MJZ (in review) Variations in vibrissal mechanical properties across the rat mystacial pad."

Abstract

Recent work has quantified the geometric parameters of individual rat vibrissae (whiskers) and developed equations that describe how these parameters vary as a function of row and column position across the array. This characterization included a detailed quantification of whisker base diameter and arc length, as well as the geometry of the whisker medulla. The present study now uses these equations for whisker geometry to quantify several properties of the whisker that govern its mechanical behavior. We first show that the average density of a whisker is lower in its proximal region than in its distal region. This density variation appears to be largely attributable to the presence of the whisker cortex, rather than to the presence of the medulla. The density variation has very little effect on the whiskers center of mass. We next show that the presence of the medulla decreases the whiskers deflection under its own weight and also decreases its mass moment of inertia, while sacrificing less than 1% stiffness at the whisker base when compared to a solid whisker. Finally, we quantify two dimensionless parameters across the array. First, the *deflection to length ratio* decreases from caudal to rostral: caudal whiskers are longer but deflect more under their own weight. Second, the *non-dimensionalized radius of gyration* is approximately constant across the array, which may simplify control of whisking by the intrinsic muscles.

We anticipate that future work will exploit the mechanical properties computed in the present study to improve simulations of the mechanosensory signals associated with vibrissotactile exploratory behavior.

New and Noteworthy

The mechanical signals transmitted by a whisker depend critically on its geometry. We used detailed measurements of whisker geometry and mass to derive equations for the whiskers center of mass, mass moment of inertia, radius of gyration, and deflection under gravity. The whiskers geometry helps reduce the amount it deflects under its own weight while maximizing its length, and reduces the energy required to whisk at a given rotational velocity while increasing stiffness at the whisker base.

2.1. Introduction

During tactile exploratory behavior, rats often oscillate their vibrissae (whiskers) back and forth at frequencies between 5 and 25 Hz in a behavior known as "whisking" (Berg and Kleinfeld 2003; Vincent 1912; Welker 1964; Wineski 1983). Using only mechanical information from its whiskers, a rat can determine an objects size, orientation, and texture (Brecht et al. 1997; Carvell and Simons 1990; Guicrobles et al. 1989; Polley et al. 2005). The rat vibrissal-trigeminal system has therefore become an important model for the study of active sensing, that is, for investigating the effects of movement and mechanics on the sensory data received (Bosman et al. 2011; Bush et al. 2016b).

The mechanical signals transmitted during whisking behavior depend critically on whisker geometry. In a recent study, we quantified whisker geometry as a function of the row and column position within the array, including arc length, base diameter, medulla geometry, radius ratio, and radius slope (Belli et al. 2017). This geometry will affect the whiskers quasi-static bending as well as its dynamic response (Hartmann 2015; Lucianna et al. 2016).

The whiskers quasi-static bending governs the mechanosensory signals that the rat will obtain as the whiskers deform when they press against objects (Birdwell et al. 2007; Hires et al. 2013; Hires et al. 2016; Huet and Hartmann 2016; Huet et al. 2015; Kaneko et al. 1998; Kim and Moller 2007; Quist and Hartmann 2012; Solomon and Hartmann 2006; Solomon and Hartmann 2010; 2011; Ueno et

al. 1998; Yang and Hartmann 2016). Under quasi-static assumptions, in which the effects of time and inertia are irrelevant, only the geometry of the whisker and its elastic properties (Youngs modulus and Poissons ratio) influence how an external force is transmitted to the vibrissal base. In other words, a whiskers quasi-static response to an external input depends solely on its geometry and elastic (material) properties.

In contrast, the whiskers dynamic response refers to the mechanosensory signals governed by its mass and inertia in response to force, torque, or change in state (Boubenec et al. 2012; Kan et al. 2013; Quist et al. 2014). Whisker dynamics are especially important when quantifying non-contact whisking, the collision generated at the instant the whisker contacts an object, and whisker vibrations. A whiskers dynamic response depends not only on its geometry and elastic properties, but also on its inertial properties, which characterize its mass distribution.

In the present work, we use the equations for average whisker geometry developed in Belli et al. (2017) along with mass measurements to quantify several mechanical properties of the whiskers. An important motivation for the present study is to lay the groundwork for future simulations that will require accurate descriptions of how whisker mechanical parameters vary across the array. In addition, we specifically tested the hypotheses that the whisker geometry would 1) minimize the deflection of the whisker under its own weight while maximizing whisker length, and 2) minimize the amount of energy required to whisk at a given rotational velocity, while increasing stiffness at the whisker base.

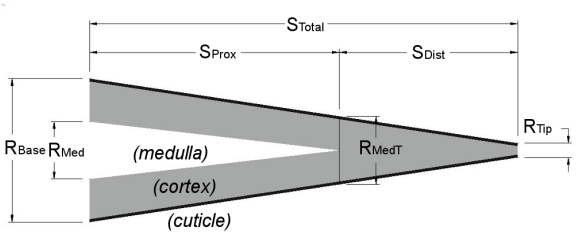

Figure 2.1. A schematic of the structural elements of the whisker
The whisker is modeled with base radius R_{Base} and tip radius R_{Tip}. The medulla is defined as a hollow cone with negligible tip diameter. The radius of the medulla at its base is denoted by R_{Med}, and the radius of the whisker at medulla termination point, R_{MedT}. The total whisker arc length (S_{Total}) can be broken into proximal(S_{Prox}), occupied by the medulla , and distal (S_{Dist}). Note that the schematic is not to scale.

2.2. Methods

All procedures involving animals were approved in advance by the Animal Care and Use Committee of Northwestern University.

2.2.1. Data collection and data reduction

The parameters used in the present study are depicted in Fig. 2.1 and are listed in Table 2.1.

Data analysis began with the 52 whiskers whose parameters are shown in Table 2.2. These are the same 52 whiskers of *reduced Dataset 2* in *Table 4* of Belli et al. (2017). Data collection procedures have been described in detail previously (Belli et al. 2017), but briefly, whiskers were obtained from the left and right arrays of three male and female Sprague-Dawley rats (Charles River SD, #400) with ages between 3 and 13 months. All whiskers were obtained by cutting the whisker near its base instead of plucking the whisker from the follicle, ensuring that the portion of the whisker internal to the follicle was not included in the mass measurement.

All whiskers were massed using a Mettler-Toledo UMX2 microbalance (0.1 μg resolution) within two to three hours after cutting to prevent dehydration. To test for any possible effects of dehydration, we performed a control experiment in which eight whiskers were massed within an hour after cutting and then re-massed 3, 8, 12, and 15 days later. Whiskers were stored in folded aluminum foil, which were then stored in a plastic freezer bag with a zipper. Results, shown in Table 2.3, indicate that dehydration

Table 2.1. Measured and computed whisker variables.

Measured variables	
Variable name	Description
D_{Base}	Diameter of the whisker at its base
D_{Tip}	Diameter of the whisker at its tip
D_{MedT}	Diameter of the whisker at where the medulla terminates
D_{Med}	Diameter of the medulla at its base
$D_{Med_Tip} \equiv 0$	Diameter of the medulla at its tip is defined to be zero
S_{Total}	Total arc length of the whisker
S_{Prox}	Arc length of the whisker proximal to medulla termination
S_{Dist}	Arc length of the whisker distal to medulla termination
M_{Total}	Total mass of the whisker
M_{Prox}	Mass of the whisker proximal to medulla termination
M_{Dist}	Mass of the whisker distal to medulla termination
Calculated variables	
Variable name	Description
$R_{Base} \equiv D_{Base}/2$	Radius of the whisker at its base
$R_{Tip} \equiv D_{Tip}/2$	Radius of the whisker at its tip
$R_{MedT} \equiv D_{MedT}/2$	Radius of the whisker at medulla terminating location
$R_{Med} \equiv D_{Med}/2$	Radius of the medulla at its base
$Slope_R \equiv (R_{Base} - R_{Tip})/S_{Total}$	Radius slope
S_{Extend}	Extended length of the proximal whisker
V_{Total}	Volume of the whisker
V_{Prox}	Volume of the whisker proximal to medulla termination
V_{Dist}	Volume of the whisker distal to medulla termination
V_{Med}	Volume of the whisker medulla
$\rho_{Total} \equiv M_{Total}/V_{Total}$	Average density of the entire whisker
$\rho_{Prox} \equiv M_{Prox}/V_{Prox}$	Average density of the whisker proximal to S_{Prox}
$\rho_{Dist} \equiv M_{Dist}/V_{Dist}$	Average density of the whisker distal to S_{Prox}
$\rho \equiv M_{Total}/(V_{Total} - V_{Med})$	Density of the cortex and cuticle, excluding the medulla
I_{Area}	Area moment of inertia
I_{Mass}	Mass moment of inertia

did not have a significant effect on the mass of the whisker when we compared the mass 15 days after cutting to the mass 1 hour after trimming (two-sided, Wilcoxon Signed-Rank Test, $p < 0.11$). Note that these results may not would generalize to all storing conditions in all laboratories.

After massing, the 52 whiskers were scanned on a flatbed scanner at 1200 dpi (Epson Perfection 4180 Photo) and imaged under a light microscope (Olympus BX60) to obtain measurements of whisker geometry including the medulla. The whisker was cut in two at the location where the medulla terminated and both proximal and distal segments were re-massed within 24-48 hours and re-scanned to estimate the arc length of each segment.

Table 2.2. Whisker parameters used in the present study.

Rat	Sex	Side	ID	D_{Base}	D_{Med}	D_{MedT}	$_{DTip}$	S_{Total}	S_{Prox}	S_{Dist}	M_{Total}	M_{Prox}	M_{Dist}
1	F	R	A1	139	49	45	5	37.5	25.8	11.7	246.2	229.9	16.3
1	F	R	A2	104	12	45	12	28.7	21	7.7	128.3	115.6	12.7
1	F	R	A3	85	14	51	3	19.9	8.5	11.4	60	46.6	13.4
1	F	R	B1	160	54	43	6	46.9	32.9	14	361.4	348.5	12.9
1	F	R	B2	73	17	48	5	19.6	7.7	11.9	239.7	225.9	13.8
1	F	R	C1	163	44	39	4	50.4	38	12.4	426.5	417	9.5
1	F	R	C2	166	56	43	4	35.2	25	10.2	283.1	274.3	8.8
1	F	R	C3	125	33	50	5	23.2	13.2	10	120.2	109.6	10.6
1	F	R	C4	100	24	64	3	15.6	6	9.6	58.8	44.2	14.6
1	F	R	C6	53	11	49	5	4.2	4.1	0.1	NaN	NaN	NaN
1	F	R	D1	205	71	38	5	56.5	45.9	10.6	NaN	638.1	NaN
1	F	R	D2	178	74	45	7	37.4	27.3	10.1	339.9	329.7	10.2
1	F	R	D4	107	35	58	14	14.4	7.1	7.3	66.9	53.9	13
1	F	R	E1	213	84	38	8	49.6	42.4	7.2	634.1	628.3	5.8
1	F	R	E3	174	68	37	9	25.6	19.8	5.8	NaN	216.4	NaN
1	F	R	E4	134	52	52	5	17	9.9	7.1	97.1	89	8.1
1	F	R	א	145	43	43	6	47	31.2	15.8	274.9	261.3	13.6
1	F	R	β	161	45	43	6	40.3	38.9	1.4	424.2	410.8	13.4
1	F	R	γ	158	54	43	4	51	39.1	11.9	NaN	374.2	NaN
2	M	R	A1	143	44	29	4	43.9	34.9	9	292.9	287.3	5.6
2	M	R	A3	95	26	44	3	21.9	12	9.9	76.4	67.3	9.1
2	M	R	A4	75	11	55	19	12	4.8	7.2	39	25.1	13.9
2	M	R	B1	163	60	40	5	52	42.3	9.7	466.7	459.1	7.6
2	M	R	B2	148	51	37	7	36.6	28.4	8.2	265.5	260	5.5
2	M	R	B3	89	24	47	3	19.2	10.6	8.6	62	53.4	8.6
2	M	R	B4	81	10	62	3	13.1	4.3	8.8	40.6	25.8	14.8
2	M	R	C2	159	52	40	4	36.5	28	8.5	327.6	320.5	7.1
2	M	R	C3	115	29	38	3	19.9	13.7	6.2	96.3	91.5	4.8
2	M	R	C4	101	16	53	4	15	7.6	7.4	63.5	54.1	9.4
2	M	R	D1	203	68	34	4	52.1	45.6	6.5	675.4	671.2	4.2
2	M	R	D5	105	22	60	4	12.9	5.9	7	54.9	44.4	10.5
2	M	R	E3	151	58	39	4	26.6	21	5.6	207.3	202.6	4.7
2	M	R	E4	132	47	45	4	18.5	12.5	6	112.3	106.5	5.8
2	M	R	E5	93	31	55	3	10.9	5.2	5.7	39	31.7	7.3
2	M	R	α	154	47	39	4	50.3	40.8	9.5	379.9	372.5	7.4
2	M	R	β	134	40	38	7	45.1	36.3	8.8	251.4	243.7	7.7
2	M	R	γ	134	44	41	4	49.7	41.3	8.4	375.3	368.1	7.2
2	M	R	δ	101	25	41	6	35.8	28.2	7.6	170.8	164.1	6.7
3	M	L	A1	154	60	39	6	41.7	30.3	11.4	277.1	268.9	8.2
3	M	L	A4	76	16	48	5	13.9	6.4	7.5	39.5	32.1	7.4
3	M	L	B1	171	68	40	3	48.2	37.7	10.5	414.2	405.8	8.4
3	M	L	B2	153	50	38	5	35.3	26.1	9.2	239.3	233.7	5.6
3	M	L	B3	99	27	41	5	20.6	12.8	7.8	74.3	68.6	5.7
3	M	L	C2	167	56	40	3	36.6	27.7	8.9	307.9	301.5	6.4
3	M	L	C4	103	26	51	3	16.5	8.9	7.6	71.1	63.1	8
3	M	L	D3	134	57	41	6	24.9	18.3	6.6	150.2	145.6	4.6
3	M	L	D4	136	45	46	5	20.6	14.5	6.1	135.9	130.6	5.3
3	M	L	D6	81	18	65	4	8.6	2.9	5.7	23.6	14.3	9.3
3	M	L	E3	158	62	44	5	26.4	20.2	6.2	208	202.7	5.3
3	M	L	E6	92	15	59	3	6.4	3	3.4	26	19.9	6.1
3	M	L	α	160	48	48	3	44.9	37.1	7.8	343	334.5	8.5
3	M	L	β	171	53	38	5	54.9	49.6	5.3	477.7	470.7	7

(F, female; M, male; R, right; L, left) (The D's are in μm, S's are in mm, and M's are in μg)
Rows shaded gray indicate whiskers that were found to be outliers and removed from analysis (see text for details).

Table 2.3. Whisker mass did not vary significantly up to 15 days post-cutting.

Whisker identity	**Whisker mass (μg)**				
	1 hour	3 days	8 days	12 days	15 days
A1	127.1	127.5	127.8	126.5	127.5
B1	82.1	82.2	83.3	81.4	82.1
γ	381.7	381.5	380.2	379.2	380.5
C1	327.0	329.3	327.9	329.2	329.2
C3	87.2	86.9	87.1	87.1	86.5
δ	416.0	418.5	417.4	417.3	418.0
D2	105.5	105.6	104.3	104.8	104.6
Unknown	210.9	211.8	211.4	211.2	210.9

Four whisker segments were lost before they could be massed (indicated as NaNs in Table 2.2), leaving a total of 48 whiskers with complete parameter sets. These 48 whiskers were assessed for the presence of extreme outlier values. We searched for outliers in mass, base and tip diameters, arc length, volume, and average density. Extreme outliers were identified as any value more than three standard deviations from the mean.

We found two outlier whiskers for Rat 1: the B2 whisker was an outlier in proximal average density (10.1 mg/mm^3) and the β whisker was an outlier in distal average density (17.1mg/mm^3). The data for these two whiskers are shown in rows 5 and 18 of Table 2.2, which are highlighted gray and correspond to the same two rows of *Table 4* of Belli et al., 2017. These outliers almost certainly occurred due to human error when measuring the geometry of these particular whiskers. Compared with other whiskers with similar total arc lengths, the proximal arc length (S_{Prox}) for the B2 whisker and the distal arc length (S_{Dist}) for the β whisker were noticeably too short relative to their total arc lengths (S_{Total}). These two outlier whiskers were removed from analysis, yielding a final dataset of 46 whiskers with no missing observations or outliers.

All figures in the present work use this dataset of 46 whiskers. Of the 46 whiskers, 13 were from the right side of a female rat, 19 whiskers were from the right side of a male rat, and 14 whiskers were from the left side of a second male rat. The female rat was ∼13 months old and weighed ∼350 grams, and both male rats were ∼3 months old and weighed ∼300 grams.

2.2.2. Mechanical properties of a hollow, tapered whisker

The goal of the present work was to characterize how the geometric features of a vibrissa influence some of its mechanical properties and thus the signals that will be generated during active tactile sensing. We therefore computed several mechanical properties based on the experimentally-measured data, including the mass moment of inertia, the area moment of inertia at the whisker base, and the amount that the whisker deflects under its own weight

Assumptions about densities of the cuticle, cortex, and medulla: As indicated in Fig. 2.1, the whisker consists of the cortex, the cuticle, and the medulla. The cortex is densely packed with desiccated hair protein known as keratin. The cuticle is a thin layer of keratin surrounding and protecting the cortex. Recent work on human hair has shown that the cuticle contains β-keratin, while the cortex is composed of α-keratin (Stanic et al. 2015), and we expect that a similar difference between cuticle and cortex also holds for rodent vibrissae. However, the present work did not quantify the geometry of the cuticle separately from the cortex, and therefore the two materials are assumed to have the same density. The medulla is a porous, web-like structure in the proximal portion of the whisker that is filled with air pockets (Chernova 2003; Hausman 1930). Because the medulla has such a low density, it is often approximated as hollow (Adineh et al. 2015; Voges et al. 2012). We follow the convention of these previous studies in assuming that the medulla has negligible density in all calculations that follow.

Assumptions about proximal and distal slopes: Previous work in both mice (Hires et al. 2016) and rats (Belli et al. 2017) reported that the slope differs between the proximal and distal regions. The difference is indicated in the schematic of Fig. 2.1 and also further exemplified in Fig. 2.2A. In the rat, the proximal radius slope and average distal radius slope are statistically the same when averaged over all whiskers. However, when the ratio of proximal slope to distal slope was analyzed as a function of column, the majority of whiskers in columns 1 and 2 had proximal slopes greater than distal slopes, while the majority of whiskers in columns 3–6 and in the Greek column had proximal slopes smaller than distal slopes. These results are confirmed in Fig. 2.2B. We accounted for these differences in radius slope in the calculations that follow.

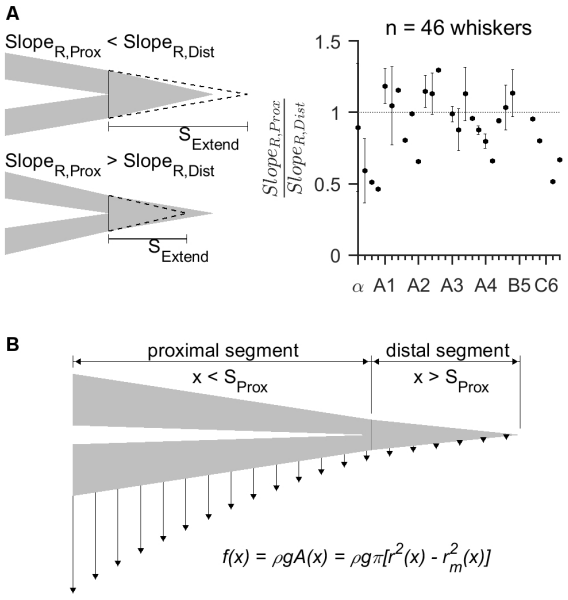

Figure 2.2. Computing whisker deflection under its own weight, including the effects of different proximal and distal slopes

(A) Ratio of proximal to distal radius slope. The whisker has a proximal region that contains a hollow medulla and a distal region that is solid. As illustrated in the schematic (not to scale), previous studies have found that the slope differs between the proximal and distal regions. Specifically, columns 1 and 2 tend to have the ratios of proximal to distal slope that are greater than one, compared with the rest of columns. The x-axis sorts whiskers by column and then by row within each column. **(B) Deflection of a tapered whisker with a medulla under its own weight.** Schematic is not to scale, and the cuticle is not shown for visual clarity. The outer cross-sectional radius of the whisker and the inner cross-sectional radius of the medulla are given by Eq. 2.4 and 2.5, respectively. We derived a function, $f(x)$, that describes the distributed load of the whisker resulting from its own weight. The black vertical vectors indicate this force per unit length. Vector magnitudes in the distal region decrease quadratically. In the proximal region, the decrease in vector magnitude is approximately quadratic, but not exactly due to the presence of the medulla.

2.2.2.1. Mass moment of inertia as a function of whisker geometry. The mass moment of inertia of the vibrissa (I_{Mass}) measures the whiskers resistance to rotation. We used the method of superposition to compute the mass moment of inertia for a straight whisker (Appendix A), and we used the method of integral to compute the mass moment of inertia for a whisker with intrinsic curvature (Appendix B).

As derived in Appendix A, the mass moment of inertia for a straight whisker is given by:

$$I_{Mass} = \frac{1}{60}\pi(3R_{Base}^4 S_{Extend} + 2R_{Base}^2 S_{Extend}^3 - 3R_{Med}^4 S_{Prox} - 2R_{Med}^2 S_{Prox}^3 + 3R_{MedT}^4 \quad (2.1)$$
$$(S_{Dist} - S_{Extend} + S_{Prox} + 2R_{MedT}^2 (S_{Dist} - S_{Extend} + S_{Prox})$$
$$(S_{Dist}^2 + S_{Extend}^2 + 3S_{Extend}S_{Prox} + 6S_{Prox}^2 + S_{Dist}(S_{Extend} + 4S_{Prox})))\rho$$

In Equation 2.1, R_{Base} is the radius at the whisker base, R_{Med} is the radius of the medulla at the whisker base, R_{MedT} is the radius of the whisker at the point of medulla termination, and ρ is the density of the whisker cortex.

The variable S_{Extend} allows us to account for the slope differences between proximal and distal regions. S_{Extend} is the extrapolated full length of the whisker had it retained the slope of its proximal portion for its full length. It is also illustrated in Fig. 2.2B. Appendix A explains the mathematical basis for S_{Extend} in further detail.

If the proximal and distal slopes of the whisker were the same, then $S_{Extend} \equiv S_{Prox} + S_{Dist}$, and Equation 2.1 simplifies to the following expression:

$$I_{Mass} = \frac{1}{60}\pi(-3R_{Med}^4 S_{Prox} - 2R_{Med}^2 S_{Prox}^3 + 3R_{Base}^4 S_{Total} + 2R_{Base}^2 S_{Total}^3) \quad (2.2)$$

It is worth emphasizing that in Equations 2.1 and 2.2, and throughout this entire study, the density ρ without a subscript denotes the material density of keratin that forms the whisker excluding the medulla. In other words, ρ represents the combined density of the cortex and cuticle. Later portions of this study will employ the variables ρ_{Total}, ρ_{Prox}, and ρ_{Dist}, which represent densities averaged over select regions of the whisker as defined in Table 2.1.

2.2.2.2. Area moment of inertia at the whisker base. The stiffness at the whisker base is given by the product of the cross-sectional area moment of inertia (I_{Area}) and Youngs modulus (E). For a given value of Youngs modulus, a larger area moment of inertia means that the whisker is more resistant to bending. Given the presence of the medulla at the whisker base, the area moment of inertia at the

whisker base (I_{Area}) can be described as (Hibbeler 2014):

$$I_{Area} = \frac{\pi}{4}(R_{Base}^4 - R_{Med}^4) \tag{2.3}$$

2.2.2.3. The vertical deflection of the whisker under the influence of gravity reflects a tradeoff between whisker mass and stiffness. Like any cantilever beam, a whiskers mass will cause it to deflect vertically ("droop") under the influence of gravity. The magnitude of vertical deflection reflects a tradeoff between the mass of the whisker and its stiffness. The deflection curve of the whisker is denoted by $v(x)$: it describes the vertical deflection at every position x along the whisker length. To derive the deflection curve, we first obtained an analytical expression for its second-order derivative. This equation was then numerically integrated twice to obtain the deflection curve, $v(x)$. Here we provide the derivation of the second-order derivative of the deflection curve.

Consistent with previous studies (Birdwell et al. 2007; Hires et al. 2013), we modeled the whisker as a straight, tapered cantilever beam. Although whiskers have intrinsic curvature (Ahissar and Knutsen 2008; Quist and Hartmann 2012; Towal et al. 2011), the principle of superposition allows us to add the amount of deflection to the amount of intrinsic curvature. Superposition is valid because the radius of curvature of the whisker is more than five times the maximum diameter of the whisker (Hibbeler 2014).

A schematic illustrating the distributed load involved in computing the deflection curve is shown in Fig. 2.2C. The cross-sectional radius of the whisker cortex (r) and inner radius occupied by the medulla (r_m) were written as functions of the distance (x) from the whisker base:

$$r(x) = \begin{cases} \frac{R_{MedT} - R_{Base}}{S_{Prox}} x + R_{Base}, x \leq S_{Prox} \\ \frac{R_{Tip} - R_{MedT}}{S_{Dist}}(x - S_{Prox}) + R_{MedT}, x \geq S_{Prox} \end{cases} \tag{2.4}$$

$$r_m(x) = \frac{-R_{Med}}{S_{Prox}} x + R_{Med} \tag{2.5}$$

To provide intuition for Equations 2.4and 2.5, we reiterate (see Table 2.1) that R_{MedT} is different from R_{Med}. R_{Med} is the base radius of the medulla. R_{MedT} is the outer radius of the whisker at the location where the medulla terminates.

Having developed expressions for the radius of the whisker and the radius of the medulla as functions of the longitudinal distance from whisker base, x, it follows that the cross-sectional area of the whisker cortex as a function of x, $A(x)$, is given by:

$$A(x) = \pi[r(x)^2 - r_m(x)^2] \tag{2.6}$$

Next, at each position (x) along its length, the whisker experiences a distributed load (f) due to its own weight (Fig. 2.2). The distributed load has dimensions of force per unit length. The expression for the distributed load was obtained by finding the weight of keratin in an infinitesimal cross-section of the whisker. This weight is the product of the density of keratin (ρ), the acceleration due to gravity (g), and the cross-sectional area (A) occupied by keratin at each position (x):

$$f(x) = \rho g A(x) = \rho g \pi[r(x)^2 - r_m(x)^2] \tag{2.7}$$

Given the expression for the distributed load, standard elastic beam bending equations can be used to compute the change in sheer force and bending moment (Hibbeler 2014). Specifically, the integral of the distributed load over the length of any segment of a beam yields the change in shear force, $F(x)$. The integral of shear force over the length of any segment of a beam yields the change in bending moment $M(x)$:

$$F(x) = \int f(x)dx \tag{2.8}$$

$$M(x) = \int F(x)dx = \int\int f(x)dxdx \tag{2.9}$$

For a thin beam, the moment $M(x)$ is related to the curvature $\kappa(x)$ of the whisker by:

$$\kappa(x) = \frac{M(x)}{EI(x)} \tag{2.10}$$

And for small angles, the curvature is the second derivative of the deflection curve:

$$v''(x) = \kappa(x) \tag{2.11}$$

So that

$$v''(x) = \frac{M(x)}{EI(x)} \tag{2.12}$$

It is important to note that I is a function of x, and it depends on the medulla:

$$I(x) = \frac{1}{4}\pi[r(x)^4 - r_m(x)]^4] \tag{2.13}$$

Note that $I(x)$ refers to the area moment of inertia at each location (x) along the length of the whisker. By contrast, I_{Area} (as defined in Equation 2.3) specifically refers to the area moment of inertia at the base of each whisker. In other words, I_{Area} is identical to $I(x)$ evaluated at the base of the whisker: $I_{Area} \equiv I(x)|_{x=0}$.

Substituting the bending moment (eq. 2.9) and area moment of inertia (eq. 2.13) into Equation 2.12 yields two second-order differential equations for v"(x). One equation is for the proximal region of the whisker, $v_{Prox}(x)$, and the second equation is for the distal region, $v_{Dist}(x)$.

We performed these substitutions using Wolfram Mathematica$^{\mathrm{TM}}$and found that for the proximal segment of the whisker ($x \leq S_{Prox}$) the second-order derivative of the deflection curve $v_{Prox}(x)$ is given by:

$$v''_{Prox}(x) = \frac{4\rho g S_{Prox}(-\frac{R_{Med}^2(S_{Prox}-x)^4}{4S_{Prox}^3} + \frac{S_{Prox}(R_{Base}+\frac{R_{MedT}-R_{Base})x}{S_{Prox}})^4}{4(R_{MedT}-R_{Base})^2})}{3E((R_{Base}+\frac{(R_{MedT}-R_{Base})x}{S_{Prox}})^4 - (R_{Med}-\frac{R_{Med}x}{S_{Prox}})^4)} \tag{2.14}$$

For the proximal segment, we assumed a clamped boundary condition at the whisker base (Bagdasarian et al. 2013), so that both the displacement and the slope of the whisker are zero at the base, i.e.,

$$v_{Prox}(0) = 0; \quad v'_{Prox}(0) = 0 \tag{2.15}$$

The second equation, also found using Mathematica$^{\mathrm{TM}}$, describes the distal portion of the whisker, where $x \geq S_{Prox}$, and is given by:

$$v_{Dist}(x)'' = \frac{\rho g S_{Dist}^2}{3E(R_{Tip} - R_{MedT})^2} \tag{2.16}$$

Two compatibility conditions were applied to solve for v_{Dist} because the displacement and slope at the termination point of the medulla ($x = S_{Prox}$) must be identical for both proximal and distal regions of the whisker:

$$v_{Dist}(S_{Prox}) = v_{Prox}(S_{Prox}); \quad v'_{Dist}(S_{Prox}) = v'_{Prox}(S_{Prox}) \tag{2.17}$$

Notice that this derivation shows that the curvature (i.e., the second-order derivative of the deflection curve) of the distal portion of the whisker is independent of the position x.

When integrated twice, Equations 2.14 and 2.16 yield the deflection curve $v(x)$ at every point along the whisker length. Equations 2.15 and 2.17 give the constants of integration. Although in theory Equations 2.14 and 2.16 could have been integrated analytically, these integrations were quite complicated; it was found easier to compute the integrals numerically using *ode45* in MATLAB$^{\mathrm{TM}}$.

Tip deflection (δ) is defined as the distance that the tip of the whisker is vertically displaced from its original position due to the weight of the whisker. The value of the tip deflection is found by evaluating the deflection curve at the location $x = S_{Total}$.

2.3. Results

2.3.1. The importance of mechanical properties to the study of rat whiskers

A whiskers material properties and mass distribution govern its mechanical properties, which dictate both its quasi-static bending and dynamic response. In this first section of Results, we describe how seven variables of interest relate to whisking behavior. We specifically consider the center of mass, mass moment of inertia, radius of gyration, area moment of inertia, and tip deflection, as well as two non-dimensionalized variables: the normalized radius of gyration and the ratio of tip deflection to arc length.

Variables with dimensions

(1) The center of mass (CoM) of a whisker is a point in space whose location is determined by the distribution of mass along the whiskers length. It is the theoretical point at which all the distributed mass should be placed in order to retain the same response to an external force. In theory, if an external force acted on the whisker at its center of mass, the whisker would translate only in the direction of the applied force and would not rotate. The CoM has dimensions of length.

(2) The mass moment of inertia of a whisker (I_{Mass}) directly determines *(a)* the torque required to generate a given angular acceleration and *(b)* the kinetic energy required to rotate at a given angular velocity. Both angular acceleration and angular velocity are important when describing non-contact whisking (i.e., the whiskers rotation in free-air). From an energy perspective, a low value of the mass moment of inertia is preferred, as it will reduce the kinetic energy and torque required for a given angular velocity and acceleration. I_{Mass} has the unit of $mass - length^2$ and it is only defined with respect to a particular axis of rotation.

In conditions such as non-contact whisking, when the whisker can be approximated as a rigid body (Knutsen et al. 2008; O'Connor et al. 2013; Quist et al. 2014), the product of I_{Mass} and the angular acceleration of the whisker yields the torque required to rotate the whisker: $\tau = I_{Mass}\alpha$. In addition, again assuming a rigid body approximation, the product of I_{Mass} and

the square of the rotational velocity ω yields the kinetic energy required to rotate the whisker: $KE = \frac{1}{2} I_{Mass} \omega^2$. The superposition approach for (I_{Mass}) are provided in Methods assuming a straight whisker. The integral approach, accounting for the intrinsic curvature of the whisker, is provided in Appendix B for all three Cartesian axes of rotation. All axes are defined with respect to the shape of the whisker and pass through the whisker base (see Appendix B).

(3) In some ways, the radius of gyration of a whisker (R_g) can be thought of as the rotational analog of the center of mass. Mathematically, the radius of gyration is equal to the square root of $I_{Mass}/Mass$, and it has dimensions of length. The radius of gyration is the theoretical point where all the distributed mass should be placed in order to retain the same rotational response to an external torque.

Unlike the CoM, which represents a specific point relative to a chosen origin, the radius of gyration is a scalar. R_g is a distance from a chosen axis of rotation but it has no directionality or absolute position in space. In the present study, the axis of rotation always passes through the base of the whisker.

(4) The area moment of inertia at the whisker base (I_{Area}) is directly related to the stiffness of the whisker, and therefore characterizes how much the whisker will bend in response to an imposed moment. For a given imposed moment, a whisker with greater bending stiffness will deflect less than one with smaller bending stiffness. As described in 2.2, the stiffness is the product of the Youngs modulus (E) and I_{Area} of the beam. Because the cross-sectional geometry of a whisker varies monotonically (and nearly linearly) from base to tip, the I_{Area} at the base is representative of the entire whisker.

(5) The deflection of a whisker under its own weight describes the vertical displacement of each node of the whisker under the influence of gravity. The tip deflection δ is the largest deflection for each whisker, which always takes place at its tip. From a behavioral standpoint, minimizing tip deflection is preferred, in order to maximize the whiskers horizontal "reach".

Dimensionless variables

(6) The normalized radius of gyration (R_{gN}) effectively describes a tradeoff between a whiskers arc length and its radius of gyration. Both quantities have dimensions of length, so the ratio is non-dimensional (R_{gN}/S_{Total}).

Particular to the present study, the normalized radius of gyration is important because whiskers have high aspect ratios (arc length to base diameter), such that the radius of gyration is primarily determined by the arc length. As a result, and as will be further detailed in Section 2.3.5, if whiskers were all perfect, linearly-tapering cones with zero tip diameter, they would all have the exact same value of normalized radius of gyration. In other words, the normalized radius of gyration is how much the whisker deviates from a perfect cone. Whiskers are not perfect cones because of the presence of the medulla and the slightly-nonlinear slopes (Hires et al. 2016).

(7) Finally, the deflection-to-length ratio (δ/S_{Total}) is calculated by dividing the tip deflection by the arc length of the whisker. This ratio reflects tradeoffs in the rat's sensing volume compared to the energy required for whisking. Increased tip deflection decreases the sensing volume. Theoretically, tip deflections can be reduced either by shortening the whisker or by increasing base diameter (which will increase mass). Thus, δ/S_{Total} directly assesses the extent to which each whisker in the array trades off increases in mass in order to attain an increase in sensing volume.

2.3.2. Density varies along the whisker length

Both the cuticle and the near-hollow medulla contribute to a non-uniform distribution of keratin material throughout the whisker (Fig. 2.1). To quantify the variability in mass distribution along the whisker length, we calculated the average density of both the proximal and distal portions of the whisker (Fig. 2.3A). These densities are the variables ρ_{Prox} and ρ_{Dist} in Table 2.1. As expected, the average density is significantly higher in the distal region than in the proximal region (paired, two-sided Wilcoxon Signed Rank Test, $p < 0.001$). The average proximal density is $1.26 \pm 0.16 mg/mm^3 (mean \pm std)$ with a median

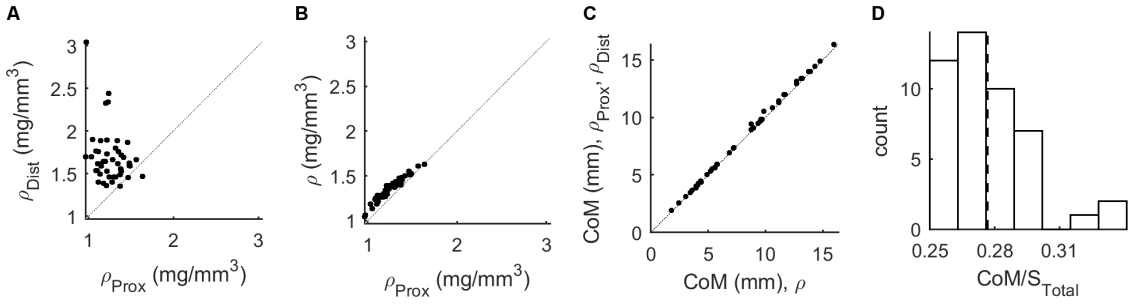

Figure 2.3. Variability between proximal and distal densities and its effect on whiskers center of mass

(A) The density of the distal portion of the whisker (ρ_{Dist}) is greater than the average density of the proximal portion (ρ_{Prox}). **(B)** The material density (ρ) is the density of the cortex and cuticle only, and is only slightly greater than ρ_{Prox}. When compared with panel (A), it is clear that the medulla is not the primary factor that explains why ρ_{Dist} is greater than ρ_{Prox}. **(C)** Due to differences in the density distribution, the whiskers center of mass (CoM) is on average $\sim 2.1\%$ more distal than it would have been if the mass had been uniformly distributed. Curvature is neglected in this analysis but would not change these results. **(D)** As expected, the center of mass as a fraction of whisker length is close to the theoretical value for a perfect cone, 0.25. The mean (0.277) is marked by a thick dashed line. .

of $1.23 mg/mm^3$, and the average distal density is $1.69 \pm 0.31 mg/mm^3 (mean \pm std)$ with a median of $1.62 mg/mm^3$.

For comparison, the average density for the entire whisker is $1.28 \pm 0.16 mg/mm^3 (mean \pm std)$ with a median of $1.26 mg/mm^3$. The average density for the entire whisker was computed assuming the whisker volume as the sum of the proximal and distal volumes, thereby accounting for the slight difference in radius slope observed between the whiskers proximal and distal regions in *Figure 6A* in Belli et al., 2017,

Two factors are likely to contribute to the difference between proximal and distal densities shown in Fig. 2.3A. First, the presence of the medulla will decrease the average density in the proximal region. Second, the area fraction (and hence the volume fraction) of the whisker occupied by the cuticle increases substantially from proximal to distal (Quist et al. 2011). The cuticle occupies up to 60% of the most distal regions of the whisker (Quist et al. 2011). Given that the cuticle is likely to be of a different material (β-keratin) than the cortex (α-keratin) (Stanic et al. 2015), it seems likely that the cuticle contributes significantly to density variations along the whisker length.

To disambiguate the contributions of these two factors, we computed the material density (ρ) of the entire whisker and compared it with the density of the distal region. By definition (Table 2.1), the material

density ρ is computed after subtracting out the volume of the medulla. In other words, ρ is the density of the cortex and cuticle only. The material density was found to be $1.36 \pm 0.13 mg/mm^3 (mean \pm std)$ with a median of $1.38 mg/mm^3$.

When the material density is plotted versus the proximal density (Fig. 2.3B) all points lie just barely above the identity line, indicating that the effect of the medulla is small (paired, two-sided Wilcoxon Signed Rank Test, $p < 0.001$). Comparing Fig. 2.3B with Fig. 2.3A further shows that the material density is typically smaller than the distal density, confirming that the presence of the medulla has only a limited effect on the density of the entire whisker. Thus the changes in density along the whisker length can be attributed primarily to the change in volume fraction occupied by the cuticle.

Although the average whisker density is considerably greater in the whisker distal region than in the proximal portion, this non-uniformity has very little effect on the whiskers center of mass. This result is shown in Fig. 2.3C, which compares the center of mass computed using the material density with that computed using different average densities for the proximal and distal regions of the whisker. When averaged across all 46 whiskers, the center of mass shifted only 2.106% closer to the distal end of the whisker than if the average density had been uniform (paired, two-sided Wilcoxon Signed Rank Test, $p < 0.001$). Note that this analysis holds equally well for curved whiskers as for straight whiskers: straight whiskers can be thought of as a special case of curved whiskers with zero curvature. In other words, the center of mass will change significantly with whisker curvature. However, for a whisker of a given curvature, density variations will have very little effect on the center of mass.

If a whisker were a perfectly straight, uniformly dense cone with tip diameter equal to zero, then by definition, its center of mass would always lie at a distance $d = S_{Total}/4$. The center of mass as a fraction of whisker arc length is shown in Fig. 2.3D for all 46 whiskers of the dataset. As expected, the whiskers exhibit greater scatter about the value 0.25 ($IQR = 0.0215$). The scatter results from four factors: the presence of the medulla, differences in density between cuticle and cortex, differences in slope between proximal and distal regions, and non-zero tip radius.

2.3.3. Mechanical advantages conferred by the medulla

Recall from the mechanical descriptions provided at the beginning of 2.3.1 reducing the whiskers mass moment of inertia (I_{Mass}) would decrease energy expenditure, but increasing the whiskers area moment of inertia (I_{Area}) would increase stiffness at the base, potentially improving signal transmission. We therefore hypothesized that the hollow medulla strikes a balance between decreasing the mass moment of inertia and increasing the area moment of inertia at the whisker base.

To investigate the potential mechanical advantages of the medulla, we compared the actual whisker geometry to two hypothetical whisker geometries, shown in Fig. 2.4. The "filled medulla" case assumes that the space occupied by the medulla is filled with keratin, just like the whisker cortex. In this scenario, the mass of the whisker increases but the outer dimensions of the whisker remain constant.

The "reduced volume" case assumes that the total amount of keratin of the whisker remains the same but is distributed closer to the whiskers central axis. Intuitively, this case corresponds to "squashing" the medulla by bringing the sides of the whisker towards the central axis. In this scenario, the mass of the whisker stays constant, but its volume decreases and its geometry changes. The new base radius, R_3, is given by the expression:

$$R_3 = \frac{1}{2}(\sqrt{(2R_{Base} + R_{MedT})^2 - 4R_{Med}^2} - R_{MedT}) \tag{2.18}$$

Notice that for both the "filled medulla" and "reduced volume" cases, only the proximal portion of the whisker is affected; the geometry of the distal portion remains unchanged.

For each of the three cases shown in Fig. 2.4, we quantified four material and mechanical properties across all whiskers of the array: the whisker mass (M), the area moment of inertia at the base (I_{Area}), the deflection of the tip under the whiskers own weight (δ), and the mass moment of inertia (I_{Mass}) about the axis that passes through the whisker base, orthogonal to the long axis of the whisker. This axis is the whiskers primary axis of rotation during whisking behavior, so I_{Mass} is directly related to the torque and rotational kinetic energy required for whisking. The I_{Mass} calculation here assumes that

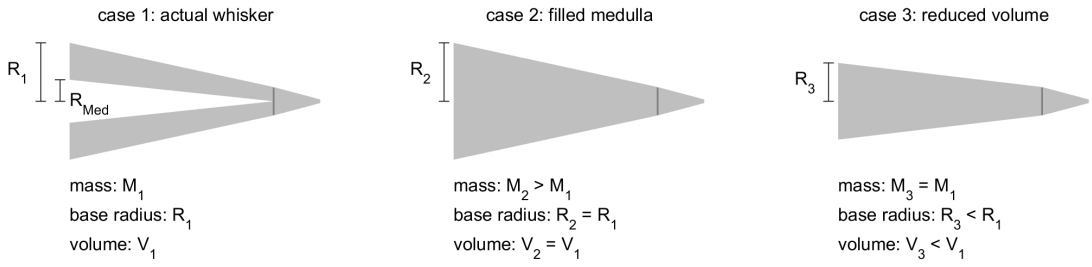

Figure 2.4. Comparison of actual whisker morphology to two alternative hypothetical geometries

Case 1 illustrates the actual whisker geometry. Case 2 has the same outer dimensions as case 1, but greater mass because the hollow medulla is now assumed to be solid keratin. Case 3 has the same mass as case 1, but the hollow medulla is "squashed" in the proximal region of the whisker. This compression reduces the proximal taper and the base diameter. For visual simplicity, the cuticle is not illustrated in any of the schematics.

Table 2.4. Equations used to compute the geometry of all whiskers in the array.

Variable	Equation
Arc length (S_{Total})	$43 + 1.8Row - 7.6Col, S_{Total} > 10mm$
Proximal arc length (S_{Prox})	$0.95S_{Total} - 7.3$
Base diameter (D_{Base})	$0.041 + 0.0020S_{Total} + 0.011Row - 0.0039Col$
Radius slope ($Slope_R$)	$0.0012 + 0.00017Row - 0.000066Col + 0.00011Col^2$
Medulla diameter (D_{Med})	$0.44D_{Base} - 0.019$
Tip diameter (D_{Tip})	Calculated from S_{Total}, D_{Base}, and $Slope_R$*
Medulla termination diameter (D_{MedT})	Calculated from $S_{Total}, S_{Prox}D_{Base}$, and $Slope_R$

*($D_{Tip} \equiv 0 if D_{Tip} < 0$)

whiskers have zero tip diameter, no intrinsic curvature, and that their proximal and distal regions have two distinct slopes.

In order to generalize the results of this analysis across the entire array, we used the equations of Belli et al. to determine the geometric parameters for each whisker based only on its row and column identity. These equations are listed in Table 2.4. Whiskers B5, C6, D6, and E6 were excluded from this analysis because their arc length was less than 10 mm and therefore violated the assumptions required to use these equations. For each of the remaining 27 whiskers, the quantities M,I_{Mass},I_{Area} and δ were calculated using the material density of the whisker found experimentally ($\delta = 1.36mg/mm^3$; Fig. 2.3B).

The mean and standard deviation for M,I_{Mass},I_{Area} and δ were computed over all 27 whiskers in the array for the three cases shown in Fig. 2.4. Results are shown in Table 2.5. Each row of Table 2.5 lists

Table 2.5. Effect of the medulla on the mechanical properties of the whisker.

Parameter	Unit	Filled medulla (case 2) relative to actual whisker (case 1)	Reduced volume (case 3) relative to actual whisker (case 1)
Mass (M)	mg	$\uparrow$ 5.67 $\pm$ 2.66% (worse)	no change
Mass moment of inertia (I_{Mass})	$mg \cdot mm^2$	$\uparrow$ 2.75 $\pm$ 1.81% (worse)	$\downarrow$ 0.69 $\pm$ 0.35% (better)
Area moment of inertia* (I_{Area})	mm^4	$\uparrow$ 0.69 $\pm$ 0.37% (better)	$\downarrow$ 12.44 $\pm$ 4.17% (worse)
Tip deflection (δ)	mm	$\uparrow$ 1.47 $\pm$ 1.05% (worse)	$\uparrow$ 11.70 $\pm$ 4.21% (worse)

(*at the base)
Four mechanical parameters are computed assuming two hypothetical geometries and compared with the same parameters computed using the actual whisker geometry. The average and standard deviation taken across all 27 whiskers are shown for each quantity. Relative to the actual whisker, the "filled medulla" (case 2) undesirably increases mass moment of inertia (I_{Mass}) and the amount of tip deflection under the whiskers own weight (δ), while increasing stiffness at the base (I_{Area}) by less than 1%. The "reduced volume" results in a slightly lower I_{Mass}, but at the cost of significantly decreasing I_{Area} and increasing δ). The assessments "worse" or "better" are based on energy considerations for Mass and Mass moment of inertia, based on stiffness considerations for Area moment of Inertia, and based on considerations of sensing volume for tip deflection.

the percent difference in these parameters for hypothetical cases 2 and 3 relative to case 1 (the actual whisker geometry) (all changes are with $p < 0.001$). This analysis answers questions such as: "When averaged across all whiskers in the array, by how much would I_{Mass} increase if the whiskers were entirely solid?"

For case 2, the first row of Table 2.5 immediately indicates that having a whisker medulla (case 1) is more advantageous than filling the medulla with keratin (case 2) because filling the medulla would increase the mass of the whisker on average by more than 5%. This increase in mass also inevitably increases I_{Mass} for case 2 compared to case 1, which would increase the amount of kinetic energy required to rotate the whisker. For case 3, the rows for M and I_{Mass} in Table 2.5 also show a slightly less intuitive result– although the mass of the whisker is identical between the reduced volume whisker (case 3) and the actual whisker, the mass moment of inertia (I_{Mass}) of case 3 is slightly smaller than I_{Mass} for the actual whisker (gray highlight in Table 2.5). This effect occurs because the mass is redistributed such that some of it is more proximal to the whisker base. In theory then, case 3 would decrease the rotational kinetic energy needed for whisking. This effect is very small, however (less than 1%), and its advantage is likely outweighed by the negative consequences for stiffness described next.

The area moment of inertia at the whisker base (third row of Table 2.5) is important because, along with Youngs modulus, it determines the whiskers bending stiffness at the base. If the base of the whisker is stiff, the same forces and moments will produce a smaller amount of deflection (curvature change). This difference in signal strength will affect the whiskers mechanical sensing resolution. The geometry of the filled medulla whisker (case 2) results in an area moment of inertia only slightly bigger than that of the actual whisker (case 1). The reduced volume whisker (case 3), on the other hand, has an area moment of inertia substantially smaller than that of the actual whisker (case 1). These results make excellent intuitive sense because by definition, area moment of inertia is proportional to the fourth power of the radius.

Finally, the last row of Table 2.5 illustrates that both the filled medulla whisker (case 2) and the reduced volume whisker (case 3) increase tip defection relative to the actual whisker geometry (case 1). Of the parameters discussed so far, tip deflection most clearly exposes the trade-off between two quantities whose desired values have opposite trends: it is desirable to minimize mass (and thus I_{Mass}) to reduce the energy required for whisking, while it is desirable for I_{Area} to be large to resist bending, preventing the whisker from "drooping", and to increase the signal strength at the whisker base. Comparing the magnitude of tip deflection across the three cases thus suggests that the actual whisker geometry (case 1) is superior to the alternative proposed geometries.

In summary, the hollow medulla strikes a balance between decreasing I_{Mass} and increasing I_{Area} at the whisker base. Although the actual geometry achieves only the second-highest bending stiffness (compare with case 2), it decreases M, I_{Mass}, and δ. Similarly, the actual whisker geometry has a slightly higher I_{Mass} than case 3, but this disadvantage is outweighed by the much larger increase in stiffness and decrease in tip deflection.

2.3.4. The intrinsic curvature of the whisker has a much larger influence on I_{Mass} than does variation in whisker slope

Real rodent whiskers are characterized by two salient geometric features: curvature (Knutsen et al., 2008; Towal et al., 2011) and non-linear slope (Hires et al. 2016). However, the analysis of the previous section,

including Table 2.5, uses the method of superposition to calculate I_{Mass} (Appendix A) that neglects intrinsic curvature. The calculation of Appendix A assumes a straight whisker with two distinct slopes in proximal and distal regions. Therefore, as shown in Appendix B, we also developed another approach using integral to compute I_{Mass} that accounts for intrinsic curvature and neglects slope differences. The two approaches (superposition and integral) converge for the case of a straight, single sloped whisker: the error between the two approaches is less than 0.0012% (see Appendix B).

To summarize, the superposition approach accounts for slope variations but not intrinsic curvature, while the disk integral approach accounts for intrinsic curvature but not slope variations. We used these two approaches to evaluate how each of the two geometric features– slope and curvature– affected I_{Mass}. Note that accounting for both slope variation and curvature simultaneously would require a purely numerical approach outside the scope of the present work. The I_{Mass} of whiskers for a straight, single-slope geometry calculated using the disk integral approach was used as the baseline standard for comparison. All calculations in this section were based on the experimental parameters shown in Table 2.2.

The change of I_{Mass} from baseline to a two-slope geometry (while maintaining zero curvature) is shown in in Fig. 2.5A. Accounting for two slopes causes I_{Mass} to increase for most but not all whiskers. The reason for this variability is that the radius slope could either decrease or increase from proximal to distal, depending on the individual whisker in the experimental data. For those whiskers whose distal slope is steeper than the proximal slope, accounting for two slopes "removes" material from the whisker and thus decreases I_{Mass}. In contrast, for those whiskers whose proximal slope is steeper than the distal slope, accounting for two slopes "adds" material from the whisker and thus increases I_{Mass}.

The change in I_{Mass} from baseline to a curved geometry (while maintaining a single slope) is shown in Fig. 2.5B. Accounting for curvature resulted in a decrease in I_{Mass} for all whiskers, without exception. This decrease is expected because I_{Mass} essentially quantifies the distance of the whiskers mass distribution from its axis of rotation. Because the whiskers intrinsic curvature causes it to curve towards its primary axis of rotation (at the whisker base), the value of I_{Mass} necessarily decreases as curvature increases.

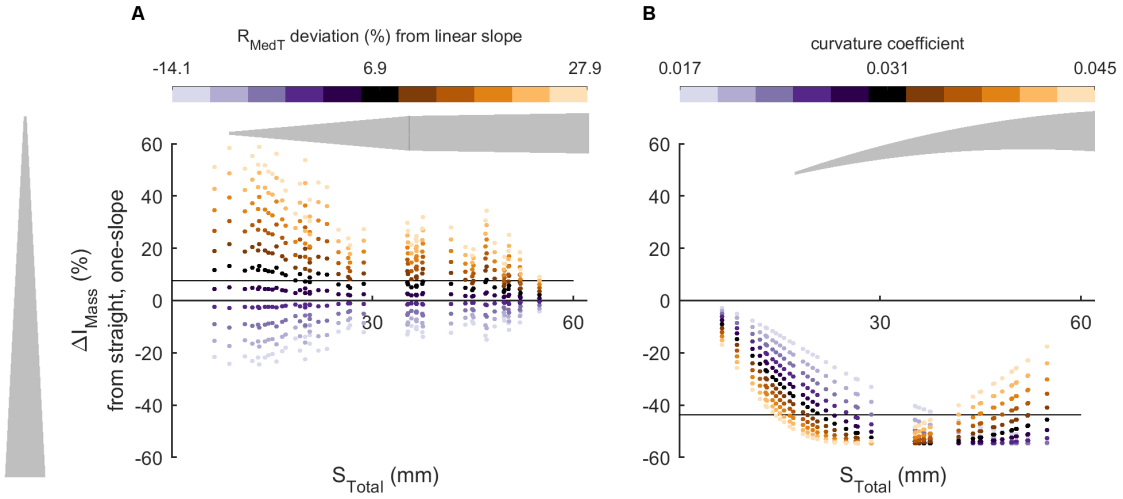

Figure 2.5. Effects of curvature and nonlinear slope on the whiskers mass moment of inertia
This figure compares I_{Mass} calculated under different geometric assumptions. The assumptions are: straight one-slope (baseline), straight two-slopes, and curved one-slope. A "sensitivity analysis" was performed for all 46 whiskers in Table 2.2. Data are colored by the tested slope variation or curvature. The horizontal line shows the mean of all data within each plot. In both subplots, whiskers are arranged by S_{Total} along the x-axis. **(A)** The y-axis shows the change of I_{Mass} from straight one-slope to straight two-slope. The range of R_{MedT} variation is defined based on data in Table 2.2. **(B)** The y-axis shows the change of I_{Mass} from straight one-slope to curved one-slope. The range of curvature variation is defined based on data in Towal et al., 2011.

Comparing the average and standard deviation of the data plotted in black (calculated based on average curvature and slope variation) in each dataset, it is evident that curvature has a much larger effect on I_{Mass} ($-40.77\pm13.19\%$) than two slopes ($8.37\pm16.72\%$), when compared with baseline geometry. The two datasets are significantly different ($p \ll 0.001$, paired two-sample t-test).

2.3.5. Variations in mechanical parameters across the vibrissal array

The overall goal of the present work was to develop mechanical models that could be used to simulate the signals across the entire whisker array during active whisking behavior. We therefore examined each of the mechanical parameters in Table 2.4 (M, I_{Mass}, I_{Area}, and δ) as a function of location within the vibrissal array. To provide intuition for the effect of density variations, we also computed the volume of each whisker, which can be visually compared with the mass.

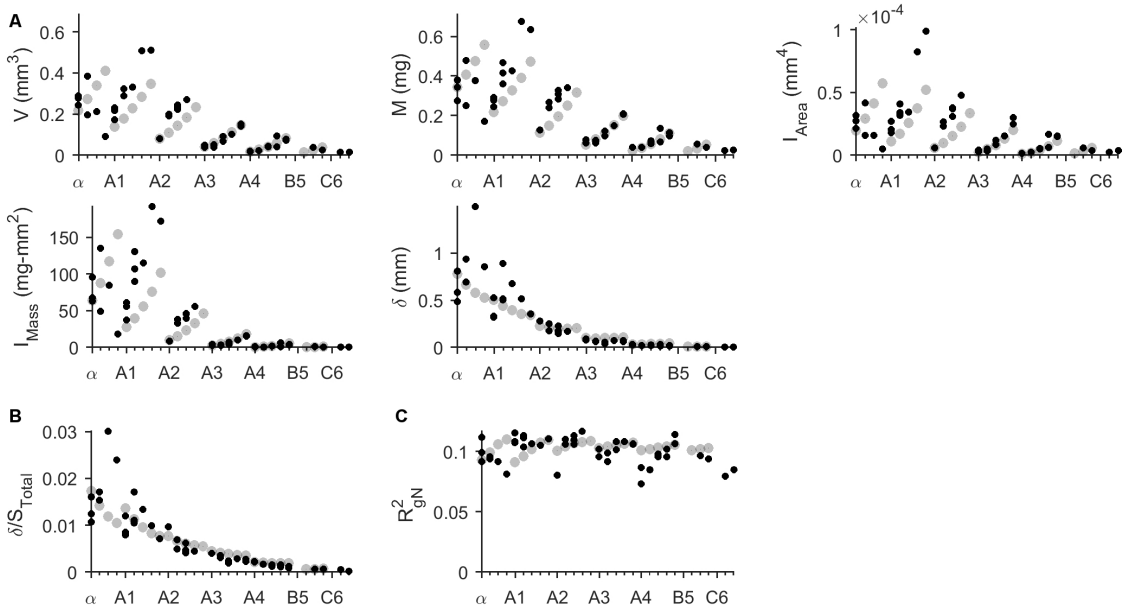

Figure 2.6. Mechanical and material properties as a function of whisker identity

Black circles show experimental data from all 46 whiskers in the dataset. Gray circles are trends computed from equations in Table 2.4, based on a total of 27 whiskers. **(A)** The whiskers volume (V), mass (M), area moment of inertia (I_{Area}), mass moment of inertia (I_{Mass}), and tip defection (δ) all decrease as a function of column position. **(B)** The dimensionless "deflection to length ratio" (δ/S_{Total}) decreases as a function of column position. The more rostral whiskers have the smallest tip deflection for a given whisker length. Longer, more caudal whiskers droop significantly more under their own weight, even when normalized by whisker length. **(C)** The normalized square of the radius of gyration is essentially 0.1 for all whiskers.

Results are shown in Fig. 2.6A, which compares the experimental data with values computed using the equations shown in Table 2.4 assuming a constant cortex density of $1.36 mg/mm^3$. As in the analysis of Table 5, four of the 31 whiskers (B5, C6, D6, and E6) were excluded from the equation-based calculation, so only 27 equation-based data points are shown. The most obvious trend in the figure is that all five variables tend to decrease as a function of column position. This result is expected, because the whiskers tend to become smaller from caudal to rostral (i.e., from column 1 to column 6). A more subtle effect is that within each column, all parameters except for tend to increase slightly from the A row to the E row (ventral to dorsal).

It is also interesting to examine how several dimensionless parameters scale across the array. Two of the four variables listed in Table 2.4– tip deflection (δ) and the mass moment of inertia (I_{Mass})– can

be combined with the total arc length of the whisker and the mass of the whisker to form physically informative dimensionless parameters.

The tip deflection (δ), can be divided by the total arc length (S_{Total}) to form the dimensionless parameter δ/S_{Total}, i.e., the "deflection to length" ratio, as shown in Fig. 2.6B. As its name suggests, this quantity represents how far a whisker of a given length will deflect at its tip under the influence of gravity. This dimensionless parameter reveals that the smallest whiskers have the smallest tip deflection for a given whisker length. The larger, more caudal whiskers are likely to extend the rats sensory volume (Hobbs et al. 2015; Huet and Hartmann 2014) but deflect more under their own weight, even after normalizing for arc lengths.

The second important dimensionless parameter is related to the mass moment of inertia. Dividing I_{Mass} by the whisker mass M yields the square of the radius of gyration ($R_g^2 \equiv \frac{I_{Mass}}{M}$). When normalized by the square of the whisker length, we obtain the normalized square of the radius of gyration ($R_{gN}^2 \equiv \frac{I_{Mass}}{MS_{Total}^2}$), as shown in Fig. 2.6C.

For a solid cone with tip diameter equal to zero, base radius r, and height h, it can be shown that the square of the radius of gyration is $R_g^2 = \frac{1}{20}(2h^2 + 3r^2)$ (equation A.9 in Appendix A), and the normalized square of the radius of gyration can be calculated as the following:

$$R_{gN}^2 = \frac{1}{20}(2 + 3\frac{r^2}{h^2}) \tag{2.19}$$

If $r \ll h$, as is the case for all rodent macro-vibrissae, then R_{gN}^2 is always approximately, though not exactly, 0.1 ($IQR = 0.0155$ for data in black and $IQR = 0.055$ for data in gray in Fig. 2.6). In other words, R_{gN}^2 characterizes how far the whisker shape deviates from a perfect cone.

2.4. discussion

Civil engineers use I-beams, C-beams, and other hollow structured sections to construct bridges and buildings. The design of these structural elements is based on elastic beam bending theory: material is distributed far from the neutral axis, about which the cross-section rotates during bending, to increase resistance to bending without increasing weight (Hibbeler 2014). With its hollow medulla, the rat whisker exhibits similar mechanical advantages. In addition, systematic variations in dimensionless parameters across the array lend support to the idea (Belli et al. 2017) that whiskers in different row and column positions have been precisely tuned to diversify the tactile signals received.

2.4.1. Advantages of the whisker morphology over hypothetical alternatives

Previous studies, which divided the whisker into quartiles, found that the medulla occupied between 50-75% of the whisker length (Adineh et al. 2015; Voges et al. 2012). More recent work (Belli et al. 2017) has quantified medulla length with $\sim 0.1mm$ resolution. Fig. 4A-D of that work demonstrates close linear relationships betweenthe dimensions of the medulla and those of the entire whisker. The fraction of the whiskers volume occupied by the medulla is smaller for shorter whiskers than for longer whiskers, so rostral whiskers will tend to have a more uniform average density than caudal whiskers. These density variations will be important for accurate dynamic simulations, for example, in analyses of non-contact whisking, interactions with textured surfaces, and during collisions (Boubenec et al. 2012; Khatri et al. 2010; Quist et al. 2014).

Consistent with the presence of the medulla, Fig. 2.3A of the present work confirms that the proximal region of the whisker has a lower average density than the more distal region. An important caveat, however, is that the medulla is only one of several factors contributing to the average density variations observed in Fig. 2.3A. A more important factor seems to be that the cuticle occupies an increasing volume fraction of the whisker towards its distal regions (Quist et al. 2011). Given that the cuticle probably has a different density than the cortex (Stanic et al. 2015), these material differences could account for much of the observed density variation.

The presence of the medulla within the whisker offers several key advantages over the two hypothetical geometries shown in Fig, 2.4 and described in Table 2.4. Most obviously, the medulla decreases the total mass of the whisker compared to a solid ("filled") whisker. In addition, the medulla reduces the amount that the whisker deflects under its own weight. Table 2.4 shows that without the presence of the medulla, tip deflection increases by $\sim 1.5\%$ for the filled whisker and by over 11% in the reduced volume case. However, even though the medulla is proportionally larger in caudal whiskers, the deflection to length ratio is not constant across the array. Most caudal whiskers deflect more under their own weight in proportion to their length (Fig. 2.6B). The maximum deflection of any whisker under the influence of gravity is approximately 1 mm.

Finally, as shown in Table 2.4, the medulla serves to increase stiffness at the whisker base (I_{Area}), while minimizing the amount of energy required to whisk at a given rotational velocity (I_{Mass}). If the medulla were filled, whiskers would have slightly greater (by less than 1%) I_{Area} than actual whiskers, but in return they would bear the cost of increases in mass ($\sim 5.7\%$) and mass moment of inertia ($\sim 2.8\%$). If the whisker volume were reduced (the "squashed" whisker), I_{Mass} would decreases slightly (by less than 1%), but the tradeoff would be a large decrease in stiffness at the whisker base (by more than 12%).

Although these changes may seem small, a 3-12% change for all whiskers across the array will have a significant effect, especially given that a rat whisks continuously between 5 and 25 Hz during long durations of active tactile exploration (Berg and Kleinfeld 2003; Welker 1964).

2.4.2. Center of mass and radius of gyration

Assuming a straight whisker, the variability in density along the whiskers length has a small effect on the whiskers center of mass or radius of gyration. About 2.4% difference was observed when the center of mass was computed assuming a constant density for the whisker instead of variable proximal/distal density.

The radius of gyration, R_g, is the point at which all the mass of an object should be placed in order to maintain a rotational inertia equivalent to that of the original object. The radius of gyration can be thought of as the rotational analog to the center of mass. An important difference, however, is that

the center of mass does not depend on the direction in which the object is translated. In contrast, the radius of gyration depends on the axis of rotation. In the present work, R_g was computed about the axis of rotation associated with natural whisking behavior. Note also that the present work computes R_g assuming that the whisker does have intrinsic curvature.

For a solid cone, the square of R_g depends on the sum of the length squared and the radius squared (Eq. 2.19). Because the whisker is so long and thin, the contribution of the radius will be negligible, so Eq. 2.19 simplifies to $R_g^2 = 0.1S^2$. Thus, if the whisker were a perfect solid cone, its radius of gyration would always be at a location 31.6% of the whisker length.

Fig. 2.6C clearly shows that the whiskers deviate at most $\sim$ 10% from perfect cones, shifting the value of $(R_g/S_{Total})^2$ from 0.100 to a maximum of 0.110 and a minimum of 0.091 for equation-based whiskers. Thus, the radius of gyration for a typical whisker will always be found at distances that range from $\sim$ 30.1% to $\sim$ 33.2% of the whisker length. Even if the whisker is damaged, R_g will scale with whisker length and mass so the rat does not have to learn a new dynamic scaling law. This is a result of the high length-to-radius aspect ratio.

From a motor control standpoint, these results imply that the muscle torque required to rotate the whisker at a given angular acceleration will always be proportional to the whiskers mass multiplied by a constant fraction ($\sim$ 0.11) of the square of the whisker length. Under the hypothesis that muscle force depends upon the number of fibers (Oatis 2004), if the number of muscle fibers per motor unit for each whisker scaled with MS_{Total}^2, then the motor system could send the same rate of spikes to each intrinsic muscle and all whiskers would rotate with the same angular acceleration. Alternatively, the number of neurons in the facial motor nucleus activated by a presynaptic neuron (e.g., a neuron in M1) could scale with MS_{Total}^2 to achieve the same effect. Note, however, that this analysis neglects the mass and drag of the follicle itself, as well as the viscoelastic properties of the tissue.

2.4.3. Summary and future work

The present study has quantified several important parameters that are essential for accurate simulations of whisker dynamics. Systematic variations in dimensionless parameters across the array lend support to

the idea (Belli et al. 2017) that whiskers in different row and column positions have been precisely tuned to diversify the tactile signals received. We anticipate that future simulation studies will exploit these results to quantify the mechanosensory signals associated with vibrissotactile exploratory behavior; these signals can then be correlated with neural activity (Bush et al. 2016a).

In addition, increasing evidence points to the idea that different groups of whiskers may be best suited for different functions (Ahl 1986; Brecht et al. 1997; Carvell and Simons 1990; Hobbs et al. 2015; Hobbs et al. 2016; The et al. 2013; Wineski 1983). These groupings may correspond at least in part to muscle groups that activate different regions of whiskers (Haidarliu et al. 2012; Haidarliu et al. 2013; Haidarliu et al. 2011; 2010; Hill et al. 2008; Simony et al. 2010). The varying geometric and motor relationships across the array will diversify the signals acquired during active tactile sensation. An important area of future work will be to examine the effect of geometry on quasi-static bending from external forces and moments (Hires et al. 2013; Huet and Hartmann 2016; Kaneko et al. 1998; Solomon and Hartmann 2008).

On a more speculative note, we observe that– although not quantified in the present work– three locations appear to converge along the length of each whisker: the location where the medulla terminates (Belli et al., 2017); the location of the "change-point" at which the cuticle thickness increases significantly (Quist et al., 2011); and the location at which whiskers tend to curve out of the plane (Knutsen et al. 2008; Towal et al. 2011). It would be interesting if these three locations were in fact the same.

Acknowledgments

We thank Chris S. Bresee for many helpful discussions. This work was supported by National Science Foundation awards CAREER IOS-0846088 and EFRI-0938007, as well as NIH R01-NS093585 to MJZH. HMB was supported in part by Ruth L. Kirschstein National Research Service Award (NRSA) Individual Predoctoral Fellowship NIH F31-NS090872-01A1.

CHAPTER 3

Whisking kinematics enables object localization in head-centered coordinates based on tactile information from a single vibrissa

This chapter has been published as "Yang AET and Hartmann MJZ (2016) Whisking Kinematics Enables Object Localization in Head-Centered Coordinates Based on Tactile Information from a Single Vibrissa. Front. Behav. Neurosci. 10:145. doi: 10.3389/fnbeh.2016.00145".

Abstract

During active tactile exploration with their whiskers (vibrissae), rodents can rapidly orient to an object even though there are very few proprioceptors in the whisker muscles. Thus a long-standing question in the study of the vibrissal system is how the rat can localize an object in head-centered coordinates without muscle-based proprioception. We used a three-dimensional model of whisker bending to simulate whisking motions against a peg to investigate the possibility that the 3D mechanics of contact from a single whisker are sufficient for localization in head-centered coordinates. Results show that, for nearly all whiskers in the array, purely tactile signals at the whisker base– as would be measured by

mechanoreceptors, in whisker-centered coordinates– could be used to determine the location of a vertical peg in head-centered coordinates. Both the "roll" and the "elevation" components of whisking kinematics contribute to the uniqueness and resolution of the localization. These results offer an explanation for a behavioral study showing that rats can more accurately determine the horizontal angle of an object if one column, rather than one row, of whiskers is spared.

3.1. Introduction

Many rodents, including rats, exhibit 5 to 12 Hz "whisking" motions of the large facial vibrissa as they tactually explore the environment. During tactile exploration with whiskers, rats can orient quickly and precisely to an object even though there are very few proprioceptors in the whisker muscles (Ebara et al., 2002; Moore et al., 2015). A large open question, then, is how the rat might localize an object in head-centered coordinates without muscle-based proprioception. Specifically, how does the rat know the angular position of the whisker (and hence the object) at the instant of whisker-object contact? Several possible answers to this question have been proposed by three behavioral studies that have quantified the degree to which rodents can localize an object in the horizontal plane (Knutsen et al., 2006; Mehta et al., 2007; O'Connor et al., 2010).

Mehta et al. (2007) propose that the rat integrates a binary touch signal with kinesthetic information about the angular position of the vibrissa at the time of contact. The authors suggest that the kinesthetic signal could be generated either in the periphery, via "whisking" neurons of the trigeminal ganglion (Zucker and Welker, 1969; Szwed et al., 2003; Szwed et al., 2006; Leiser and Moxon, 2007; Khatri et al., 2009; Wallach et al., 2016) or from a cortical reafferent signal (Mehta et al., 2007; Curtis and Kleinfeld, 2009; Hill et al., 2011; Moore et al., 2015). Similarly, Knutsen et al. (2006), suggest that temporal coding (e.g., the interval elapsed between whisking onset and object contact) could provide information about the angular location of the object in head-centered coordinates (Szwed et al., 2003; Szwed et al., 2006; Knutsen and Ahissar, 2009; Wallach et al., 2016). OConnor et al., (2010) who worked in mice, indicate that differences in the bending of the whisker are observed for different angular locations, but experimental resolution of the study did not permit detailed quantification of these effects.

An intriguing alternative hypothesis was proposed in a fourth study that examined three dimensional (3D) whisking kinematics (Knutsen et al., 2008). In this study, the dorsal-ventral elevation as well as the whiskers roll about its own axis were found to be coupled to the protraction angle. In the discussion, the authors suggest that the roll of the whisker could provide a mechanism for the rat to determine where in the whisking cycle an object has been contacted.

Our laboratory recently developed a 3D quasi-static model of whisker bending that allows us to test this hypothesis in simulation. The model computes all six components of force ($\vec{F}$) and moment ($\vec{M}$) at the vibrissal base as a rat whisks against a peg (Huet et al., 2015; Huet and Hartmann, 2016). We can therefore determine to what extent the information present in these mechanical signals sufficient to yield the location of the object.

In behavioral terms, the present work asks: are the tactile signals obtained by a single whisker and transmitted to the follicle– in *whisker*-centered coordinates– sufficient to uniquely determine the location of an object so that the animal can orient to it in *head*-centered coordinates?

3.2. Materials and Methods

3.2.1. Position and orientation of the head and the pegs surrounding the head

The goal of the present work was to simulate the 3D tactile-mechanical information available to the animal under conditions that resembled as closely as possible those of the relevant behavioral experiments (Knutsen et al., 2006; Mehta et al., 2007; O'Connor et al., 2010). All of these studies either worked in the head-fixed animal or indicate that head motions were very small. Given that the kinematic equations for 3D whisker motion were also obtained from the head-fixed animal (Knutsen et al., 2008), the present work simulates whisking in the head-fixed rat. Therefore, in simulation, an anatomically-accurate model of the rat head and vibrissal array (Towal et al., 2011) was placed with the snout at the origin and with bregma aligned with lambda in the horizontal plane. Vertical pegs (infinitely tall) were placed on a grid in Cartesian coordinates surrounding the head (Fig. 3.1A). Pegs were spaced 1 mm apart. The grid of pegs occupied the complete region of space that could be reached by the whiskers during retraction and protraction. Simulations were run independently for each whisker. All 31 whiskers in the array were simulated. Some whiskers in the E-row had a strong concave-downward orientation, and this orientation was nearly parallel to the peg for some peg locations. In these cases the mechanics were not well defined, and these peg locations were eliminated in post-processing (Figure 4).

Simulations included only those pegs located between 30% and 90% of the whisker arc length in order to avoid extremely large mechanical signals near the base and immediate slip-off from the peg near the tip of the whisker.

3.2.2. Simulating whisking kinematics

Simulations employed the standard variables illustrated in Fig.1B, where θ represents the horizontal (protraction) angle of the whisker, ϕ is the elevation angle, and ζ is the roll of the whisker about its own axis, as defined by the whiskers intrinsic curvature (Knutsen et al., 2008; Towal et al., 2011).

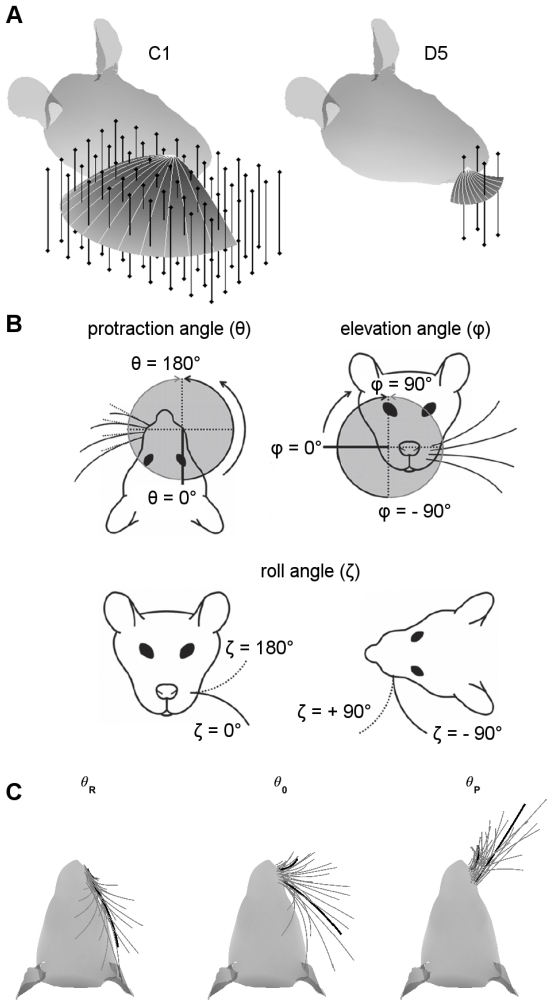

Figure 3.1. Coordinate systems, variables, and parameters used in the simulations

(A) Examples of peg locations relative to the head. The two figurines illustrate the 3D protraction of the C1 and D5 whiskers. The head is oriented so that bregma is aligned with lambda in the horizontal plane. Protraction of the whisker is shown as a curved surface, with shading proportional to the z-coordinate (height). Solid light gray lines within the surface show the whisker shape in 10° increments during the protraction. Vertical bars represent pegs evenly distributed on an x-y grid. Pegs are illustrated at reduced resolution as 4-mm apart in both x- and y- directions for visual clarity, but all simulation results were obtained with 1-mm spacing. **(B)** Angle definitions. The angle θ is the protraction angle, ϕ is the elevation angle, and ζ is the roll of the vibrissa about its own axis. Figure adapted from (Hobbs et al., 2016a). **(C)** Range of whisking. To ensure coverage of the full whisking range, all simulations started with the whisker retracted to be tangent to the rats face in the top-down view. Each whisker was then protracted by 120° or until the tip of the whisker crossed the rostrocaudal midline. The C1 and D5 vibrissae are drawn as thick black lines for visual reference.

As in several previous studies (Huet and Hartmann, 2014; Hobbs et al., 2015; Hobbs et al., 2016b; Hobbs et al., 2016a; Huet and Hartmann, 2016), the horizontal resting angle (θ_0) and the resting orientation of each whisker about its own axis (ζ_0) were obtained from Towal et al. (2011). The elevation resting angles (ϕ_0) were obtained from Knutsen et al. (2008). Note that we obtained θ_0 and ζ_0 from Towal et al. 2011 because these angles are not provided in Knutsen et al. 2008, but ϕ_0 was obtained from Knutsen et al. 2008 because the parametrization in Towal et al. 2011 yields unrealistically low values of ϕ_0 for the A-row whiskers (Huet and Hartmann, 2014).

All simulations were initially run using equations for whisking kinematics obtained from awake behaving animals by Knutsen et al. (2008). These equations were obtained in a coordinate system in which the horizontal plane was defined by the line connecting the nose and the anterior-most corner of the rat eye.

We realized, however, that more accurate results would be obtained if the kinematic equations of Knutsen et al. (2008) were converted to the same coordinate system as the morphological model of the rat, in which the horizontal plane is defined by bilateral alignment of the whisker rows (Towal et al., 2011). We therefore performed this coordinate-system conversion. The original and converted kinematic equations are shown in the top and bottom halves of Table 3.1. All simulations were then completely rerun using the new, converted equations, and results compared with those obtained using the old equations.

The conversion shown in Table 3.1 was achieved in four steps.

First, we found the head pitch offset between the coordinate system of the morphological model and the coordinate system in which the kinematic equations were determined. The pitch difference was found to be a rotation of 13.8° clockwise, tipping the snout down. This pitch difference goes from the coordinate system of the morphological model to the coordinate system of the kinematic equations.

Second, recall that the resting elevation angle ϕ_0 was originally obtained from the coordinate system of the kinematic equations. We therefore had to deter‘mine this angle in the coordinate system of the morphological model. To do this, all whiskers were first set to their resting azimuthal angles in the coordinate system of the morphological model (ϕ_0). All whiskers were rotated by the 13.8° pitch offset to be in the same coordinate system as the kinematic equations and then set to their elevation angle ϕ_0.

Table 3.1. Equations used to simulate whisking kinematics.

Kinematic equations in the coordinate system of Knutsen et al. 2008			
Row	Protraction	Elevation	Roll
A	$d\theta = 0.02/dt$	$\phi = (56 \pm 5.3) + 0.12d\theta$	ζ=$\zeta_0(0.76 \pm 0.08) * d\theta$
B	$d\theta = 0.02/dt$	$\phi = (25 \pm 9.4) + 0.30d\theta$	ζ=$\zeta_0(0.25 \pm 0.18) * d\theta$
C	$d\theta = 0.02/dt$	$\phi = (-4.2 \pm 6.3) + 0.30d\theta$	ζ=$\zeta_0 + (0.22 \pm 0.22) * d\theta$
D	$d\theta = 0.02/dt$	$\phi = (-27.2 \pm 7.7) + 0.14d\theta$	ζ=$\zeta_0 + (0.42 \pm 0.11) * d\theta$
E	$d\theta = 0.02/dt$	$\phi = (-44 \pm 7.6) + 0.02d\theta$	$\zeta = \zeta_0 + (0.73 \pm 0.14) * d\theta$
Kinematic equations after converting to the coordinate system of Towal et al., 2011			
Row	Protraction	Elevation	Roll
A	$d\theta = 0.02/dt$	$\phi = (53.3 \pm 4.25) + (0.398 \pm 0.005)d\theta$	$\zeta = \zeta_0(0.900 \pm 0.026)d\theta$
B	$d\theta = 0.02/dt$	$\phi = (22.1 \pm 4.69) + (0.591 \pm 0.008)d\theta$	$\zeta = \zeta_0(0.284 \pm 0.005)d\theta$
C	$d\theta = 0.02/dt$	$\phi = (-6.59 \pm 5.30) + (0.578 \pm 0.000)d\theta$	$\zeta = \zeta_0 + (0.243 \pm 0.000)d\theta$
D	$d\theta = 0.02/dt$	$\phi = (-30.2 \pm 5.21) + (0.393 \pm 0.001)d\theta$	$\zeta = \zeta_0 + (0.449 \pm 0.001)d\theta$
E	$d\theta = 0.02/dt$	$\phi = (-46.6 \pm 4.64) + (0.217 \pm 0.000)d\theta$	$\zeta = \zeta_0 + (0.744 \pm 0.001)d\theta$

Whisker angles ϕ and ζ are functions of the protraction angle θ and the row identity of the whisker. *(Top half)* Numerical constants in these equations were obtained from the experimental study of Knutsen et al. (2008). The incremental displacement $d\theta$ is measured relative to the resting angle $theta_0$, which was obtained from Towal et al., 2011. The resting angle ζ_0 is unique for each vibrissa and was obtained from Towal et al (2011). Plus-minus values in equations for ϕ and ζ are error bounds from Knutsen et al. (2008). *(Bottom half)* The equations in the top half of the table were converted to the coordinate system of the morphological model. Details of the conversion are described in Methods.

At this point all whiskers now had their correct resting angles θ_0 and ϕ_0 in the coordinate system for the kinematic equations. Finally, all whiskers were rotated by the negative of the pitch offset, back into the coordinate system of the morphological model.

Third, we determined the slopes for $\Delta\phi/\Delta\theta$ and $\Delta\zeta/\Delta\theta$ from Table 3.1 and Figure 2 in Knutsen et al., 2008. These slopes are in the coordinate system of the kinematic equations. Following a procedure similar to that of step 2, these slopes were converted to the coordinate system of the morphological model.

Fourth, we converted the desired range of protraction angles $\Delta\theta$ from morphological into kinematic coordinates. We used the slope relationships $\Delta\phi/\Delta\theta$ and $\Delta\zeta/\Delta\theta$ to obtain the full kinematic equations, and then converted the full kinematic equations back into morphological coordinates.

Notably, Table 3.1 shows that within the coordinate system of Knutsen et al. (2008), the resting elevation angle ϕ_0 is constant within each row. In contrast, after conversion to the coordinate system of the morphological model, each whisker has a unique resting elevation angle phi_0. In other words, we

must assign a specific value of ϕ_0 for each individual whisker. The average and standard deviation of these values are provided for each row of whiskers in the bottom half of Table 3.1.

Table 3.1 also shows that after coordinate conversion the equations that define the slope of ϕ with respect to θ ($\Delta\phi/\Delta\theta$) and the slope of ζ with respect to θ ($\Delta\zeta/\Delta\theta$) varied for each whisker independently. However, the slopes were found to be similar enough across all whiskers within a row that a single average value was used on a per-row basis.

Comparing results between stimulations that used the original kinematic equations with those that used the coordinate-transformed kinematic equations significant shifts at the level of individual whiskers. However, the coordinate transformation did not generally change the trends across the array (e.g., Figures 4, 5 and 7) or significantly affect uniqueness of the mappings (Table 3.2). Thus the results described in the present study are robust to fairly large changes in the kinematic equations for whisker motion. Similar robustness was observed in a simulation study that included a sensitivity analysis of variations in the geometry of whisker-object contact (Hobbs et al., 2016a).

3.2.3. Choice of protraction amplitude

We were careful to ensure that each whisker was simulated to protract through a large range of whisking angles (Figure 1C). A simulation began with all whiskers retracted until they were tangent to the surface of the rats head (left subplot). Each whisker was then simulated to protract through its resting angle (middle subplot) until one of two terminating criteria was met (right subplot): either it reached a total protraction amplitude of 120°, or the tip of the whisker backtracked along the rostro-caudal direction. For most whiskers, this range exceeded the protraction amplitudes observed in many experimental studies (Carvell and Simons, 1990; Gao et al., 2001; Gao et al., 2003; Towal and Hartmann, 2006; Hill et al., 2008; Towal and Hartmann, 2008; Grant et al., 2009; Grant et al., 2012; Hobbs et al., 2016b). These extreme choices for protraction amplitude ensured that our uniqueness and resolution measurements (Sections 3.3.3 and 3.3.4) covered all regions of the whisking space.

The simulation was run in two stages, with coarse and fine spatial resolution. In the first stage the approximate location of the peg was determined by simulating the protraction over the full range

of whisker protraction in increments of 2°. This first stage narrowed the range of possible peg-whisker contact location to an annular sector with an opening angle of 2° and two radii that differed by 2% of the whisker length. The second stage then started from the angle found in stage one, and protracted the whisker forward with a 0.02° step size for up to 100 steps or until the distance between the peg and the nearest point on the whisker stopped decreasing. The whisker was considered to have contacted the peg at the protraction angle when the peg-to-whisker distance was minimal.

To simulate whisker deflection, each whisker was protracted 5° past the angle at which it would have made contact with the peg, had the peg been present. The undeflected 3D shape of the whisker as well as the 3D position of the peg were the two inputs to the quasi-static numerical model described in section 3.2.5. All mechanical signals analyzed in Results were determined at the end of the 5° protraction.

A value of 5° was chosen for two reasons. First, when we examined the three studies describing the behavioral experiments (Knutsen et al., 2006; Mehta et al., 2007; O'Connor et al., 2010), our best understanding was that the rodents deflected their whiskers against the peg by only a few°. Other studies that have explicitly monitored contact durations or angles during object exploration have found similar evidence for light touch (Deutsch et al., 2012; Hobbs et al., 2015), and light touch is also observed during detection and orienting behaviors (Grant et al., 2009; Mitchinson et al., 2011). Second, the whisker tends to slip off the peg if it protracts too far (Williams and Kramer, 2010; Hires et al., 2013).

3.2.4. Coordinate systems: whisker-centered vs. head centered coordinates

To understand the nature of vibrissal-based object localization requires making a clear distinction between the two coordinate systems illustrated in Fig. 3.2: head-centered coordinates and whisker-centered coordinates.

Orienting behavior is expressed by motion of the rats entire head. In head-centered coordinates the location of an object is most easily expressed using the snout as the origin. The rat must be able to orient its snout towards an object regardless of which whisker(s) made contact with the object. However, each whisker in the array has a unique arc length and a unique intrinsic curvature. Each whisker has a different basepoint on the rats cheek, and each whisker emerges from the cheek with a different set of

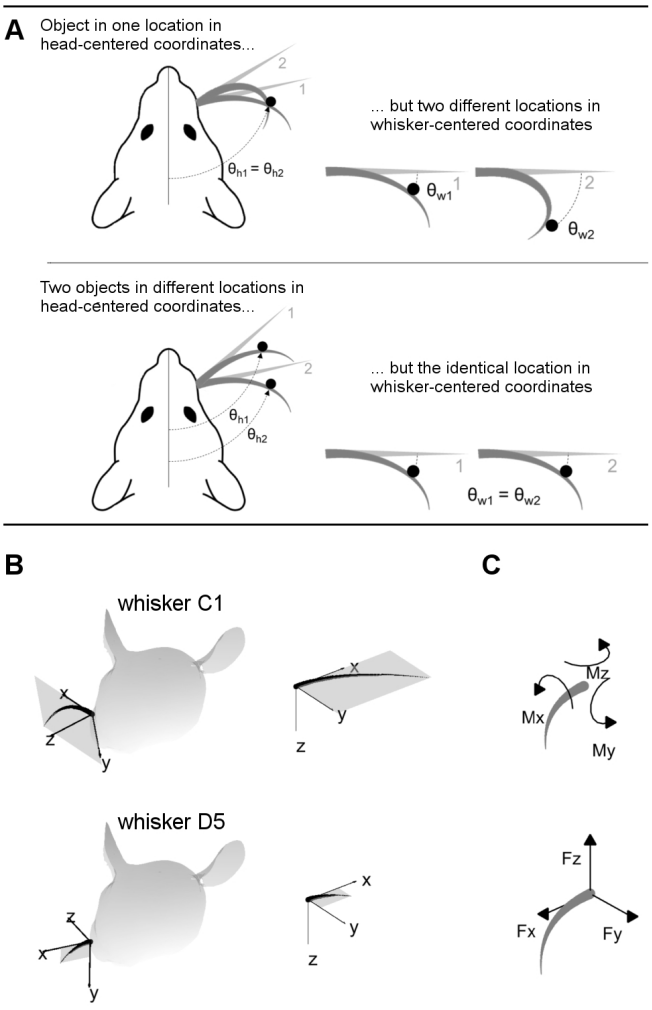

Figure 3.2. 2D intuition for head-centered and whisker-centered coordinate systems.
(A) The origin for head centered coordinates is typically taken to be the tip of the snout, with the y-axis pointing along the midline. In contrast, the origin for whisker centered coordinates is at the whisker base, and the x- and y- axes are determined by the plane in which the whisker lies. The differences between these two coordinate systems are exemplified in two extreme cases, as labeled. Although the rat orients to objects in head centered coordinates, the only tactile information available is most naturally represented in whisker-centered coordinates. (B) 3D intuition for head-centered and whisker-centered coordinate systems. In all panels gray trapezoids indicate the plane of the whisker. *(Left panels)* Whiskers C1 and D5 are illustrated in their resting positions on the rats face Whisker-centered coordinates are indicated. *(Right panels)* Whiskers C1 and D5, still in their whisker-centered coordinate systems, are rotated to the same 3D angle to facilitate visual comparison. (C) Mechanical signals at the whisker base. When a whisker is deflected by an external point load it generates three forces and three moments at the whisker base.

angles when at biomechanical rest. Each whisker is rotated by a different intrinsic ("sling") muscle which wraps around the follicle at its base.

The important consequence of this geometry, as illustrated in two dimensions in Fig. 3.2A, is that the tactile (mechanical) signals that enter the follicle due to contact with an object are obtained in whisker-centered coordinates, which rotate with each whisker (Hartmann, 2015; Huet et al., 2015; Huet and Hartmann, 2016). Tactile information depends only on the difference between the shape of the whisker before and after deformation. The position of the whisker before deformation is not directly encoded in the transmitted signals, and there are few if any proprioceptors in the whisker muscles to tell the rat where the whisker is in head centered coordinates (Moore et al., 2015). Fig. 3.2B provides intuition for the 3D transformations between whisker-centered and head centered reference frames. In this figure whiskers C1 and D5 are shown in their resting positions on the rats face, in the context of their two unique, whisker-centered coordinate systems. The orientation of the C1 whisker is primarily concave down, so the x-y axes form nearly a vertical plane and the z-axis points mostly forwards. The orientation of the D5 whisker is primarily concave forward, so the plane formed by the x-y axes is more horizontal (tilted out of the page in Fig 2B) and the z-axis points forward and a bit up. Although the coordinate systems for the C1 and D5 whiskers may initially appear very different in the context of the rats head, it is clear from the right panels of Fig. 3.2B that they are identical whisker-centered coordinate systems.

The specific question addressed by the present work is: are the tactile signals obtained by any single whisker and transmitted to the follicle in *whisker*-centered coordinates sufficient to uniquely determine the 2D location of an object in *head*-centered coordinates?

3.2.5. Computing mechanical signals as the whisker protracts against a peg

The present work uses a quasi-static model for whisker bending that permits us to simulate 3D mechanics and the whiskers slip along a peg (Huet et al., 2015; Huet and Hartmann, 2016).

Details of the model have been described in these earlier studies, but briefly, each whisker is simulated as a 100-link Euler-Bernoulli beam connected by linear and torsional springs. Whiskers were simulated to have a Youngs modulus of 3 GPa (Quist et al., 2011). Whisker arc lengths (S) were determined

based on their (row, column) position within the array (Towal et al., 2011). Base diameters (D_{base}) were calculated based on the linear relationship $D_{base} = 0.07113 + (0.00208)S$, where S and D_{base} are expressed in millimeters (Belli et al., 2016). Whisker tips are often damaged, so tip diameter can vary considerably. Tip diameter was therefore assigned a constant value of 4.1 μm, calculated as the average across 52 whiskers (Belli et al., 2016).

The inputs to the model are the 3D location of the peg, and the 3D intrinsic position and shape of the undeflected whisker, protracted 5° past the angle at which it would have made contact with the peg. The outputs of the model are the deflected whisker shape and the resultant mechanical signals at the whisker base. The mechanical signals can be written in terms of six components illustrated in Fig. 3.2C: three components of force (F_X, F_Y, and F_Z) and three components of moment (M_X, M_Y, and M_Z).

The physical meaning of each component is as follows: F_X is the axial force, which acts along the direction of whisker shaft, pushing or pulling the whisker directly into or out of the follicle. F_Y and F_Z are the transverse forces, which act along the y- and z- axes in whisker-centered coordinates, respectively. F_Y increases or decreases the curvature of whisker depending on its sign, while F_Z bends the whisker in and out of the plane of its intrinsic curvature. The torsional moment, M_X, twists the whisker about its own shaft. The bending moments M_Y and M_Z are correlated, respectively, with F_Z and F_Y by the radial distance of contact point from the base of whisker.

We reiterate that the present work assumes that rodents receive mechanical signals from individual whiskers without knowledge of the angles of the whisker in head-centered coordinates.

3.2.6. The average minimum distance as metric to quantify the resolution of the mappings

Some analyses (Figures 5, 6, and 7) required a metric to quantify the resolution of the mapping between mechanical signals at the whisker base and the (x, y) location of the peg. The idea here is that a given combination of mechanical signals should map to a single (x, y) location of a peg in head-centered coordinates. Furthermore, the (x, y) location of the peg predicted by those mechanical signals should be far away from the (x, y) locations of any other peg.

We therefore defined the "average minimum distance" as follows: First, because the variables M_B and M_D have different dimensions and different orders of magnitudes (10^{-6} and 100), they were normalized between 0 and 1. Then, for each data point (MB_n,MD_n) we calculated the distance D_{nm} from every other (MB_m,MD_m) point in the dataset: $D_{nm} = \sqrt{(MB_m - MB_n)^2 + (MD_m - MD_n)^2}$. The point ($MB_m$,$MD_m$) with the minimum value of D_{nm} was denoted as $D_{n,min}$ and was selected as the nearest neighbor to (MB_n,MD_n). The same procedure was performed for all N data points in the entire mapping. The sum of all minimum distances $\sum_{n=1}^{N} D_{n,min}$ divided by the total number of data points N was defined as the average minimum distance. Intuitively, this metric provides a measure that answers the question "on average, how close is the nearest (MB, MD) neighbor?"

3.3. Results

3.3.1. Mechanical signals at the whisker base in whisker-centered coordinates vary with the pegs location in head-centered coordinates

All six components of force and moment at the whisker base were found to exhibit systematic variations with the (x,y) location of the peg in head centered coordinates. Examples of these variations are shown in the first two rows of subplots in Fig. 3.3 for whiskers C1 and D5. For each whisker, four of the six mechanical signals vary primarily as a function of the radial distance to the peg. For the C1 whisker these four signals are F_X, M_X, F_Z, and M_Y, while for the D5 whisker the four signals are F_X, M_X, F_Y, and M_Z. However, one of the forces and its corresponding moment have different signs and magnitudes when the whisker presses against posterior compared to anterior pegs. These signals are F_Y and M_Z for C1 and F_Z and M_Y for D5. These signals therefore exhibit significant variation in a posterior/anterior direction.

The near orthogonality of the two types of variations suggests that there may be multiple combinations of mechanical variables that could uniquely represent the two parameters (x, y) that define the location of the peg. Rather than try every possible combination of the raw signals one by one, we turned to neurophysiological results for guidance.

Recordings from primary sensory neurons in the trigeminal ganglion show that responses correlate strongly with both the magnitude (Szwed et al., 2003; Szwed et al., 2006) and direction (Simons, 1978; Gibson and Welker, 1983; Simons, 1985; Lichtenstein et al., 1990; Jones et al., 2004; Lottem and Azouz, 2011; Lottem et al., 2015) of whisker bending. We therefore rewrote the y- and z- components of the bending moments in terms of the magnitude and direction of their vector sum: $M_B = \sqrt{M_Y^2 + M_Z^2}$ and $M_D = \arctan(M_Z/M_Y)$.

As shown in the bottom row of Figure 3, the mappings for M_B and M_D are excellent complements, in that M_B is mostly correlated with radial distance, while M_D is more correlated with the angular location of contact. In the next two sections we therefore ask first, whether these two signals vary systematically

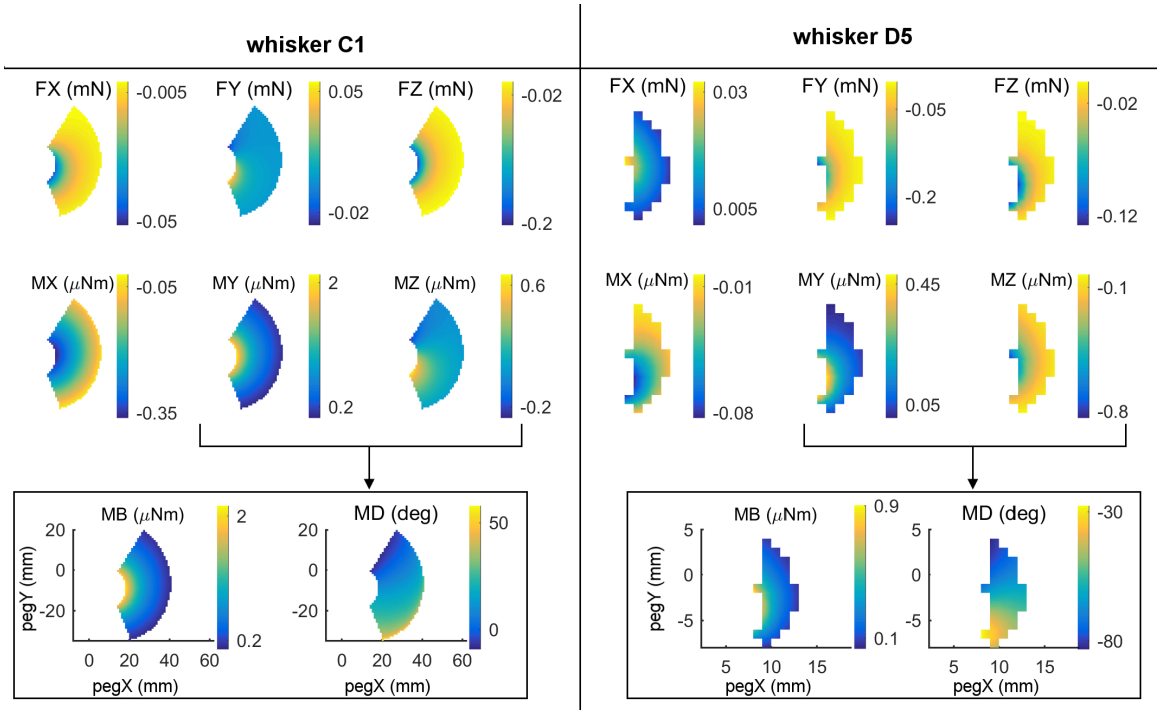

Figure 3.3. Mechanical signals vary with the (x,y) location of contact.
The left and right halves of this figure display results for two different whiskers, C1 and D5. *(Top two rows)* all six components ($F_x, F_y, F_z, M_x, M_y, M_z$) of mechanical signals after the whisker was simulated to deflect 5° against pegs at different (x,y) locations in head-centered coordinates. The location (0,0) represents the rats snout. At any (x,y) location in each subplot, color represents the magnitude of the signal at the whisker base after the 5° deflection against the peg at that (x,y) location. Colors were interpolated between peg locations and the relevant scale for each signal is shown in the colorbars. *(Bottom row)* The signals M_y and M_z can be combined into the magnitude and direction of the bending moment. Notice that for whisker C1, M_B almost entirely follows M_Y because M_Z is so much smaller than M_Y. The same is not true for D5 because it pushes differently against the peg.

with peg location, and second, to what extent these two signals alone can uniquely represent the (x,y) location of the peg.

3.3.2. Bending magnitude and direction vary with peg location for all whiskers

To represent M_B and M_D intuitively within a single plot, vector fields are used to represent these two variables at each peg location for all 31 whiskers of the array. Results are shown in Fig. 3.4. In this figure the subplots are spatially arranged to match the arrangement of the vibrissae on the rats face. Each subplot shows the vector field of bending magnitude and direction for one whisker. The origin of each

vector is placed at the (x, y) location of the peg of contact. The magnitude of the vector represents the magnitude of the bending moment, and the direction of the vector indicates the direction of the bending moment. Because it is difficult to see the direction of some of the shorter vectors, the bending direction is also represented by the color of each vector. We emphasize that although the figure illustrates the direction of bending moment in the (x, y) plane, the direction of bending moment is actually a combination of the two bending moments in the y- and z- directions in whisker-centered coordinates. Both y- and z- axes are perpendicular (transverse) to the whisker shaft.

The first feature evident in Fig. 3.4 is that each whisker reaches very different numbers and very different subsets of pegs. The subplots are on the same scale within each column so the size of the regions reached can be directly compared (from A row to B row, etc.). The scale of the subplots changes between columns, but the shapes of the regions that can be reached can be compared from column to column (e.g., from Column 1, to 2, to 3, etc.). For example, rostral whiskers were able to reach more anterior pegs; there is more variability between rows than between columns; and in general, whiskers in rows B and C reach the most pegs.

The second result revealed by Fig. 3.4 is that both the magnitude and the direction of the bending moment vary systematically for each of the 31 whiskers. As suggested by the plots of Fig. 3.3, the direction of bending varies primarily with the pegs anterior/posterior location, while the magnitude of bending varies more with radial distance. Moreover, there is large degree of variability from whisker to whisker, even for two whiskers close together, for example β and γ. The question remains, however, to what extent the vector plots shown in Fig. 3.4 represent unique mappings to the (x, y) locations of the pegs.

3.3.3. Most whiskers show unique mappings

If a mapping between M_B and M_D and (x,y) is unique, then each pair (M_B, M_D) should point to only one x value and only one y value. These mappings can be visualized using the conventions shown in Fig. 3.5, which shows results for the Column 2 whiskers. In each of the subplots M_B is represented on the x-axis and M_D is represented on the y-axis. Each point on the plot is assigned a color corresponding to

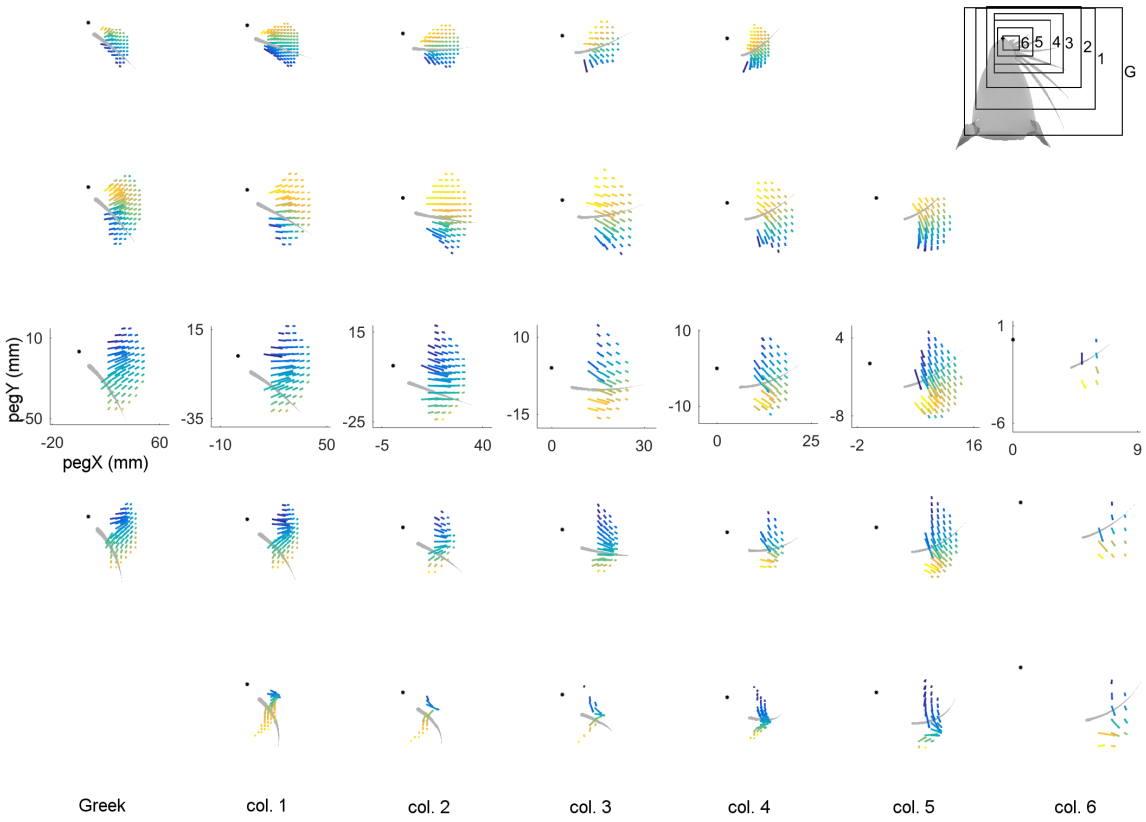

Figure 3.4. Magnitude and direction of bending moment at the whisker base after a 5° rotation against pegs placed at different (x, y) locations relative to the rats head.

The subplots in this figure are positioned in the same pattern as the whiskers on the mystacial pad of the rat, from rows A through E (top-down) and columns Greek through 6 (left-right). Each subplot shows the resting position and orientation of that whisker as a gray, tapered curve. The axes represent the (x, y) locations of the pegs, with the origin at the rats snout. Colored vectors represent the magnitude and direction of the bending moment for that whisker. The color of the vector also represents bending direction because it is difficult to see the direction of some of the very short vectors. Each vector has its origin at the peg location. All subplots within a single column are on the same scale. The subplots in different columns are on different scales because the whiskers differ greatly in length between columns. Axes are shown only within the C-row to indicate that the identical scales apply within each column. The upper-right subplot is a reference for the scales of the plots in each column. Both M_B and M_D are scaled identically within each column, but are scaled differently between columns. All simulations were run with 1 mm resolution in both x- and y-, but the number of pegs in each subplot has been reduced for visual clarity.

the associated x- or y-location of the peg. Points are interpolated between locations and the plot is made transparent so that uniqueness can be directly visualized. Non-unique locations in the map show sharp

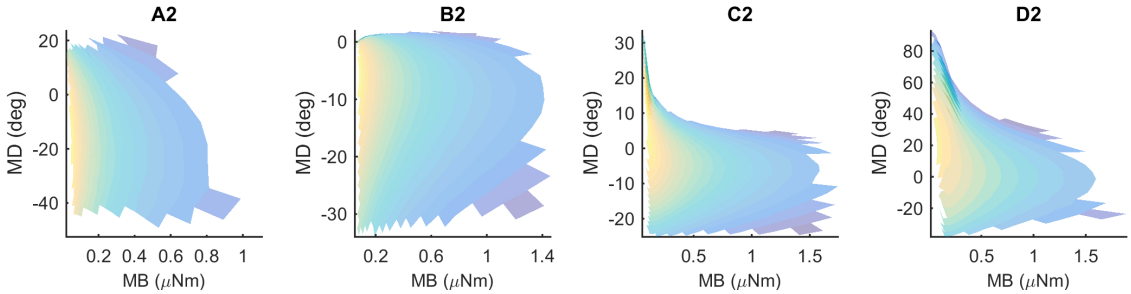

Figure 3.5. Mappings for the Column-2 whiskers are generally unique, typical of all whiskers of the array.

The x- and y- axes represent the magnitude and direction of bending moment, respectively. All data points are interpolated to form a surface colored by the x-locations of the pegs. The surface has been rendered to be partially transparent, so that non-unique (overlapping) regions of the mappings are revealed. Overlaps, if present, are visible as regions of high color intensity. In this example of the column 2 whiskers, whisker B2 is non-unique in the extremely narrow dark blue strip near $M_D = 0$. Whisker D2 has tiny non-unique patches with steep negative slopes near $M_B = 0.30$ and $M_D = 60$. Overlaps would remain the same for all whiskers if they were colored by the y-location of the pegs instead of the x-location.

edges of brightened color where the surface "folds over" on itself. The "percent uniqueness" (Table 3.2 and Fig. 3.5) was quantified as the percent of surface plot area that did not contain overlap.

The results in Fig. 3.5 indicate that the mappings are nearly completely analytically unique for all whiskers of column 2. There is an extremely narrow band of overlap for the B2 whisker where M_D is close to zero, and for patches of overlap of the D2 whisker in the top left corner, where M_D is large and M_B is small. These results were typical for all columns of whiskers, as summarized in Table 3.2. Of the 31 whiskers tested in the array, 30 reached sufficient number of pegs to generate surface plots that could be analyzed for uniqueness (the exception was whisker C6, which reached very few pegs). Of the 30 surface plots, 11 gave completely (100%) unique results, ten were more than 98% unique, six were more than 95% unique, and the remaining three were more than 92% unique. It is worth noting that all three whiskers with less than 95% uniqueness belonged to row E: whiskers in this row reach far fewer pegs than the other rows (c.f., Fig. 3.4), and the orientation of whiskers more concave-downward.

Table 3.2. Number of pegs reached and the percent of mapping that is unique

Whisker	N pegs	% unique
α	535	100.00
A1	446	100.00
A2	305	99.99
A3	166	100.00
A4	66	100.00
β	1390	97.42
B1	1023	98.88
B2	668	99.93
B3	397	100.00
B4	194	100.00
B5	55	100.00
γ	1656	99.53
C1	1048	98.79
C2	616	98.71
C3	344	99.20
C4	179	97.66
C5	69	95.94
C6	6	N/A
δ	1090	98.49
D1	579	98.53
D2	307	97.72
D3	173	98.94
D4	98	100.00
D5	55	100.00
D6	12	100.00
E1	147	97.44
E2	46	96.00
E3	44	93.63
E4	33	92.94
E5	28	93.75
E6	12	100.00

Abbreviations: N pegs: number of pegs; % unique: Percent of the (M_B, M_D) space that uniquely maps to an (x,y) peg location. Whisker C6 was simulated but is labeled N/A because it reached too few pegs to form a surface for this analysis.

3.3.4. Both elevation and roll contribute to the uniqueness and the resolution of the mappings

An intrinsic limitation of the type of simulation results shown in Fig. 3.5 is that a solution could be declared unique even if two mappings differed by only floating point error. Uniqueness does not have much practical utility unless a measure of resolution is added. Therefore, the average minimum distance

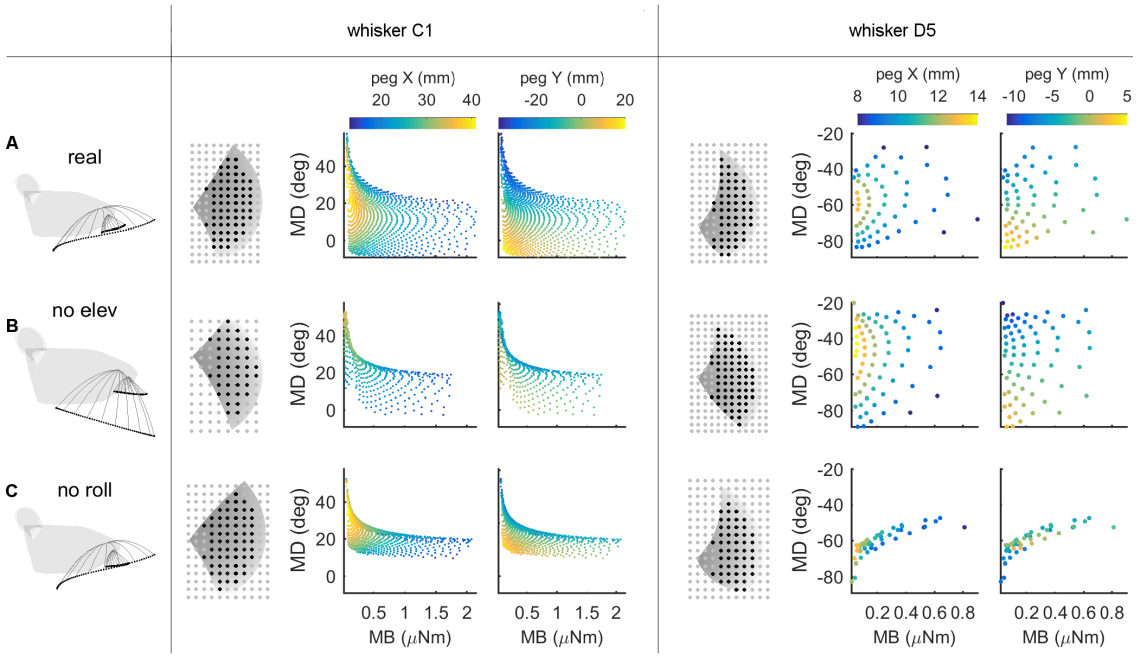

Figure 3.6. Mappings between bending magnitude and direction (M_B, M_D) and peg location (x,y) as whisking kinematics are altered.

Each row of the figure shows data from the corresponding row of Table 3.3. The first figurine in each row shows a side view of the kinematic profile of the C1 and D5 whiskers. Solid gray lines are representative whisker shapes in 10° increments, and black dots are the whisker tip positions. The grayscale plots in each row show the pegs that can be reached by the whisker (black dots). The grayscale shading indicates the z-coordinate (height) of the whiskers trajectory, and the pegs for the C1 whisker are four times denser than shown in the plot. The colored subplots in each row show the mappings between bending magnitude and direction (M_B, M_D) and the (x,y) location of the peg. Colormaps are the same for all subplots within each column, as indicated in the colorbars at the top of each column. All colored plots for each whisker have the same axis limits (A) Normal whisking kinematics. (B) No elevation. (C). No roll.

(AMD, see Methods) was used to evaluate the resolution of each of the mappings. The C1 and D5 whiskers are used as typical, illustrative examples in Fig. 3.6, but analysis was run on all whiskers in the array.

The colored subplots in Fig. 3.6 are similar to those in Fig. 3.5, except that the data points have not been interpolated to form a surface. The color of each data point corresponds to the pegs x- or y-location, and differentiation between peg locations is associated with larger distances between data points. It is clear that for whisker C1 in Figure 6A, the data points are spread out and that peg locations

vary continuously. Whisker D5 shows a similar trend but reaches fewer pegs (it is a shorter whisker), so the data points are further apart from each other.

We next examined the effect of features of whisking kinematics on the mappings. As described in Methods, when the vibrissal array protracts, each whisker exhibits a small amount of dorsoventral elevation (Bermejo et al., 2002; Knutsen et al., 2008; Knutsen, 2015) as well as roll about its own axis (Knutsen et al., 2008; Knutsen, 2015). We performed simulations with elevation and roll removed, as illustrated in Fig. 3.6B, C. Qualitatively, these figures demonstrate that when either roll or elevation is removed, the data points distribute across a smaller region of the (M_B, M_D) space, meaning that the mapping resolution deteriorates. In addition, for both whiskers C1 and D5, removal of either roll or elevation altered the total number of pegs reached.

The effects of removing elevation are shown in Fig. 3.6B and in Table 3.3. For long, caudal whiskers such as C1, removing elevation decreases the range of bending magnitude (M_B) by approximately 20%, and the range of bending direction (M_D) decreases even more. These effects are quantified in the middle row of Table 3.3, which indicates that resolution (as measured by AMD) decreases to 69% of its value measured during normal kinematics. For short, rostral whiskers such as D5, the effect of removing elevation is more difficult to observe. Only small differences are visible in Fig. 3.6B. Table 3.3 shows that quantitatively, the AMD decreased by 6%, but uniqueness was unaffected and the number of pegs reached actually increased. Thus, by comparing effects between whiskers C1 and D5, we see that the effect of elevation is strongly influenced by the particular whiskers angle of emergence and the orientation of the whiskers trajectory with respect to the peg.

Removing roll has a more consistent effect across whiskers, as shown in Fig. 3.6C and the bottom row of Table 3.3. The range of bending direction (M_D) is dramatically reduced for both whiskers C1 and D5. Uniqueness also drops significantly for both whiskers (to 82% for C1, and to 52% for D5) and mapping resolution is reduced to AMD = 0.52 and AMD = 0.34 for the two whiskers.

It is interesting to note that the removal of either elevation or roll has a much larger effect on bending direction than on bending magnitude. The change in bending magnitude is dominated by the radial distance from the contact point to the whisker base for a fixed pushing angle (in this case, 5 °).

Table 3.3. The effect of elevation and roll on the number of pegs reached and the mapping resolution.

	Whisker C1			Whisker D5		
	N pegs	% unique	A.M.D	N pegs	% unique	A.M.D
Normal kinematics	1048	98.79%	1	55	100.00%	1
No elevation	633	96.28%	0.691	67	100.00%	0.940
No roll	976	82.21%	0.522	50	51.75%	0.339

Abbreviations: N pegs: number of pegs; % unique: Percent of the (M_B, M_D) space that uniquely maps to an (x,y) peg location; A.M.D.: Average minimum distance computed over the entire mapping. The A.M.D. has been normalized to equal exactly 1 for normal whisking kinematics so that the effects of altered kinematics can be quantified.

Summarizing, both roll and elevation contribute in important ways to the quality of mappings, but in different respects. Roll consistently increases both mapping resolution and uniqueness by a significant amount. Elevation contributes to resolution and may or may not to uniqueness, depending on whisker identity.

3.3.5. Localization of a peg using a row vs. a column of whiskers

We can now use the mappings found in sections 3.3.2 – 3.3.4 to suggest explanations for some results of the behavioral studies (Knutsen et al., 2006; Mehta et al., 2007; O'Connor et al., 2010). In all three experiments rodents were required to indicate the horizontal (anterior/posterior) location of a vertical peg. All three studies found that animals could perform the task if whiskers were trimmed such that only one row of whiskers remained (the C row), or even if only one whisker remained (typically C1 or C2), albeit at a reduced performance level.

A particularly intriguing result of one of the studies (Knutsen et al., 2006) was that rats obtained the highest localization acuity ($< 1.5mm$) if they were initially trained on the task with all whiskers intact, and then trimmed to leave only one column (instead of a row) of whiskers.

To explain this result, we hypothesized that, for pegs placed in different anterior/posterior locations, the mappings between (M_B, M_D) and the (r, θ) positions of the pegs in head centered coordinates should be more different for a column of whiskers than for a row of whiskers.

We tested this hypothesis by simulating deflections of the C-row and column-2 whiskers against a set of 26 pegs, as shown in Figs. 7A, B. These are the same whiskers used in the behavioral experiment of Knutsen et al., 2006. The pegs were placed at radial distances either 8 or 12 mm from the average location of the whisker basepoints. The pegs were distributed from -60 ° to 60 ° in 10-degree increments, yielding 13 pegs at each of the two radial distances. Results, shown in Figs. 7C, D, lend support to our hypothesis.

For both proximal and distal radial distances (Figs. 7C, D), the curves for bending magnitude (MB) are similar across all whiskers in the C-row: M_B monotonically decreases from C1 to C4. The M_B curves are also quite similar across the column-2 whiskers: M_B increases from A2 to C2, and then tends to decrease for whisker D2. The curves for bending direction (M_D) are also similar across all whiskers in the C-row: M_D decreases from C1 to C4.

The curves for M_D across the column-2 whiskers, however, exhibit very different slopes depending on the posterior/anterior location of the peg. The A2 whisker will be oriented slightly concave-forward when it makes contact with a peg at a posterior location. Contact with the peg will therefore tend to push the A2 whisker to become straight, resulting in a negative M_D (dark purple curve in the bottom right subplot in Fig. 3.7C). In contrast, the D2 whisker will be oriented slightly concave-backwards when it makes contact with a peg at a posterior location. Contact with the peg will tend to push the D2 whisker to curve more, resulting in a positive M_D (light green curve in the bottom right subplot in Fig. 3.7C).

Conversely, when the whiskers hit a peg at a more anterior location, the A2 whisker has rolled to become oriented slightly concave backwards, while the D2 whisker has rolled to become oriented more concave backward, thus the trends are opposite.

Summarizing, pegs at different angular locations can be more easily distinguished from each other on the basis of differences in bending direction within a column, rather than within a row.

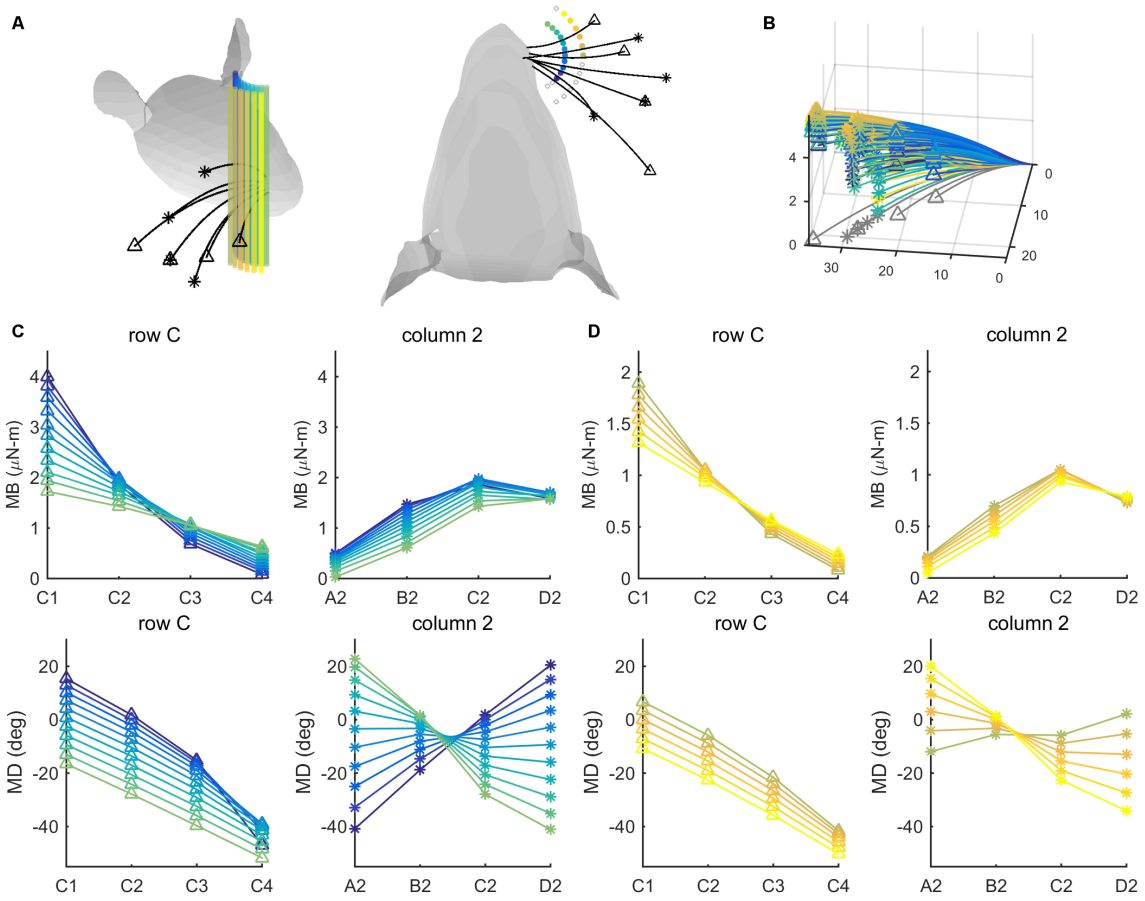

Figure 3.7. Mechanical signals within rows and columns of whiskers.

(A) 26 pegs (colored cylinders) are placed at radial distances r = 8 and r =12 mm from the average location of the whisker base points. The pegs are spread from -60° to 60° in 10° degree increments in head-centered coordinates. Four whiskers of the C row (C1-C4, tips marked with triangles) and four whiskers of column 2 (A2-D2, tips marked with asterisks) are simulated to protract 5° against the peg. (B) The same whiskers as in (A) are now shown in whisker-centered coordinates. All undeflected whiskers lie in the x-y plane, and all proximal segments align with the x-axis. Whiskers are shown in gray before deflection and in color after deflection. The colors of the deflected whiskers correspond to the pegs in panel (A). (C) The four subplots show bending magnitude and bending direction for pegs placed at a radial distance r = 8 mm from the average whisker base. Bending magnitudes and bending directions are plotted for the C-row (triangles) and Column-2 (asterisks) whiskers. The color code corresponds to the peg locations shown in panel (A). (D) The same subplots as in (C), but for pegs placed at a radial distance r = 12 mm from the average whisker base. The color code again corresponds to the peg locations shown in panel (A).

3.4. Discussions

How is it possible for a rodent to orient to an object based on tactile information from a single whisker? To date, this has been a challenging question to answer because the 3D tactile signals available to the rat could not be quantified. The present study exploited a 3D model recently developed by our laboratory (Huet et al., 2015; Huet and Hartmann, 2016) to simulate the mechanical signals the rat will obtain as it whisks against a vertical peg. We find that for nearly all whiskers, sufficient information is available in the bending moment signal to localize the peg, provided that the whiskers kinematic trajectory includes both roll and elevation and the rats head exhibits minimal pitch. These constraints are compatible with the conditions observed in three behavioral studies (Knutsen et al., 2006; Mehta et al., 2007; O'Connor et al., 2010).

3.4.1. Cues for orienting to an object

The present work has demonstrated one possible mechanism by which the rat could localize a vertical peg in head-centered coordinates based entirely on tactile information from a single vibrissa. We do not suggest that the mechanism demonstrated here is the only method by which the rat might determine the pegs location. The nervous system generally exploits all available information to solve perceptual tasks, and multiple redundant cues are likely used.

A complementary possibility is that the rodent could estimate the location of the peg by combining a contact signal with an estimate of the position of the whisker at time of contact. The position signal could be obtained by combining reafferent signals representing the phase of the whisker (Fee et al., 1997; Mehta et al., 2007; Moore et al., 2015; Wallach et al., 2016) with an efference copy of whisking midpoint and amplitude (Curtis and Kleinfeld, 2009; Kleinfeld and Deschnes, 2011). Kinematic (position) control is a viable motor control strategy during non-contact whisking because the whiskers have such low mass; upon contact it seems likely that the rat will shift to a force control strategy (Quist et al., 2014; Hobbs et al., 2016b).

Alternatively, the animal could determine the horizontal angle of a peg by keeping track of the time at which each whisker starts protraction and then integrating whisker velocity with respect to time to

obtain an estimate of the whiskers position at the time of contact (Szwed et al., 2003; Knutsen et al., 2006; Szwed et al., 2006; Knutsen and Ahissar, 2009; Huet et al., 2015). This mechanism would require the rat to keep track of the velocity of each whisker with high precision (Towal and Hartmann, 2006; Towal and Hartmann, 2008; Grant et al., 2009; Hartmann, 2009; Hobbs et al., 2016b).

Peg localization could also be aided by skin stretch, which could serve in a proprioceptive capacity to provide cues about protraction angle. Weak proprioceptive signals from the muscles could also be carried through the mesencephalic nucleus (Mameli et al., 2010; Mameli et al., 2016).

Finally, we note that in order to replicate as faithfully as possible the three previous behavioral experiments, the simulations here used infinitely tall vertical pegs. Therefore the present study does not address the question of how the rat might determine the height of an object. As indicated by several previous articles, the height could be at least partially determined by a labeled line system, that is, determined by the whiskers identity(Knutsen et al., 2008). Alternatively, use of one or more additional mechanical signals (e.g., the axial force) seems likely to resolve this third coordinate (Solomon and Hartmann, 2011; Pammer et al., 2013).

In our view, it would make excellent sense for timing information coupled with velocity integration to provide a coarse estimate of the angular position of the whisker. At each point in time, the position estimate could be updated with information from skin stretch, weak proprioceptive signals, and efference copy. The final cue about the horizontal angle of contact would emerge at the instant of contact, as the whisker deflects against the object in a direction related to the objects angular position. The overall location and shape of an object spanning many whiskers could then be coded by tactile feedback from many whiskers integrated simultaneously.

3.4.2. Potential mechanisms for neural coding

How would mechanical signals transmitted by the whisker be transduced into neural signals while maintaining information about object location? Multiple studies have demonstrated that primary sensory neurons of the trigeminal ganglion are strongly directionally tuned (Simons, 1978; Gibson and Welker, 1983; Simons, 1985; Lichtenstein et al., 1990; Jones et al., 2004; Lottem and Azouz, 2011; Lottem et al.,

2015). This tuning is related, at least in part, to the angular location of mechanoreceptors within the follicle (Ebara et al., 2002; Knutsen et al., 2008; Rutlin et al., 2014; Whiteley et al., 2015).The bending direction (M_D), could therefore be represented by the identity of mechanoreceptors at particular angular locations within the follicle, resulting in a labeled line code (Knutsen et al., 2008) that represents the azimuthal coordinate of object contact.

Trigeminal ganglion neurons are also well known to respond strongly to the magnitude of whisker deflection (Zucker and Welker, 1969; Gibson and Welker, 1983; Szwed et al., 2003; Jones et al., 2004; Szwed et al., 2006). The bending magnitude signal (M_B) is therefore likely to be represented as the number of spikes per unit time as the whisker increasingly deflects against an object, consistent with a role in determining radial distance (Szwed et al., 2003; Szwed et al., 2006).

Importantly, the mechanism for object localization proposed in the current work does not depend on whisking velocity, nor on the velocity of the whisker at time of impact, nor on how rapidly or slowly the whisker deflects against the peg. The peg location can be computed for every combination of M_B and M_D at each point in time. Thus, with the assumption that friction is negligible (see next section), the animal can determine the contact point location regardless of the time-history of the whisker.

In addition, although the present work simulated only protraction against the peg, symmetry arguments suggest that similar results would hold during retraction. The direction of whisker bending (M_D) is determined by its orientation relative to the peg. This orientation depends on the angles through which the whisker rotates during protraction. Although retraction is unlikely to follow the exact inverse trajectory of protraction, it is clear that retraction must ultimately invert all the protraction angles as the whisker returns to its original starting position. Thus the inverted, retraction angles will likely exhibit similar uniqueness characteristics as the forward, protraction angles.

3.4.3. Effects of variable whisking kinematics and friction

In the awake, freely moving animal, whisking kinematics will be more complicated than the 3D trajectories simulated here. In particular, a well-known feature of natural whisking is that the basepoints of

the whiskers translate significantly (Knutsen et al., 2008; O'Connor et al., 2010; Knutsen, 2015). Because equations for translational motions have not yet been established, the present work simulated pure rotation and neglected translation.

This simplification is appropriate for two reasons. First, in our own work on body restrained rats, we found that the purely rotational equations provided by Knutsen et al., 2008 were a remarkably good fit to behavioral data (Huet and Hartmann, 2016). Second, a sensitivity analysis that examined the effect of variations in whisking kinematics on the angle of contact against a surface showed that the effects are systematic across the array (Hobbs et al., 2015; Hobbs et al., 2016a). Thus, if whisking kinematics are altered slightly, the mappings shown in Figs. 3.4, 3.5, and 3.6 will exhibit systematic shifts, but will not become degenerate.

Friction will also play a significant role in determining the direction in which the whiskers are deflected after contact (Solomon and Hartmann, 2008; 2010; Boubenec et al., 2012; Pammer et al., 2013; Huet and Hartmann, 2016). The present simulations assumed frictionless conditions, which in general will ensure the maximum vertical deflection along the peg over the course of the 5 protraction (Solomon and Hartmann, 2008; 2010; Huet et al., 2015; Huet and Hartmann, 2016). Friction will influence all mechanical parameters at the whisker base and is likely to introduce nonlinear effects into the mappings; this is an important area for future work.

3.4.4. The effects of head pitch and 3D mappings in whisker-centered coordinates

As stated above, the present work does not address the question of what happens when the rat pitches its head. Preliminary simulations (not shown) suggest that the mappings will shift but generally retain their uniqueness. For example, in the present work, with bregma aligned with lambda, several whiskers of the C-row showed slightly non-unique mappings. When the head is pitched upwards, whiskers of the C-row take on an orientation similar to that which the the B-row whiskers had previously. This suggests that the C-row whiskers would increase their uniqueness to match the B-row whiskers before them. The B-row whiskers, in turn, would be oriented more like the A-row whiskers.

In addition, the uniqueness of the present mappings is robust to sizable variations in whisking kinematics. As shown in Table 3.1, all simulations were first run with the kinematic equations of Knutsen et al., (2008), and then re-run after shifting these kinematic equations to the coordinate system of the morphological model (Towal et al., 2011). Although the mappings for individual whiskers varied to some degree, overall uniqueness was not strongly affected.

We also note that the mappings of the present work exploit only two of six possible mechanical variables (M_Y and M_Z). It seems likely that a third variable such as the axial force (F_X) or the twisting moment (M_X) could enable unique mappings across head pitch.

Finally, the present work has addressed only the mappings between single whisker contact and the location of a peg in head centered coordinates. A key unresolved issue is the extent to which mechanical signals at the whisker base can represent the 3D location of an object in whisker-centered-coordinates, including the height. If the 3D object-contact location can be determined based purely on tactile signals, then integration of this information across whiskers would permit the animal to obtain an impression of the objects contour or shape.

Acknowledgments

We thank Lucie Anne Huet for many useful discussions and assistance using the 3D model. We thank Per Knutsen and Ehud Ahissar for help interpreting the data and coordinate systems used in their 2006 paper.

This work was supported by NSF awards CAREER IOS-0846088 and EFRI-0938007, as well as NIH awards R01-NS093585 and R01-NS091439 to MJZH.

CHAPTER 4

Response characteristics of identified primary afferents in the rat vibrissal system

This chapter is adapted from a manuscript that has been submitted as "Furuta T, Yang AET*, Ebara S, Miyazaki N, Murata K, Hirai D, Shibata K, Kaneko T, Hartmann MJZ (submitted) Response characteristics of identified primary afferents in the rat vibrissal system."*

When compared with the visual or auditory systems, the peripheral transduction and coding mechanisms that underlie tactile sensation are as yet poorly understood. Here we exploited the unique morphology of the rat vibrissal (whisker) array to investigate coding and transduction properties of primary tactile afferents. Specifically, we performed in vivo intra-axonal recording and labeling experiments to quantify the responses of four types of identified mechanoreceptors in the vibrissal follicle. After accounting for three-dimensional vibrissal geometry, a simple, three-parameter mechanical model explained many features of the neural responses. Results also revealed a distinct anatomical basis for the difference between the responses of RS-Merkel and lanceolate endings. The present study systematically bridges between the architecture of the tactile sensing apparatus, the response properties of identified primary afferents, and the mechanics that describe touch. Aspects of the model could be applied to the study of more complex mechanical input.

4.1. Introduction

In comparison to sensory transduction in the visual and auditory systems, transduction mechanisms for mechanical stimuli in the somatosensory periphery are as yet poorly understood. During tactile stimulation of the hand, mechanical signal transmission involves both the material properties of the hand

(e.g., viscoelasticity), as well as mechanical-to-electrical transduction by the mechanoreceptors. The spatiotemporal dynamics of skin deformation during active touch is complex and difficult to measure, and depends on sweat, dirt, skin ridges, and hydration state. These factors make it difficult to quantitatively analyze the relationship between mechanical stimuli and the response of neural elements in the skin.

A related challenge in the field of somatosensation is that we have only incomplete information about peripheral response properties. Mechanoreceptors have been classified based on their morphologies (e.g., Merkel, Meissner, Pacinian and Lanceolate), as reviewed in Abraira and Ginty (Abraira and Ginty), but only recently have studies begun to directly characterize responses of identified endings (Li et al. 2011; Maksimovic et al. 2014). We still lack a general understanding of the relationship between tactile stimulus features (e.g., amplitude, velocity, direction, frequency), mechanoreceptor characteristics (type, size, number and location of endings) and response properties (magnitude, latency).

In the context of these challenges, the rat vibrissal (whisker) system offers a unique opportunity to investigate the responses of primary afferents to well-controlled tactile stimulation. Rats use $\sim$31 sensitive vibrissae on each side of the face for tactual exploration. There are no mechanoreceptors along the length of a vibrissa, instead, all tactile information is transmitted to the follicle at its base (Ebara et al. 2002; Whiteley et al. 2015). The vibrissal follicles contain an elaborate architecture to encode tactile input, incorporating a wide variety of mechanoreceptor types (Ebara et al. 2002), many of which are directly analogous to those in the hand.

Two recent studies demonstrated that the responses of primary vibrissal-related trigeminal afferents are better described with a generalized linear model (GLM) based on mechanical variables, rather than kinematic variables (Bush et al. 2016; Campagner et al. 2016). However, both studies were limited to a two-dimensional (2D) analysis, and the GLM approach provides almost no insight into the physical mechanisms behind neural response characteristics.

In the present work, we exploited the accessibility and highly regular morphology of the rat vibrissal (whisker) system to dissociate sensory geometry from the response of the mechanoreceptor itself. We specifically hypothesized that primary afferents possess a correlation between their mechanoreceptor types and angular tuning with respect to three-dimensional (3D) vibrissal mechanics, and also that intrinsic

curvature of the vibrissal shaft plays a large role in establishing the angular tuning. To test this hypothesis, we performed intra-axonal recordings as individual vibrissae were deflected with a piezoelectric transducer, and then labeled and visualized the morphologies of each nerve ending. A three-parameter mechanical model that accounts for the whiskers 3D geometry was then used to explain the correlation between response properties and mechanoreceptor type. This work is some of the first to reveal correlations between the structure and function of the peripheral tactile architecture.

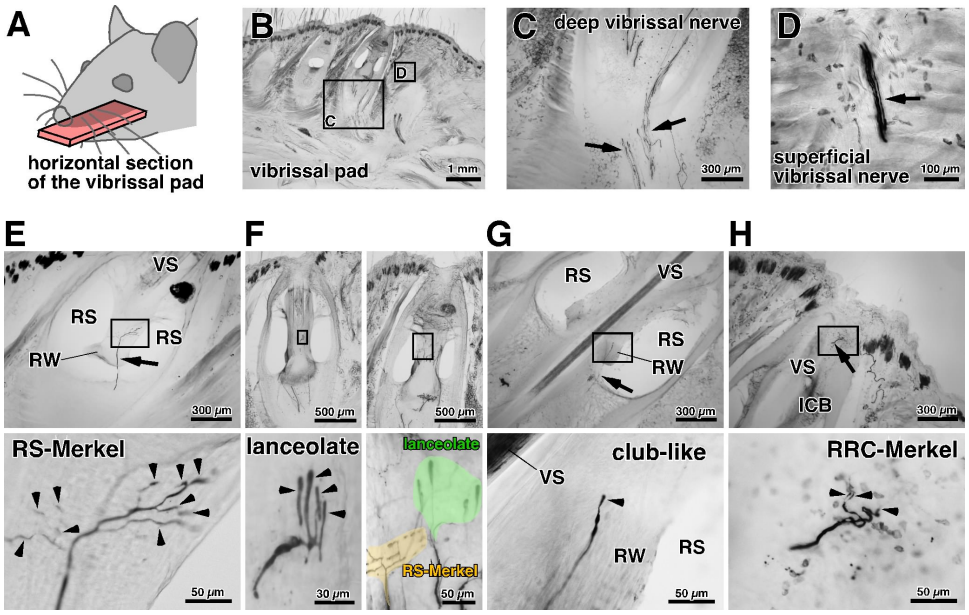

Figure 4.1. Bulk tracer injections reveal mechanoreceptor morphology and location within the follicle

(A) All sections were made parallel to the horizontal plane. **(B)** The main bundle of the infraorbital nerve divides into many small bundles under the vibrissal pad. **(C)** Deep vibrissal nerves enter into the follicles at the level of the cavernous sinus, indicated by arrows. **(D)** A second nerve bundle, which runs toward the surface of the skin, contains the superficial vibrissal nerve. **(E-H)** The deep vibrissal nerve gives rise to several types of nerve endings in the follicle: Merkel endings at the ring sinus level (RS-Merkel), lanceolate endings, club-like endings. The superficial vibrissal nerve provides Merkel endings at the rete ridge collar (RRC-Merkel). In each subplot, the bottom figure shows the expanded view in the region indicated by the rectangle in the top figure.

4.2. Results

4.2.1. The morphology of four types of mechanoreceptors in the vibrissal follicle

To visualize afferent fibers we performed bulk tracer injections into the infraorbital nerve and sectioned the pad horizontally (Fig. 4.1A). Consistent with previous findings (Ebara et al. 2002), the infraorbital nerve gave off thick fiber bundles that entered follicles at a deep level (the deep vibrissal nerve) as well as thin bundles that went toward the skin surface and branched into follicles at a superficial level (the superficial vibrissal nerve) (Fig. 4.1B-D).

Previous work (Ebara et al. 2002) has shown that the deep and superficial vibrissal nerves innervate several morphologically distinct types of mechanoreceptors, representative examples of which are shown in Fig. 4.1E-H.

In addition to the four types of endings identified in Fig. 4.1E-H, vibrissal follicles and the surrounding skin also contain other types of nerve endings, for example, circumferential fine- and small-caliber innervations, reticular endings, palisade endings, and free nerve endings. These ending types were not investigated further in the present study.

Disk-like nerve endings associated with Merkel cells are known as Merkel endings (Iggo and Muir 1969). The deep vibrissal nerve innervates Merkel endings at the level of the ring sinus (RS); these endings are called RS-Merkel and are illustrated in Fig. 4.1E. The deep vibrissal nerve also innervates lanceolate receptors and club-like receptors. Lanceolate endings (Fig. 4.1F) consist of longitudinal nerve endings and Schwann sheaths, and are located mainly at the level of the ring sinus. Club-like receptors (Fig. 4.1G), consist of club-like endings enveloped by Schwann sheaths, and in the present work were invariably found to be associated with the ringwulst. The superficial vibrissal nerve innervates a second category of Merkel cells, distinguished by their position near the rete ridge collar (RRC). These endings are termed RRC-Merkel endings and are illustrated in Fig. 4.1H. Importantly, each mechanoreceptor cluster associated with a single primary afferent axon covered only a small part of a follicle, whereas the totality of mechanoreceptors encircled the entire root of vibrissal shaft.

Given the diversity of identified mechanoreceptor types, an important open problem is to quantify the response characteristics of each type. These response characteristics can be measured only by recording directly from identified primary afferents using juxtasomal recordings.

4.2.2. Intra-axonal labeling and recording of primary afferents

To investigate the correlation between morphological characteristics and mechanoreceptor response properties, we performed intra-axonal recording and labeling in the infraorbital nerve. Each afferent responded to stimulation of one and only one vibrissa. When an intra-axonal recording was complete, the axon was

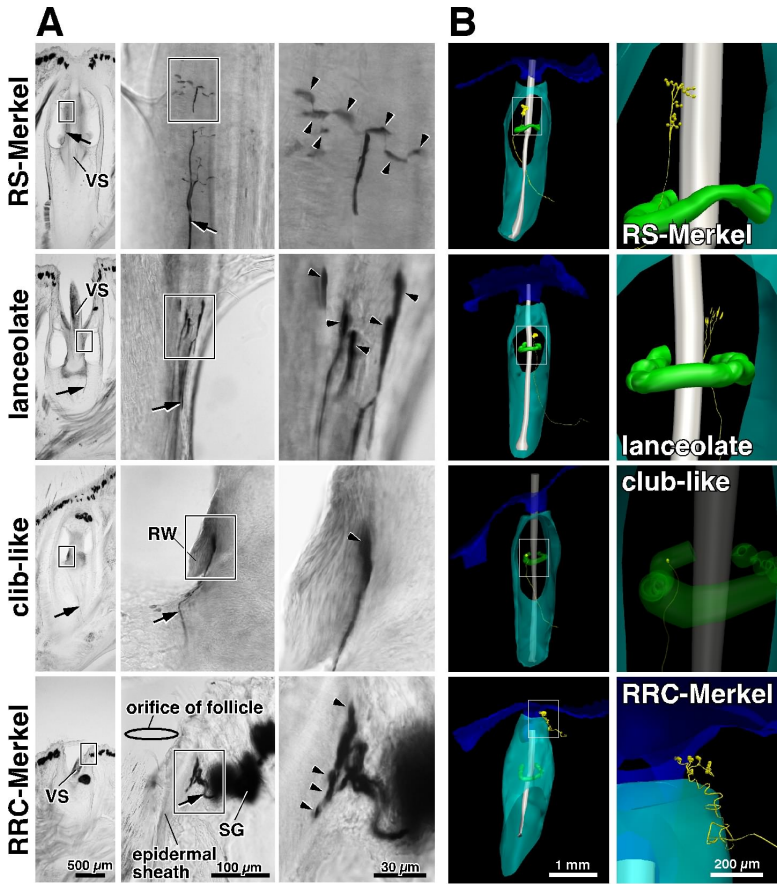

Figure 4.2. Representative axons and endings

(A) Morphologies labeled via intra-axonal injection. Arrows indicate trunks of labeled afferents. Arrowheads indicate peripheral endings. **(B)** Representative 3D-reconstructions of follicles that contained recorded axons. Axons and terminals are yellow while the skin, follicle capsule, vibrissal shaft and ringwulst are shown in blue, cyan, gray and green, respectively. Thickness of axons and size of terminals are exaggerated for visual clarity. The expanded view for each reconstruction shows a semi-quantitative rendering of the approximate shape of the mechanoreceptor terminals. In these expanded views, the scale along the longest dimension of the mechanoreceptor is quantitatively accurate. The scale in the other two dimensions is approximate, due to limitations of the light microscope equipped with the 3D Neurolucida tracing system.

injected with BDA to visualize the morphology of the nerve endings derived from single afferent fibers. Representative labeling of these terminals is shown in Fig. 4.2.

We obtained 30 labeled afferent fibers. Nine fibers were excluded from analysis: two fibers were excluded because they terminated in the skin between the vibrissae and appeared to have palisade endings; an additional seven fibers were excluded because BDA labeling was insufficient to determine receptor type.

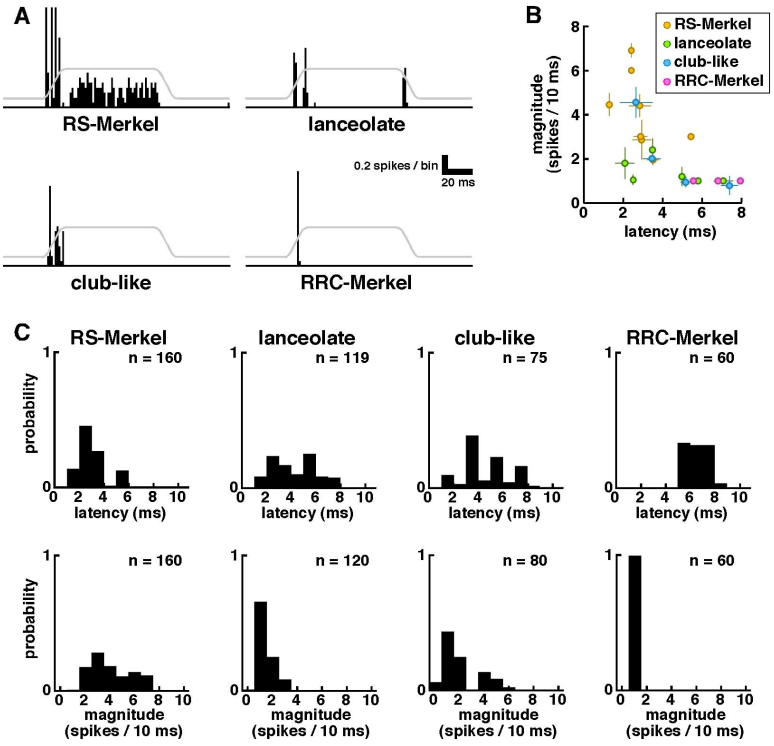

Figure 4.3. Response properties of primary afferents when the whisker is deflected in the afferents best direction

(A) Representative PSTHs (bin width: 1 ms) for the four mechanoreceptor types. Gray lines represent movement of the piezo stimulator with an amplitude of 5°. **(B)** Response latency and magnitude tended to be inversely related among the four mechanoreceptor types. All latencies and response magnitudes are calculated in the best stimulus direction. Error bars indicate standard deviations. **(C)** Histograms of latencies and magnitudes for all trials from all afferents, categorized by afferent type. In each subplot, n indicates the total number of trials. The mean, median, SD, and SEM for all histograms are available in the source data for Fig. 4.3.

This left a total of 21 afferent fibers available for further analysis. Of these 21, eight afferents had RS-Merkel endings, six afferents had lanceolate endings, four fibers had club-like endings and three had RRC-Merkel endings. Examples of each type are shown in the four rows of Fig. 4.2A. All 21 labeled axons were then reconstructed in three dimensions so that the location of axon terminals within the follicle could be clearly visualized. Four representative examples are shown in Fig. 4.2B.

Responses of primary afferents were quantified while a vibrissa was deflected with a ramp-and-hold stimulus (5° amplitude; 10 ms ramp up, 50 ms hold, 10 ms ramp down). Fig. 4.3A shows representative responses from each mechanoreceptor type when the whisker was deflected in the afferents best direction.

Slowly-adapting (SA) response characteristics were exhibited only by RS-Merkel endings, while lanceolate endings, club-like endings, and RRC-Merkel endings showed rapidly-adapting (RA) responses.Many, but not all, RS-Merkel endings exhibited OFF responses in stimulus directions other than the best direction (Fig. 4.11).Three of six lanceolate endings and three of four club-like endings showed clear OFF responses, while no OFF response was observed in RRC-Merkel endings.

Consistent with previous studies (Jones et al. 2004), all afferents exhibited highly repeatable firing patterns. Across all 20 trials of stimulation, seventeen of the 21 afferents exhibited less than 2 ms variation in onset latency (Fig. 4.3). Within the 10 ms onset ramp, nine of the 21 afferents exhibited no variation in spike magnitude, and nine showed a maximum magnitude variation of a single spike (Fig. 4.3). The three RRC-Merkel endings, as well as two of the six Lanceolate endings, always produced exactly one spike in the first 10 ms of firing.

When considered at the level of individual axons, latency and magnitude tended to be inversely correlated (Fig. 4.3B), and shorter latency ON responses were associated with more variable response magnitudes (Fig. 4.3).

The histograms of Fig. 4.3C indicate that RS-Merkel exhibited the shortest latency ($2.35 \pm 0.58ms$) and largest magnitude responses, while RRC-Merkel exhibited the longest latency ($6.75 \pm 1.2ms$) and the lowest magnitude (Fig. 4.3B). Lanceolate and club-like endings tended to have intermediate latencies ($4.05 \pm 1.69ms$ and $3.36 \pm 1.64ms$, respectively) and intermediate magnitudes. Rank-sum tests indicated that the responses of RS-Merkel afferents were different from those of each of the other three afferent types in both latency ($p < 1e^{-8}$) and magnitude ($p < 1e^{-15}$). Likewise, RRC-Merkel responses were different from those of all other afferent types in both latency ($p < 1e^{-13}$).and magnitude ($p < 1e^{-5}$). In contrast, rank-sum tests indicated that lanceolate and club-like endings could not be statistically distinguished in either latency ($p = 0.52$) or magnitude ($p = 0.10$).

4.2.3. The angular tuning of the neural response cannot be explained solely by the location of the nerve endings within the follicle

As schematized in Fig. 4.4A-B, the vibrissa was trimmed to a length of 5-mm and displaced in four orthogonal directions. The location of the nerve endings was then identified within this vibrissa-centered coordinate system. A representative 3D reconstruction of the vibrissal follicle, shown in Fig. 4.4D-E, illustrates one example of the spatial relationship between the vibrissa and the mechanoreceptor, in this case an RS-Merkel type axon. For this particular axon, the preferred angle was rostral and dorsal (Fig. 4.4C), consistent with the location of the mechanoreceptor endings (Fig. 4.4F); however, there was not always consistency between mechanoreceptor position and the angular tuning of each axon. Furthermore, most axons responded strongly to deflections in more than one direction and many exhibited strong OFF responses in multiple directions as well.

An overview of the variability in neural response associated with stimulus direction is shown in Fig. 4.5. Fig. 4.5A shows the large variety in response magnitude generated by 21 axons during vibrissal deflections in each of the four directions. Because our goal was to examine response magnitude and direction, responses in Fig. 4.5A are depicted as vectors. The identical data are illustrated in Fig. 4.11 "radar plots", a more traditional representation in the neurophysiological literature (Rutlin et al. 2014). The variation is striking, even within a single mechanoreceptor type.

For example, Fig. 4.5A shows that RS-Merkel type axons exhibit strong ON responses in multiple directions. Although the vector sum of the ON responses generally points towards mechanoreceptor location, there is a large spread (nearly 180°), and three axons exhibit ON responses in the direction opposite to mechanoreceptor location. OFF responses also occur for many different deflection directions, both in the direction of the mechanoreceptor and opposite to that direction.

In the case of lanceolate and club-like endings, the ON response is not strongly correlated with mechanoreceptor location. Only three of ten axons show a preferred angle within ±45° of the mechanoreceptor location. Five of ten axons have OFF responses, often strong and in multiple directions, while the remaining five have no OFF response at all.

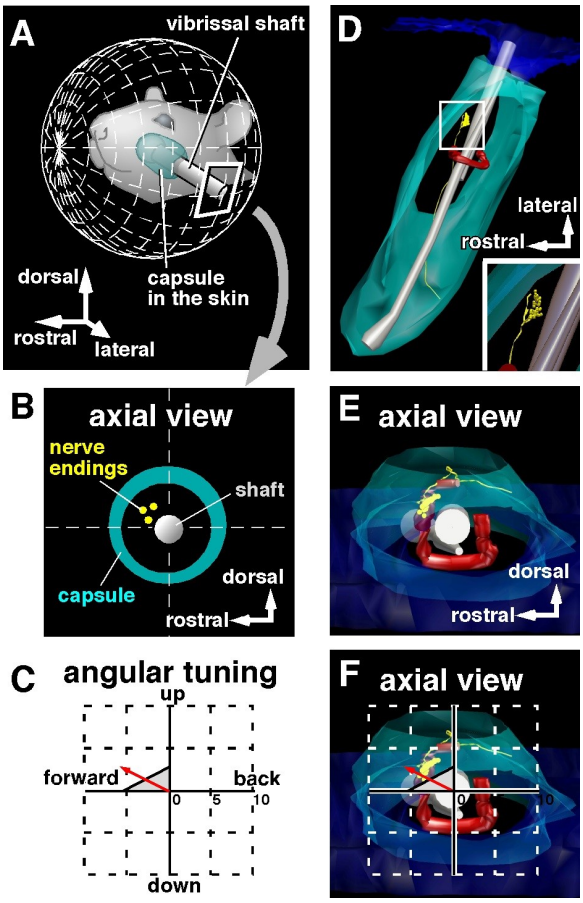

Figure 4.4. Correlation between location of endings and preferred angle

(A) Orientation of a vibrissa relative to the mystacial pad. **(B)** Locations of peripheral endings were projected into a plane normal to the axis of the vibrissal shaft. **(C)** A polar plot shows the response magnitude to each stimulus direction for the representative primary axon shown in (D-E). The red arrow is the vector sum of responses and indicates the axons preferred angle. The stimulus directions up, forward, down and back respectively correspond to dorsal, rostral, ventral, and caudal of the projected plane for the location of the peripheral ending. **(D)** A representative 3D reconstruction of a vibrissal follicle. Peripheral endings are yellow. **(E)** The reconstructed data is observed from a direction along the axis of the vibrissal shaft. **(F)** Note that the preferred angle shown in (C) corresponds closely to the location of the peripheral endings (yellow) of the afferent.

Finally, RRC-Merkel type axons exhibit exclusively ON responses, often equally robust in two completely orthogonal directions.

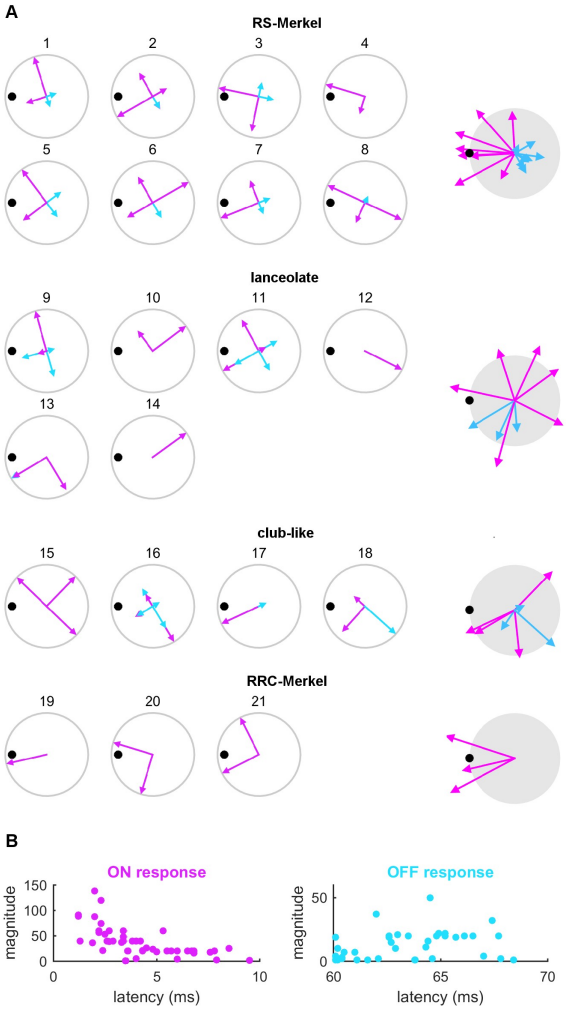

Figure 4.5. Axons exhibit a diversity of angular tuning profiles

(A) Responses of 21 axons to deflections in four directions (up, forward, back, and down). All subplots have been rotated so that the mechanoreceptor is at the same angular location. Pink vectors indicate the ON response magnitude when the vibrissa was deflected in each of the four directions, and the cyan vectors indicate the OFF response magnitude to those same deflections. The black dot in each circle indicates the mechanoreceptor location relative to the deflection vectors. Gray circles in the right-most column indicate the preferred angle of each afferent fiber shown in relationship to mechanoreceptor location, calculated as the vector sums of the ON and OFF responses for each axon. **(B)** Although latency generally varies inversely with magnitude, the correlation is not strong. Note that both subplots include responses when the whisker is stimulated in all four directions, while 4.3B shows only responses in the afferents best direction.

Correlational analysis indicated that the preferred angle of RS-Merkel and RRC-Merkel endings corresponded closely to the location of mechanoreceptors, while lanceolate and club-like endings exhibit no correlation between the two metrics (Fig. 4.5A).

Turning to Fig. 4.5B, it is clear that the latency of both ON and OFF responses exhibits considerable variability. Note that in contrast to Figure 3D, Fig. 4.5B shows response latency and magnitude when the whisker is stimulated in all four directions. Latency and magnitude are not strongly correlated. Furthermore, stimulating in the best direction does not necessarily ensure the shortest latency response: four of 21 axons had a shorter latency response in a direction other than that which generated the largest magnitude response.

If asked to summarize the results of Fig. 4.5, one might say only that it would appear challenging to account for the different response magnitudes and latencies as the vibrissa is pushed in each of the four different directions. We aimed to generate a mechanical model that could explain these data, for all 21 axons and all four directions.

4.2.4. The simplest mechanoreceptor model: an overview

We aimed to create the simplest possible mechanical model to explain the observed variability in response magnitudes and latencies as the vibrissa is pushed in each of the four different directions. Model details are provided in Supplemental Experimental Procedures. In line with the view that whisker displacement causes unique pattern of deformation within the follicle (Whiteley et al. 2015). A mechanoreceptor is modeled as a spring-mass-damper system driven by a forcing function f, which is a linear weighted sum of the mechanoreceptors presumed sensitivity to three mechanical signals at the whisker base: bending moment, axial force, and twisting moment (M_B, F_X, and M_X).

The first modeling step was to simulate the mechanical signals (M_B, F_X, and M_X) at each whisker base in response to the ramp and hold deflection delivered to the whiskers. It is important to note that the mechanical response of each vibrissa in the array is altered by its individual geometry. Each vibrissa has a unique intrinsic curvature and emerges from the vibrissal pad at a unique set of angles (Knutsen et

al. 2008; Towal et al. 2011). These different geometries are illustrated in Fig. 4.13for the D5 and gamma vibrissae.

When vibrissae are deflected forward, back, up, and down as defined in Fig. 4.4C, they will be displaced very differently in vibrissa-centered coordinates due to their intrinsic curvature and emergence angles. These geometrical asymmetries will necessarily induce differences in mechanics at the vibrissa base (Huet et al. 2015; Huet and Hartmann 2016; Quist and Hartmann 2012).

We computed all components of moment and force during simulated 5° deflections of the 31 vibrissae in the array for all four directions (Fig. 4.6A and Section 4.4). In each direction, the four parameters that will determine the vibrissas displacement in the follicle (and hence the force that it will exert on mechanoreceptors) are the magnitude of the bending moment ($M_B = \sqrt{M_Y^2 + M_Z^2}$), the direction of bending moment ($M_D = \arctan M_Z M_Y$), the magnitude of the axial force (F_X) and the magnitude of the twisting moment (M_X). The remaining two parameters, F_Y and F_Z, are neglected because they are strictly correlated with M_Y and M_Z , given that contact occurs at a constant distance from the base of the vibrissa.

All mechanical signals were then normalized between -1 and 1 and used to determine the forcing function, f:

$$f = M_B \frac{1 + \cos \Delta\theta}{2} + w_{FX} F_X + w_{MX} M_X \tag{4.1}$$

In equation 4.1, w_{FX} and w_{MX} are weighting constants. The weight w_{FX} is dimensionless, while w_{MX} has units of inverse length. The cosine factor in the M_B term accounts for the anisotropy of M_B with respect to the follicle circumference, where $\Delta\theta$ represents the angular difference between the direction of vibrissa deflection (i.e., M_D as shown in Fig. 4.6C and 4.4B) and the mechanoreceptor location (see Fig. 4.13).

The dynamics of the mechanoreceptor are then modeled as a spring-mass-damper system:

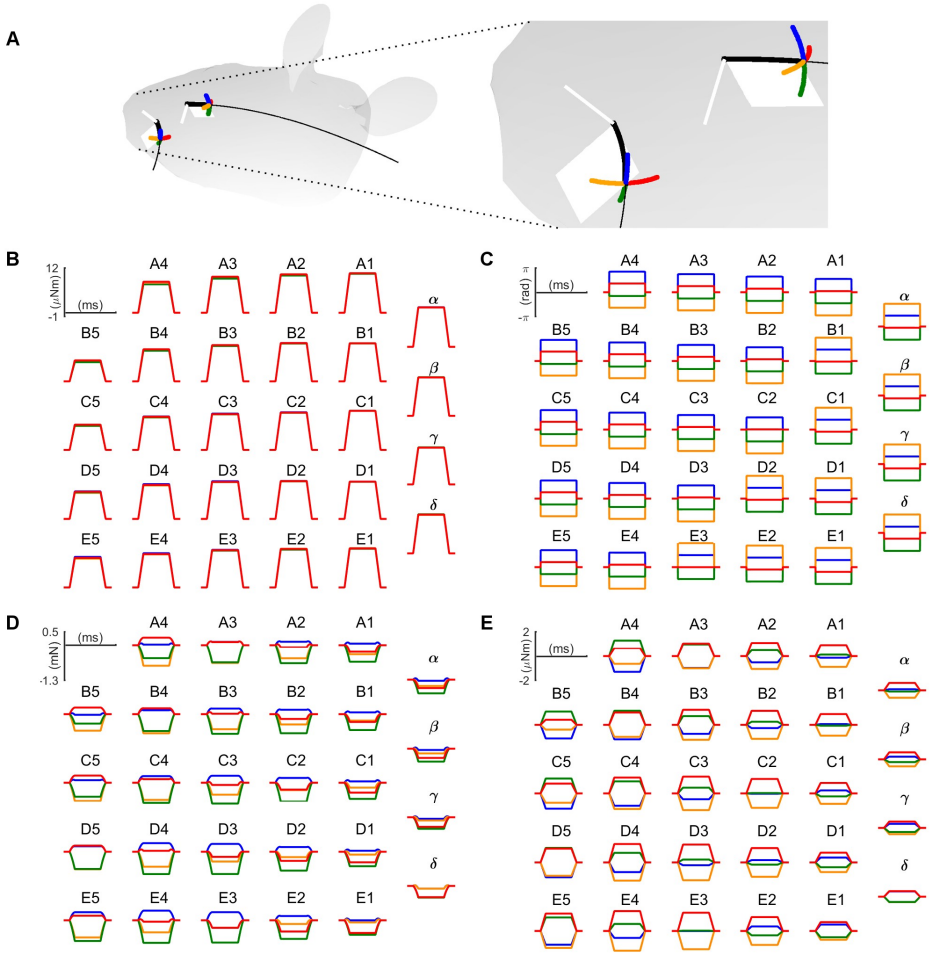

Figure 4.6. Geometry and mechanics of the present modeling of vibrissae in the array

(A) The D5 and gamma vibrissae are illustrated with the rats head placed to align bregma with lambda, as in experiments. Thin and thick black lines indicate vibrissal shape before and after trimming to $5mm$. The two vibrissae emerge from the face at very different 3D angles and have different intrinsic curvatures. These different geometries will strongly affect the mechanical responses generated by deflection in the four directions indicated. White trapezoids indicate the x-y planes that contain the two vibrissae. Solid white lines represent the z-axes normal to these planes. The colors associated with the different directions indicate the color code used throughout the manuscript: red is caudal, yellow is rostral, blue is dorsal and green is ventral. For visual clarity, all four deflections are exaggerated to 25° instead of 5°. **(B–E)** The four curves in each subplot show one component of the mechanical response to deflection of the vibrissa in each of the four directions. In all simulations the ramp time was 10 ms and the hold time was 50 ms to match experimental conditions. **(B)** Bending moment MB shows similar responses across all vibrissae in all deflection directions. **(C)** Each vibrissa responds very differently to the identical stimulation for MD. **(D)** Each vibrissa exhibits a very different F_X response to the identical stimulation. The more caudal whiskers (e.g., arc 1) often have small transients at stimulation onset and offset. **(E)** Each vibrissa exhibits a very different M_X response to the identical stimulation.

$$f = m\ddot{x} + c\dot{x} + kx \tag{4.2}$$

where m is the mass, c is the damping coefficient, and k is the spring constant The models output is the variable x, which represents mechanoreceptor position (displacement) as a function of time.

The model was optimized in two separate steps. First, for each axon, a linear optimization found the two weights that best matched the forcing function to the magnitudes of the neural response for all four deflection directions. Although the model optimizes response magnitude in all four directions simultaneously, only two weights can be varied in the optimization. Mathematically, this amounts to solving a system of four equations and two unknowns, and there is no guarantee that a solution even exists.

Second, the value of the spring constant k was set to 1, and the values of m and c were varied to match experimental and simulated response latencies. To do this, a single threshold (constant across all four directions) was imposed to determine whether the axon would fire; crossing the threshold determined the response latency, and values of m and c were optimized for each axon

The model output x serves to predict the neural responses recorded in experiment. The highest amplitude of x predicts the response magnitude (intensity), and the timing when x crosses the threshold predicts the response latency.

The optimal m, c, and threshold for each axon were chosen to minimize one overall error, which is the linear combination of the errors of magnitude and latency at the ratio of $9:1$.

Given the models extreme simplicity, it is important to set clear expectations for its ability to predict the magnitudes and latencies shown in Fig. 4.5. The model includes no information about mechanoreceptor biophysics: it assumes that the axon maintains the same sensitivity (i.e., the same weights) regardless of whether it is being deformed or released. As a result, simulated ON and OFF responses necessarily depend on each other. The model may not be able to predict the magnitude of the OFF response if an ON response has already occurred in that direction.

Finally, the model contains no term that would permit the spring-mass-damper system to adapt to the hold portion of the stimulus. The model is expected to predict response magnitude and latency only during ON and OFF windows; it cannot be expected to predict adaptation characteristics of the neuron or its response during the hold period.

4.2.5. Simulated responses are a good match to experimental data across all axons

In this section we will examine and evaluate simulation results in the order of individual axons, axons within each type, and all axons.

For each individual axon, visualized comparison between simulation and experiment for all directions are shown in Fig. 4.7 in the form of bar graphs. Each subplot displays results for an axon. The interpretation of these subplots is that the more similar the top half of the figure resembles the vertical mirror-image of the bottom half, the better the simulation predicted the experiment results. The magnitude and latency are qualitatively shown as the length and x-location of each bar, respectively. The number of total responses the simulation aimed to match is 168, as a result of 21 axons, 4 directions (dorsal, rostral, ventral, and caudal), and two windows (onset and offset).

Simulation results showed only 12 mismatches between experiment and simulation, all of which are false negatives, detailed as follows: axon 2 rostral off, neuron 8 caudal off, neuron 9 dorsal off, neuron 9 ventral off, neuron 11 rostral on, neuron 11 rostral off, neuron 11 caudal off, neuron 13 dorsal off, neuron 16 dorsal off, neuron 16 rostral off, neuron 16 ventral off, neuron 16 caudal off. All mismatches can be attributed to either of the following possible reasons:

- Mechanical limitation (over-constrained), happening only to the smallest response magnitude
- Asymmetry (having both ON and OFF responses)

We next compare results within each type. Fig. 4.8A shows summary of each type in an alternative format. With all responses of the same type rotated based on mechanoreceptor angular location and overlaid, one vector plot is made for simulation and another for experiment. The similarity between the two plots demonstrates the quality of prediction.

On top of the figure, more quantitative measures for each type are provided below.

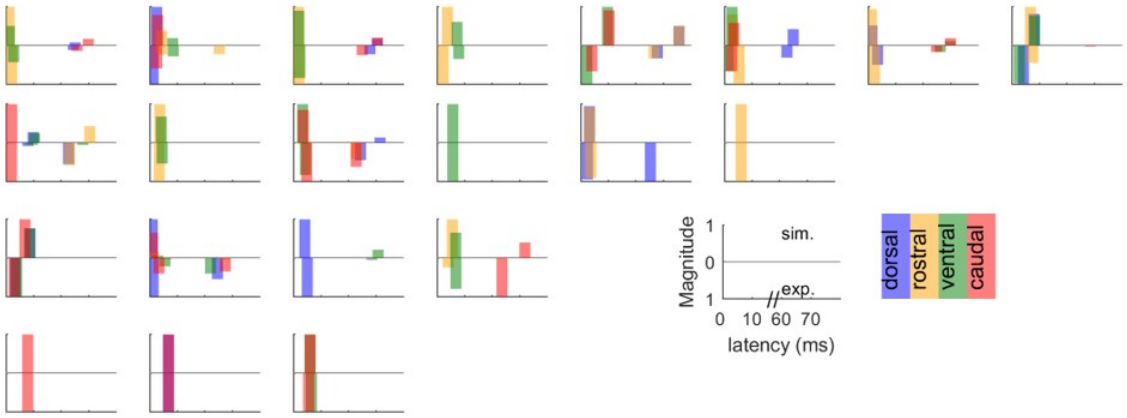

Figure 4.7. Simulation results compared to experiment in detail
Each panel shows results for one receptor type. Each plot shows responses from a different axon. The bottom half of each plot shows the latency (x-location of bars) and magnitude (length of bars) recorded in experiment, and the top half shows the corresponding dynamic mechanoreceptor response predicted by the model. The colors are associated with the different directions, labeled by the legend at the bottom right. The axis labels are shown on the bottom right subplot. The hold region of the simulated response is not shown (the x-axis has a break point) because the model cannot predict adaptation characteristics or the neural response during the hold period.

RS-Merkel has the highest number of axons and thus that of responses. Eight axons yield 64 possible responses. Most of the responses (62) were correctly predicted aside from two false negative responses (both are off-responses), including 33 true negatives and 5 correctly predicted maximum normalized response. Among the 29 true positives and true negatives, the magnitude between simulation and experiment has high coefficients of correlation for onset and offset ($R = 0.938$ and $R = 0.960$). The latency prediction during onset and offset windows are positively correlated ($R = 0.497$ and $R = 0.784$).

Lanceolate has the second highest number of axons. Six axons yield 48 responses to predict. Most of the responses were also correctly predicted, although there are a total of six false negative responses (one on-response, five off-responses). Lanceolate prediction included 29 true negatives and 13 true positives (four of the true positives are correctly predicted maximum normalized response). The magnitude between simulation and experiment has high coefficients of correlation for onset and offset ($R = 0.986$ and $R = 0.931$). The latency prediction during onset and offset windows are positively correlated ($R = 0.958$

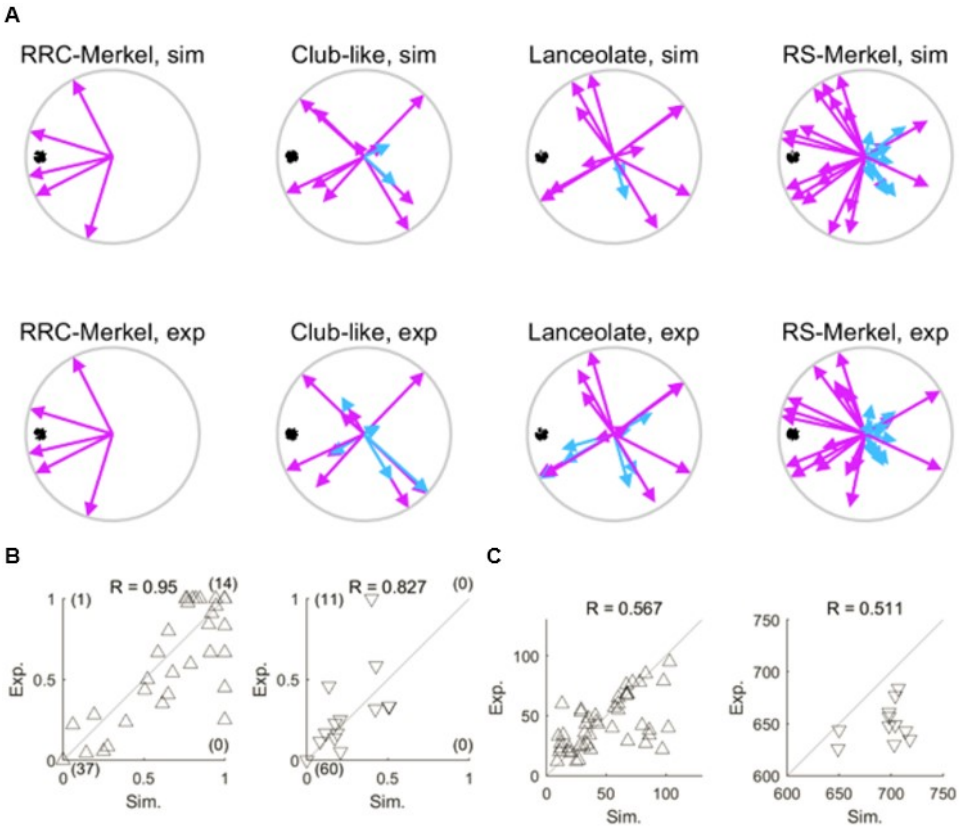

Figure 4.8. Summary plots showing simulated responses closely matching experimental data. **(A) Overlaid vector plots.** The response magnitude and direction predicted by simulation (top) is compared with response magnitude and simulation from experiment (bottom). Response magnitude and direction are plotted as vectors for ON (purple) and OFF (cyan) responses. Each circle contains results from 8, 6, 4, and 3 neurons, respectively, belonging to the type specified in the title. Note that even though all whiskers were deflected to the dorsal, rostral, ventral, and caudal directions, the vectors for each neuron have been reoriented based on the angular location of the associated mechanoreceptor on the circumference of the follicle, so as to overlay results from one neuron on top of another. **(B) Magnitude.** Normalized response magnitude in simulation (x-axis) and experiment (y-axis). Three subplots contain results for on-responses and off-responses, respectively. Triangles pointed upwards have positive values for magnitude and represent the ON response. Triangles pointed downwards have negative values for magnitude and represent the OFF response. The number at (0, 0) indicates the number of zero-responses that were successfully fit (true negative). The numbers at (0, 1) and (1, 0) indicates the number of false negative and false positive responses, respectively. The number at the point (1, 1) indicates the number of simulated responses that exactly matched the largest experimental magnitude for that axon, normalized to one. **(C) Latency.** Response latency in simulation and experiment. For all deflections for which the magnitude was predicted correctly, the latency of predicted and experimental response is compared. The values for R are shown separately for ON (upwards pointing triangles) and OFF (downwards pointing triangles) responses.

and $R = 1$). The offset latency has a high correlation coefficient because there are only a total of two responses predicted.

Club-like prediction is the weakest out of all four axon types in this study. Subtracting the four false negative responses, all of which are off-responses, 28 out of 32 responses were correctly predicted, including 16 true negatives and 2 correctly predicted maximum normalized response. The magnitude between simulation and experiment has coefficients of correlation slightly lower than the above two types for both onset and offset ($R = 0.870$ and $R = 0.903$). The latency prediction during onset and offset windows are much more weakly correlated ($R = 0.076$ and $R = -1$). Note that the offset latency here also only a total of two responses predicted. It is also worth noting that even though latency correlations are low when viewing the onset and offset windows separately, the model successfully predicted 10 non-zero responses to be in either of the correct $10 - ms$ size windows, out of a total of 100 ms timeframe. The latency correlation coefficient when viewing the entire timeframe continuously would be $R = 0.992$.

RRC-Merkel prediction has the highly quality out of all four, in part because it has the least number of axons and responses. The absence of off-responses in RRC-Merkel also reduced the complexity of prediction required. There are no false predictions in this type. Out of all 24 possible responses, 19 are true negatives, and the remaining five are all true positives. The magnitude between simulation and experiment has a perfect coefficient of correlation ($R = 1$). The latency prediction during onset is also the highest among all types ($R = 0.902$).

Finally, to evaluate the prediction for all axon as a whole, Fig. 4.8B-C shows the overall summary figures for magnitude and latency. Correlation of magnitude is strong, exhibiting R values of 0.950 and 0.827 for ON and OFF responses, respectively. Out of the 168 deflections that the model could be expected to fit, it fit the magnitudes of 59/71 non-zero responses, and 97 zero responses, for a total of $156/168 = 92.9\%$ correct.

Correlation coefficients for 57 non-zero responses were calculated in Fig. 4.8C for ON and OFF responses separately. Correlations are better for ON responses than OFF. Although the exact latencies vary, the key feature is that all simulated responses are predicted within the correct 10-ms ON and OFF windows, as a result of the combined effect of the weights, the dynamic response, and the threshold.

4.2.6. The anatomy associated with the differential mechanics of RS-Merkel and lanceolate responses

The results above indicated that many features of primary afferent coding can be explained by a simple spring-mass-damper model, provided that the vibrissas 3D geometry is considered. Each afferent has different sensitivities (weights) to different mechanical signals (M_B, M_X, and F_X). These variations in weights are equivalent to differences in mechanoreceptor geometry, orientation, branching pattern, and location in the follicle.

Club-like endings are found near the ringwulst, whereas RRC-Merkel endings are always localized near the follicle mouth (Fig. 4.1) (Ebara et al. 2002). These location differences could explain response differences between the two mechanoreceptor types. In contrast, RS-Merkel endings and lanceolate endings were found at similar locations relative to the ring sinus (Fig. 4.1), but exhibited quite different response characteristics. We therefore compared the detailed architecture of RS-Merkel and lanceolate endings at an electron microscopic level.

Myelinated axons running in the inner connective tissue sheath and traversing the intermediary zone were found to give off thin branches that pierced the glassy membrane (Fig. 4.9A-C). At increased spatial resolution, RS-Merkel endings, presumed to connect with these thin branches, were localized in the deepest layer of the epithelial sheath (Fig. 4.9D). In contrast, lanceolate endings were located in a loose space between the glassy membrane and connective tissue sheath (Fig. 4.9E) (Takahashi-Iwanaga 2000). 3D reconstruction of ultrastructure at the level of the ring sinus (Fig. 4.9F-G) clearly revealed the different spatial arrangements of these two kinds of mechanoreceptors.

Each Merkel cell was always localized between the discoid varicosity of its associated Merkel ending and the glassy membrane. This geometry is exactly reversed from the spatial relationship found in the skin, where discoid varicosities of Merkel endings are localized between Merkel cells and the basement membrane (Iggo and Muir 1969). In the case of lanceolate endings (Fig. 4.9E), we confirmed that one side of the longitudinal axon terminal contacted the deeper side of the basement membrane, while the other side of the axon terminal made contact with the connective tissue sheath (Takahashi-Iwanaga 2000). The anatomical differences between RS-Merkel and lanceolate endings are summarized in Fig.

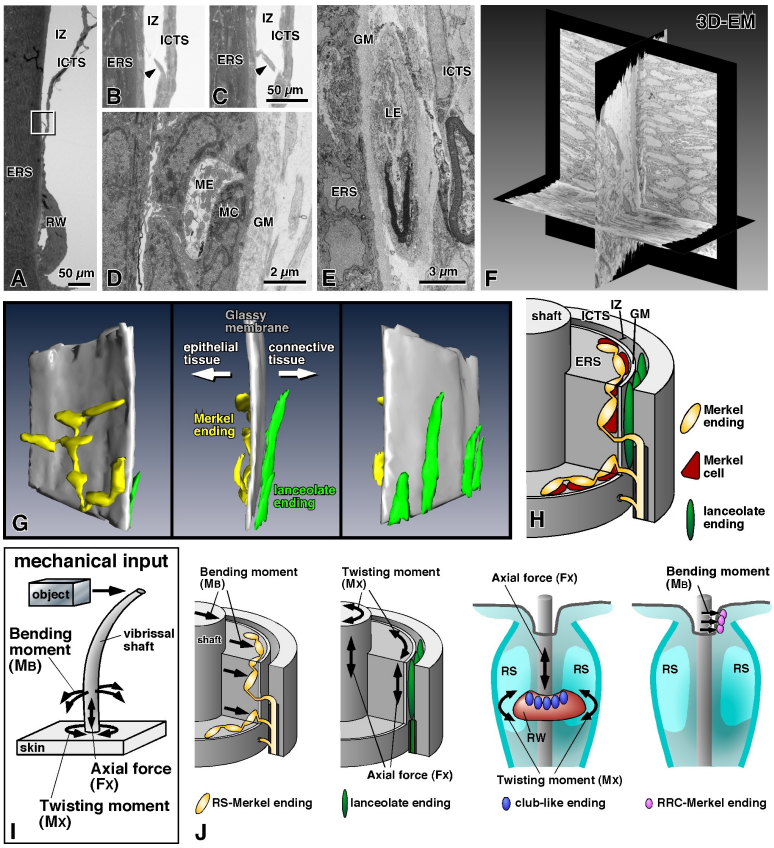

Figure 4.9. Ultrastructure of RS-Merkel and lanceolate endings

Abbreviations: ERS: epithelial root sheath; IZ: intermediary zone; ICTS: inner connective tissue sheath; RW: ringwulst; ME: Merkel ending; MC: Merkel cell; GM: glassy membrane (basement membrane); LE: lanceolate ending; 3D-EM: Three-dimensional electron microscopy. **(A)** Semi-thin section parallel to the axis of the vibrissal shaft. **(B, C)** Magnified views of the rectangle in panel (A) were obtained from two sequential semi-thin sections. Arrowheads indicate an axon branch piercing the glassy membrane to enter the ERS. **(D)** RS-Merkel endings are distributed in the most lateral layer of the ERS. **(E)** Ultrastructure of a lanceolate ending. **(F)** Three orthogonal planes of the stack data obtained with a scanning electron microscopic system. **(G)** Sequential EM images of nerve endings at the level of the ring sinus were reconstructed in 3D (gray, glassy membrane; yellow, Merkel ending; green, lanceolate ending). RS-Merkel endings are located in the epithelial sheath while lanceolate endings are localized in the loose space in between the glassy membrane and the connective tissue. **(H)** A schematic representation of Merkel and lanceolate ending innervation at the level of the ring sinus. **(I)** Mechanical input to the tip of a vibrissa is transduced by the vibrissal shaft, which has an intrinsic curvature. The mechanical signal is decomposed into three mechanical components: bending moment (M_B), axial force (F_X) and twisting moment (M_X). **(J)** The sensitivity of each mechanoreceptor is dependent upon its location and the surrounding structure. Each mechanoreceptor has a different sensitivity to the different mechanical components.

4.9H. Intuitively, the schematic suggests that these two mechanoreceptors types will experience different mechanical signals during vibrissa stimulation.

Taken together, the intra-axonal recordings, theoretical model, and 3D-EM analysis suggest the perspective depicted in Fig. 4.9I-J. Mechanical input near the vibrissal tip is transmitted by the vibrissal shaft, whose intrinsic curvature alters the three mechanical signals at its base. Each mechanoreceptor has a different sensitivity to the mechanical components, depending on its type, location, and orientation. Primary afferents responses are determined by a combination of the mechanical processing of the vibrissal shaft and the differential sensitivity of each mechanoreceptor.

The primary afferent response to bending moment depends almost entirely on the angular difference between mechanoreceptor and the bending direction (Fig. 4.6 and 4.13). The Merkel endings, which lie directly against the glassy membrane, are thus in an ideal position to respond strongly to bending moment in directions that correspond closely to the location of the mechanoreceptor (Fig. 4.5), at very short latency (Fig. 4.3B). In contrast, the effect of the axial force F_X is isotropic regardless of the circumferential position of mechanoreceptor in the follicle, and the twisting moment M_X depends on vibrissal curvature. A lanceolate ending is in an ideal position to respond to these signals because its two sides are connected between the glassy membrane and the connective tissue sheath: it will be responsive to shearing between these two structures. The isotropic nature of the axial force offers an explanation for why the lanceolate axonal response does not appear to be correlated with ending location (Fig. 4.5).

4.2.7. Confirming the importance of vibrissa curvature

To further validate the mechanisms proposed above, we confirmed the importance of the vibrissas intrinsic curvature by experimentally modifying the vibrissas shape (Fig. 4.10). After recording primary afferent responses to stimulation of a vibrissa trimmed to a length of $10mm$, we altered the intrinsic curvature of the vibrissa by clipping and bending the vibrissa with heated microforceps. Vibrissae were normally oriented concave rostral and a bit ventral, so we bent them caudal and dorsal. After the position of the stimulator was re-adjusted, the response of the same axon with the bent vibrissa was then recorded and compared with response with a normal vibrissa (Fig. 4.10). All six primary afferents tested exhibited a

significant response change in at least one stimulus direction. Across all 24 trials, 6 trials significantly increased response and 5 showed a decreased response, indicating that the shape of vibrissal shaft has a strong effect on the primary afferent response properties.

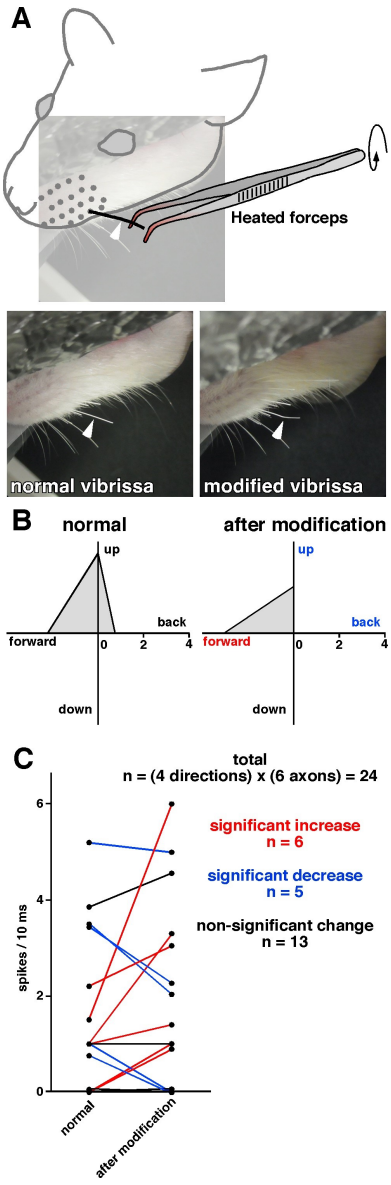

Figure 4.10. Effect of modifying vibrissa shape

(A) The vibrissa was bent with heated forceps. Photos show the vibrissa before and after bending. Arrowheads point to the curvature change. **(B)** Polar plots show response magnitudes evoked by vibrissa deflection toward the four directions before and after vibrissa-shape modification. In this particular example, the response to forward deflection was significantly increased while responses to upward and backward deflections were decreased. **(C)** We tested the effects of vibrissa-shape modification in six axons (4 directions x 6 axons = 24 trials). Vibrissa-shape modification increased responses in 6 trials and decreased in 5 trials, while no significant change was observed in 13 trials. Importantly, all 6 axons exhibited significant changes (increase and/or decrease) in at least one deflection direction.

4.3. Discussion

The present work delineates for the first time the direct correspondence between the morphological characteristics of four different mechanoreceptors types and their response properties. Mechanical modeling demonstrates that 3D vibrissal geometry plays a key role in determining both the magnitude and angular sensitivity of primary afferent responses. The results reported here thus begin to establish a systematic dataset to understand vibrissal somatosensation: the stimulus is precisely controlled, the mechanics and geometry are quantified, the recording is identifiable, and the morphology of the recorded nerve elements is verified.

4.3.1. Associating receptor type with response profile

Recent genetic approaches have provided insight into the molecular mechanisms that underlie tactile sensing and have helped to establish a direct link between mechanoreceptor type and response properties (Lumpkin and Caterina 2007; Walsh et al. 2015; Zimmerman et al. 2014). Particular progress has been made in the study of lanceolate and Merkel endings.

4.3.1.1. Lanceolate endings. A recent study of mouse hairy skin afferents (Li et al. 2011) tested the prediction that lanceolate endings should exhibit RA responses (Price et al. 2000). Results showed that lanceolate endings associated with A-beta or A-delta fibers were always RA, but those associated with C-fibers exhibited intermediate adaptation characteristics (Li et al. 2011). The present work finds that lanceolate endings in the vibrissal follicle always exhibit RA responses, consistent with the strong resemblance of vibrissae to guard hairs, which are innervated only by A-beta fibers.

The present study could also help explain why lanceolate endings associated with different fiber types appear to exhibit different adaptation properties. Lanceolate endings are associated with guard hairs, zigzag hairs, and Awl/Auchene hairs (Li et al. 2011). Fig. 4.6 of the present work suggests that the intrinsic curvature of Awl/Auchene hairs and the eponymous shape of zigzag hairs would generate high variability in F_X and M_X in the follicle. Assuming that lanceolate endings are sensitive to these signals (Fig. 4.8), subtle differences in mechanoreceptor location, surrounding structure, or receptor morphology between the three lanceolate subtypes of the hairy skin could significantly change response properties.

4.3.1.2. Merkel endings. Merkel endings are associated with Merkel cells, and a recent series of papers has explored the function of the channel protein Piezo2 in this cell type (Bautista and Lumpkin 2011; Coste et al. 2010; Ikeda et al. 2014; Maksimovic et al. 2014; Ranade et al. 2014; Woo et al. 2014; Woo et al. 2015). Piezo2 was shown to generate a mechanically-induced current in Merkel cells, demonstrating that these cells act as a primary site of mechanical transduction (Ikeda et al. 2014; Maksimovic et al. 2014; Ranade et al. 2014; Woo et al. 2014). The same set of studies showed that deprivation of Piezo2 or Merkel cells reduced SA responses, indicating that Merkel endings are SA type afferents.

The present intra-axonal labeling studies confirm that RS-Merkel endings in the vibrissal follicles exhibit SA responses at a single axon level. Intriguingly, however, we found that RRC-Merkel endings responded with RA characteristics. Our results also demonstrate a striking anatomical correlate of these different adaptation properties in the form of a morphological difference between individual Merkel disks of RRC-Merkel compared to RS-Merkel endings (Fig. 4.9). For RRC-Merkel endings, the Merkel cell lies between the neuronal terminal and the epithelial cell, while for RS-Merkel endings, the Merkel cell lies between the basement membrane and the neuronal terminal.

Our recordings of RS-Merkel endings also confirmed that adaptation characteristics of the trigeminal afferents can appear to change depending on stimulus direction (Jones et al. 2004). Three of eight RS-Merkel endings exhibited RA responses in non-preferred directions. The reason for the apparent change is that the mechanics of stimulation vary depending on the vibrissas intrinsic curvature.

Afferent encoding mechanisms thus clearly involve both the intrinsic physiological properties of each mechanoreceptor type as well as structural features and location of the end organ. In addition, an important contribution to the primary afferent response is the architecture of the tactile sensing apparatus, specifically, the 3D geometry of the vibrissa.

4.3.2. The importance of 3D vibrissal geometry

The present study finds that the 3D geometry of the vibrissa helps determine how a primary afferent will respond. Each vibrissa has a different intrinsic curvature and emerges from the mystacial pad at a different angle (Knutsen et al. 2008; Towal et al. 2011). Our results demonstrate that even when

a vibrissa is cut to 5mm, these geometric features are important in determining how information is transmitted along the vibrissa length to the receptors within the follicle.

Our mechanical analysis highlights that the effect of bending moment (M_B) will depend strongly on the direction of vibrissal deflection relative to the mechanoreceptor location in the follicle (M_D). This angular sensitivity was expressed as a cosine function (equation 4.1 and Fig. 4.13 in Supplemental Experimental Procedures, Section 4.4) because it yields a good approximation to the directional tuning curves ("radar plots") observed in studies of primary afferent responses (Rutlin et al. 2014).

Unlike the relatively smooth angular tuning associated with M_B, the axial force (F_X) and torsional moment (M_X) often vary with deflection angle in highly unintuitive ways (Fig. 4.6). The F_X and M_X signals change with deflection direction because the vibrissa has an intrinsic curvature, but the exact manner in which they change depends on an interaction between curvature and the angles of emergence. To confirm this result, simulations were run in which the vibrissa was completely straight; in this case neither F_X or M_X changed significantly with deflection direction.

The present work thus confirms and significantly extends results from a study of mouse hairy skin which demonstrated strong rostrocaudal tuning in Aδ lanceolate endings (Rutlin et al. 2014). This previous study found that the tuning was primarily attributable to an anisotropic distribution of endings in the hair follicle, i.e., the angular location of the mechanoreceptors in the follicle. The present work confirms the importance of mechanoreceptor location for the M_B signal, and then further demonstrates that the responses of some afferents– specifically, those with a sensitivity to F_X and M_X will also depend on the vibrissas intrinsic curvature and its resting orientation relative to the skin. The F_X and M_X signals are independent of the mechanoreceptors circumferential location within the follicle.

The F_X and M_X signals can play an important role even when the vibrissa in only $5mm$ long, but the effect of vibrissal geometry on primary afferent responses will be even stronger when the vibrissae are untrimmed and bending is a larger effect (Bagdasarian et al. 2013; Huet et al. 2015; Huet and Hartmann 2016; Solomon and Hartmann 2006; Solomon and Hartmann 2011).

4.3.3. Advantages and limitations of the simple spring-mass-damper model

The mechanical model in the present work is remarkably simple. Only two parameters (weights) are used to predict the magnitude of the neural response in four deflection directions. Because this problem is "over-constrained", there is no mathematical guarantee of a solution. One would not a priori expect to find a solution that satisfies all four equations simultaneously. Not only did this three-parameter model arrive at a solution in two phases and all four directions for all 21 afferents, but the predicted magnitudes were an excellent match for experimental results in 156/168 deflections.

These results thus demonstrate that a simple spring-mass-damper model can explain the magnitude of ON and OFF responses of primary vibrissal afferents at the 10 ms time scale, provided that the driving function includes the effects of 3D vibrissal mechanics. Notably, the simulated response magnitude is determined by a forcing function based entirely on quasistatic bending: no effects of collision or vibration are included.

The present model complements previous detailed models of mechanoelectrical transduction within the follicle that have included integrate and fire models of the primary afferent and use a total of either 17 (Mitchinson et al. 2004) or nine (Lottem and Azouz 2011) parameters. The philosophy of the present work was to use the simplest possible model to explain response magnitude and latency as a function of deflection direction.

A significant limitation of this approach is that the model cannot predict adaptation characteristics, so the prediction during the hold stimulus is not meaningful. A second limitation is that it cannot explain the magnitude of the OFF response if an ON response has already occurred in that deflection direction, because mechanical inputs have the same sensitivities (weights) for simulated stretch and release.

One possible approach to address both of these shortcomings would be to include derivatives of the mechanical signals in the forcing function (eq. 4.1). RA neurons would respond strongly to derivatives, and responses during ON and OFF periods would have opposite signs. Another improvement could involve adding the effects of the depth of the mechanoreceptor within the follicle to account for the deformation profile (Whiteley et al. 2015). The modeling approach of the present work is most similar to that of Dong et al. (Dong et al. 2013), which predicted the rate and timing of afferent responses

in primate glabrous skin based on combinations of stimulus kinematics. Both studies find that many response features can be predicted based on simple combinations of stimulus parameters.

4.3.4. The vibrissal system offers unique advantages for the study of mechanoreceptor responses

The results shown here underscore that responses of primary afferents depend on both sensor morphology and intrinsic mechanoreceptor properties. To tease apart the relative contributions of these factors the vibrissal system offers some unique advantages compared to the skin.

Direct stimulation or stretching of the skin is complicated by issues of viscoelasticity, nonlinear deformation, sweat, friction and hysteresis. Models of primary afferent responses in the skin have often required hundreds of parameters (Kim et al. 2010; Lesniak et al. 2014; Sripati et al. 2006).

In contrast, the 3D geometry of the vibrissa can be completely quantified and forces and moments can be computed at its base. Although our understanding of internal follicle mechanics is limited (Mitchinson et al. 2004; Whiteley et al. 2015), the vibrissa itself can be thought of as a tool for applying a highly repeatable stimulus to a mechanoreceptor. By applying the stimulation at different distances along the vibrissa length, the effects of applying a particular force can be decoupled from the effects of applying a particular displacement. Furthermore, by changing the intrinsic curvature of the vibrissa (Fig. 4.10) stimulus parameters can be varied in a systematic and repeatable manner.

Thus the simplicity of the vibrissal sensor, combined with robust physiological and morphological data, offers the ability to examine how each mechanoreceptor type acts differently to decompose tactile input. Given the homology of receptor types between vibrissa and hand, we anticipate that complementary experiments in these two systems will progressively help us “break the code” of the tactile periphery.

Author Contributions

T.F. designed the experiments; T.F. performed the experiments; T.F., S.E., D.H., K.S., and T.K. contributed to analysis of experimental data; N.M. and K.M. contributed to data acquisition of 3D electron microscopy. A.E.T.Y. and M.J.Z.H. designed and developed the simulations and A.E.T.Y. performed the mechanical modeling and simulations. A.E.T.Y. and M.J.Z.H. analyzed simulation results. T.F., A.E.T.Y., and M.J.Z.H. wrote the manuscript.

Acknowledgments

We thank Hayley M. Belli for writing the ODE solver for the SMD model. We thank John W. Rudnicki and Sara A. Solla for helpful discussions. We are also grateful to Keiko Okamoto-Furuta and Haruyasu Kohda (Division of Electron Microscopic Study, Center for Anatomical Studies, Graduate School of Medicine, Kyoto University) for technical assistance in electron microscopy. This work was supported by JSPS KAKENHI (Grant Number: 23135519, 24500409, and 15H04266) to TF, the Collaborative Study Program of NIPS to TF and NSF CAREER IOS-0846088, NSF EFRI-BSBA-0938007, and NIH R01-NS093585 to MJZH.

Supplemental Figures

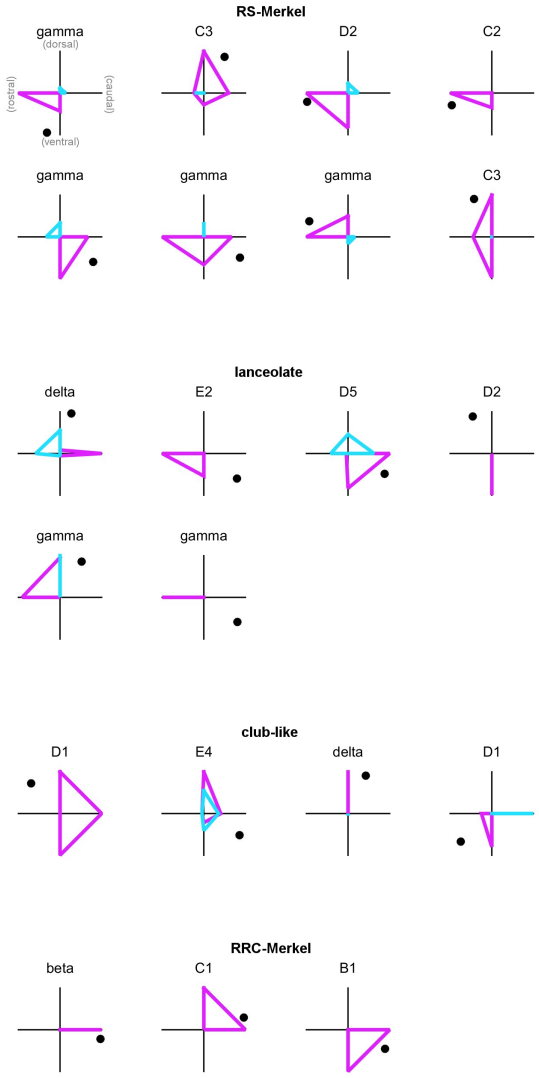

Figure 4.11. Angular tuning curves for the 21 primary afferents recorded in the present study are shown as "radar plots"

(Lichtenstein et al., 1990; Rutlin et al. 2014). The four directions of whisker displacement (rostral, ventral, caudal, and dorsal) are indicated in the schematic in the top left. In each subplot the black filled circle indicates the position of the nerve endings. The plotting convention for ON and OFF responses follows that of Lichtenstein et al., 1990. Pink polar plots indicate the magnitude of the ON response (window width: 10 ms from onset), and cyan polar plots indicate the magnitude of the OFF response (window width: 10 ms from offset). All responses shown in each subplot were normalized by the magnitude of the maximum response for that axon.

4.4. SUPPLEMENTAL EXPERIMENTAL PROCEDURES

4.4.1. Data analysis

Spike events elicited by vibrissa deflection were collected in peristimulus time histograms (PSTHs) of 20 responses with 1 ms bin width. Response magnitude was estimated as the mean number of spikes per stimulus within a time window of 10 ms after stimulus onset. We defined response onset as the first bin (poststimulus) displaying counts that significantly exceeded (99.99% confidence interval) spontaneous activity levels estimated over a prestimulus time window of 100 ms, or as the first two consecutive bins displaying significantly larger counts (99% confidence interval) than the spontaneous activity levels. Data were analyzed with IgorPro (WaveMetrics, Inc, Lake Oswego, OR) and Excel (Microsoft, Redmond, WA) software. Results are reported as mean ± SD.

Because RS-Merkel cells are slowly adapting it was sometimes challenging to distinguish between a true OFF response and a persistent response to the "hold" portion of the stimulus which continued into the OFF ramp. Some of these spikes happen to overlap with the OFF window. To distinguish persistent ON responses from OFF responses, the following procedure was used.

For each stimulus direction we performed a running average of the spike train (window size = 15 ms) over the entire duration of the ramp-and-hold stimulus to obtain the spike rate. We then averaged the spike rate in the 10 ms window immediately before the OFF ramp, and in the 10 ms window during the OFF ramp. The difference between the averages in the two windows was compared with a threshold, set to 5% of the maximum of the running average. If the difference was positive and smaller than the threshold, the response was counted as a persistent ON response and removed as an OFF response. This procedure eliminated a total of 14 OFF responses that were actually persistent ON responses. Results were identical regardless of whether the running average was computed over a 5, 10, or 15 ms window size.

4.4.2. Simulating the piezoelectric displacement of the vibrissa

To simulate vibrissa mechanics during physiological experiments we oriented an anatomical model of the rat head and vibrissa array (Towal et al., 2011) so that bregma and lambda were in the horizontal plane. In experiments the vibrissae were trimmed to 5 mm, so in simulation the vibrissa had a length between 4.9692 and 5.1020 mm to account for the vibrissas slip on the piezoelectric stimulator as well as the discretization of the vibrissa into nodes.

Piezo deflection of each vibrissa was simulated by rotating each vibrissa about its base-point by 5°. Vibrissae were displaced in the same four directions as in the experiments, i.e., rostral, caudal, dorsal, and ventral. Figure S8A depicts the trimmed gamma and D5 vibrissae from different point of view and their simulated displacements in all four directions.

We next computed the mechanical signals generated by these piezo displacements. Although piezo stimulation displaces the vibrissa in head-centered coordinates, the mechanical effect of these displacements must be computed in vibrissa-centered coordinates (Hartmann, 2015, Huet and Hartmann, 2016, Huet et al., 2015). As shown in Fig. 4.12, vibrissa-centered coordinates depend on the geometry of each individual vibrissa, with the origin placed at the vibrissa base. The x-y plane is defined as the plane in which the proximal $\sim 60\%$ of the vibrissa lies (Huet and Hartmann, 2016, Huet et al., 2015, Towal et al., 2011). The x-axis is parallel to the vibrissas length near its base, with positive pointing away from the vibrissa base. The y-axis is perpendicular to the x-axis, with positive pointing towards the vibrissa tip.

Using a 3D quasi-static model for vibrissa bending (Huet and Hartmann, 2016, Huet et al., 2015), we computed all six components of moment and force at the vibrissa base due to the piezo deflection. Details of the model have been described previously (Huet and Hartmann, 2016, Huet et al., 2015), but briefly, vibrissae are divided into nodes (100 in the present study), and the two bending moments My and Mz for each segment are calculated based on curvature and Youngs modulus.

The twisting moment of each segment (M_X) is derived from the torsional constant and Poissons ratio. With all three moments calculated, the three components of the force normal to the vibrissa can be calculated at the contact point location.

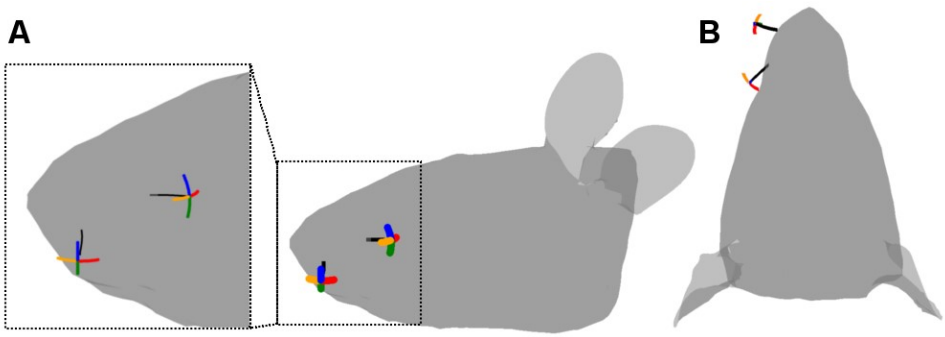

Figure 4.12. Simulation of piezoelectric displacement of the vibrissa
(A) The simulation of piezoelectric displacement in the rostral, caudal, dorsal, and ventral directions. The inset shows an expanded view of the video frame. **(B)** A rotated view of the simulated rats head to show trimmed vibrissae gamma and D5 from different points of view.

After mechanical signals were computed in vibrissa-centered coordinates the direction of the bending moment was adjusted to be relative to the physiologically-identified mechanoreceptor location to match with experimental data.

Fig. 4.6B shows that the magnitude of the bending moment ($M_B = \sqrt{M_Y^2 + M_Z^2}$) is nearly constant for all deflection directions of all 31 vibrissae. In contrast, Fig. 4.6C reveals that the direction of bending moment ($M_D = \arctan M_Z M_Y$) varies strongly with vibrissa identity because the deflection direction interacts with the vibrissas intrinsic geometry. The intuition here is that M_D expresses the mapping between the direction in which the vibrissa is displaced in the laboratory frame (as pushed by the piezo) and the direction in which the vibrissa is displaced in vibrissa-centered coordinates, as will be experienced by mechanoreceptors in the follicle. Notice that M_D is relatively constant in the dorsal or ventral directions (green and blue curves), but varies considerably in either rostral or caudal directions (yellow and red). The reason is that all vibrissae are oriented slightly concave ventral, but vary a great deal in the degree to which they curve concave forwards (Towal et al., 2011). High variability in M_D plays a key role in mechanoreceptor response (Fig. 4.13).

The magnitudes of F_X and M_X also vary greatly between vibrissae, as seen in Fig. 4.6D,E. More importantly, even for a single vibrissa, the magnitudes of F_X and M_X vary with deflection direction, as do the slopes of their onsets and offsets. Notice that while the M_B and M_X curves are completely linear, the

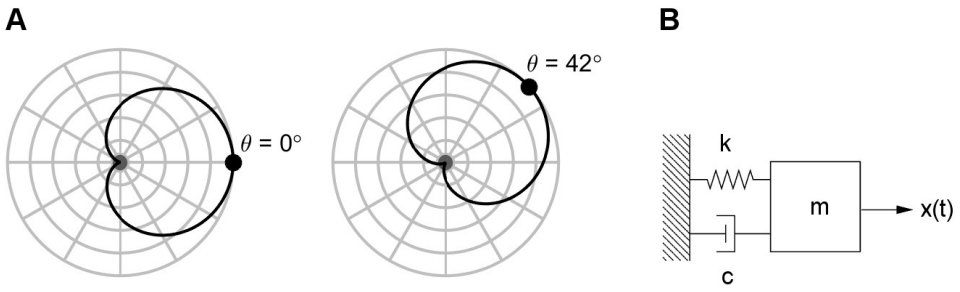

Figure 4.13. Models of mechanoreceptors
(A) Model that describes the angular tuning of the response magnitude to bending moment. Two examples are shown. In both examples, the gray dot in the center of the polar plot indicates the vibrissa, emerging out of the page. The black dot indicates the mechanoreceptor location, either at 0° (left panel) or 42° (right panel). The black curve in each panel illustrates how response magnitude (μ) varies as the vibrissa is pushed in different directions relative to the mechanoreceptor. **(B)** Spring-mass-damper model of the mechanoreceptor. The mass is allowed to move in only one dimension, and is connected to its surroundings by a spring and damper in parallel.

F_X signal often has small "bumps" near stimulation onset and offset, caused by significant nonlinearity in the F_X signal. The variability in the signals M_D, F_X, and M_X is entirely due to the differences in each vibrissas angle of emergence and intrinsic curvature, and indicates that responses of different magnitude and latency could be induced if mechanoreceptors were differentially sensitive to different combinations of the three signal magnitudes, M_B, F_X, and M_X.

4.4.3. Mechanoreceptor models

4.4.3.1. Accounting for the angular location of mechanoreceptors. One of the primary determinates of mechanoreceptor output will be its circumferential location within the follicle (c.f., Fig. 4.3E,F). To model this sensitivity, we implemented a cosine tuning function consistent with the angular tuning observed in previous studies of ganglion neurons (Jones et al., 2004, Lichtenstein et al., 1990). Fig. 4.13A illustrates an example of this angular tuning. The vibrissa points out of the page with its base at the center of the plot (black dot). The black curve represents the relative magnitude (μ) of the response as the vibrissa is pushed in different angular directions. In the example in the left panel, the mechanoreceptor lies at 0°, so the magnitude of the response is greatest in that direction. The magnitude of the response decreases with the cosine of the angle until the response is zero at 180°. In the example in the right

panel, the mechanoreceptor lies at 42° (chosen arbitrarily), so the magnitude of the response is greatest when the vibrissa is pushed to 42° and smallest when pushed to 222°.

The varying magnitude of response to bending moment can be mathematically expressed as:

$$\mu = \frac{1 + \cos\left(\theta_{push} - \theta_{receptor}\right)}{2} \tag{4.3}$$

where θ_{push} is the angle in which the vibrissa is pushed and $\theta_{receptor}$ is the angular location of the mechanoreceptor within the follicle. Note that μ is exactly 1 when the vibrissa is pushed in the same direction as the mechanoreceptor, exactly zero when it is pushed opposite to the mechanoreceptor, and exactly $\frac{1}{2}$ when pushed at 90° relative to the mechanoreceptor.

4.4.3.2. Optimizing simulated response magnitudes (finding the weights for Eq. 4.1. Each mechanoreceptor was modeled as a single degree-of-freedom spring-mass-damper (SMD) system, as schematized in Fig. 4.13B and expressed in Eq. 4.2. We hypothesized that mechanoreceptor responses could be predicted based on the SMD models response to different linear, weighted combinations of forces and moments (Eq. 4.1).

The first step in modeling was thus to efficiently determine the optimal combination of weights to be used in equation 1. To do this, we performed a multivariable linear regression using the function glmfit in Matlab^{TM}. The inputs to glmfit were determined as follows.

First, μ, F_X, and M_X were all normalized between -1 and 1. The weights are found based on these normalized values so that they reflect the degree to which each mechanical signal contributes to the solution.

Next, because M_X and μ vary monotonically with deflection angle (Fig. 4.6), the maximum value for these signals will always occur at the end of the ON ramp (and, by symmetry, at the start of the OFF ramp). Therefore the single value at this point was used as the input signal to the multivariable regression.

In contrast to M_X and μ, however, F_X does not always vary monotonically with deflection angle (Fig. 4.6D). Simply taking the value at the end of the ON ramp will not necessarily reflect the variations

in magnitude over the entire ramp. Therefore, we performed the multivariable regression for each of the 100 points of the ON ramp to find the optimal weight.

Thus, with one value for μ, one value for M_X, and 100 values for F_X, there were 100 candidate sets of $[\mu, M_X, F_X]$ predictors over which to optimize the weights for each afferent.

The Matlab^{TM}function glmfit evaluated all 100 candidate sets to find weights for each of the set of predictor variables. In each iteration, the input to the GLM model was a 4 by 3 array of predictors (four directions, three mechanical signals) and the output was a 4 by 1 response (one magnitude in each of the four directions). The constant term in glmfit was turned off. Out of the 100 solutions, only one set of weights was selected to carry over as input to the SMD dynamic model. This selection process involved four steps.

The predictor variables, $[\mu, M_X, F_X]$ were first multiplied by the optimal weights, resulting in four curves, one for each deflection direction. Next, the simulation magnitude in each of the four directions was determined from the peak of each of the four curves. We then compared the four simulation magnitudes with the experimentally-measured sum of spikes over the 10-ms ON window in that direction. Finally, for each solution, the sum of the squared errors between simulation and experiment was computed, and the solution with the smallest error was selected.

Note that for most axons of the present study the spikes of interest are only those that occur during the ON ramp. In cases where there are no spikes during onset, the spikes of interest are then those that occur during the OFF ramp. For OFF responses, the sum of spikes was designated as negative for the purposes of modeling. The motivation for the negative sign was to ensure a bounce back (overshoot) above zero during the OFF response when the dynamic response was simulated (see next section).

4.4.3.3. Optimizing simulated response latencies (finding m, c, k, for Eq. 4.2). The optimal static ramp f in Eq. 1 serves as the input forcing function to the spring-mass-damper model of mechanoreceptors, in Eq. 2.

The dynamic response of a mechanoreceptor to the input function f is a trajectory of positions, x. The position trajectory x is a 41000 array, corresponding to 4 pushing directions and 1,000 time steps

(0.1ms resolution), and can be computed for any given choice of mass (m), damping coefficient (c) and spring constant (k).

Because the spring constant k is the proportionality constant between f and x, it will simply scale the response magnitude for all four directions within each axon by the same factor for a given m and c. In other words, the absolute magnitude of k will not alter the relative response magnitudes across the four pushing directions for each individual axon.

Therefore, assigning a unit spring constant $k = 1\frac{N}{m}$ simplified the dynamic model without loss of generality. The dynamic properties that remain to be found are the mass m, which determines the natural frequency of oscillation, and the damping coefficient c, which describes how the oscillation amplitude decays with time. Mass and damping coefficients were optimized over receptor type.

In addition to m and c, a response threshold was imposed on top of the dynamic trajectories to represent the neurophysiological phenomenon of a firing threshold. To find a single response threshold optimized for all four stimulus directions for each primary afferent, the search domain was defined between the minimum and maximum dynamic response divided into 100 increments.

The search for the optimal m, c and threshold was performed in a brute-force nested loop. For each combination of m, c, and threshold, we evaluated the fitness between the simulated dynamic oscillation trajectory and the experimental spike histogram. Thus for each iteration of the nested loop, a set of four dynamic trajectories were calculated for a given m and c; all four trajectories were placed under a threshold to determine a simulated latency for comparison with experimental latencies. Following this comprehensive search, the set of values for m, c, and threshold that minimized the error between simulation and experiment was selected as optimal.

CHAPTER 5

Contact-resistive sensing of touch and airflow using a rat whisker

This chapter has been submitted to the 7th IEEE RAS/EMBS International Conference on Biomedical Robotics as "Yang AET, Hartmann MJZ, and Bergbreiter S (in review) Contact-Resistive Sensing of Touch and Airflow Using A Rat Whisker."

Rats rely heavily on tactile information from their whiskers to acquire information about their surroundings. Whiskers have no sensors along their lengths. Instead, all mechanical information is transmitted via the receptors at the base of whiskers. The present study introduces a micro-sensor developed specifically to imitate the sensing of biological rat whiskers. The sensor responds to bending moments resulting from touch and/or airflow in two axes. The sensor was designed based on analytical models from cantilever beam theory. These models were validated by Finite-Element Analysis. Sensors were then fabricated using micro-milled molds and integrated into an Arduino-based circuit for simple signal acquisition. The present work investigates the engineering aspect of an excellent bio-inspired sensing system. The investigation provides better understanding of the principles behind the first few steps in the neural pathways of the rat's sense of touch. These principles will advance the knowledge of the neural pathway of humans' sense of touch. The sensor also has human-assistive potential.

5.1. Introduction

The rat vibrissal (whisker) array system (Fig. 5.1A) is a common model for the neuroscience of touch. Behaviorally, rats use their whiskers for tactile exploration similar to the way in which humans use their hands. Physiologically, the neural pathways are in many ways analogous between whiskers and hands. A major distinction between the two systems is that mechanically, whiskers are simpler than

hands. Viewing whiskers as cantilever beams with sensors located only at the base in theory allows us to quantify the complete mechanical input to the system during active sensing behaviors more easily than for hands.

However, researchers find it infeasible to install a sensor to a rat's face to directly measure mechanics without interfering with whisker mechanics or the large number of receptors under the skin. Up to this day, research in the field typically rely on image processing and numerical modeling to simulate the mechanics at the whisker base (Huet et al., 2015). Simulations are typically limited to quasi-static motions. The whisker dynamics during free-air whisking and airflow tracking (Yu et al., 2016a) are highly challenging to simulate due to the whisker's extreme geometric aspect ratio. Therefore, it is important to the field of neuroscience to have an engineered sensor for biological whiskers. The sensor can contribute to the validation of simulated quasi-statics and the knowledge of whisking dynamics.

The rat whisker's interaction with environment takes place anywhere along the whisker's length. Nevertheless, all the mechanical signals are transmitted via the follicle exclusively located at the base (Ebara et al., 2002). Previous studies have shown the lateral bending moments are sufficient in pseudo-2D (Yang and Hartmann, 2016) and crucial in 3D (Huet et al., 2017) to detect contact location. The taper (Hires et al., 2016) and elastic (Quist et al, 2011) properties of whiskers play crucial roles in the efficiency of the mechanical information transfer process. In other words, biological whiskers have advantageous properties that are missing or difficult to control in artificial materials for robotic sensors. This study presents a sensor particularly tailored for biological whiskers. The flexible, lightweight, and bio-compatible nature of the sensor also makes it a good candidate for wearable assistive devices such as health-monitoring strain sensor (Harada et al., 2014) and flexible joysticks.

A version of the sensor was first mentioned in a previous publication (Charalambides and Bergbreiter, 2017) as a potential application The fabrication process in the present work is derived from the fabrication methods described in that paper. The primary contributions of the present work are an informed geometric design based on both analytical and Finite Element Analysis (FEA) models, new material choices for fabrication, and new experimental results from touch and airflow sensing.

5.2. Methods

The basic sensor design is shown in Fig. 5.1B. A whisker is to be inserted in a central pillar made from a conductive elastomer. As the whisker is bent, the pillar contacts surrounding pads, forming conduction between the pillar and those pads. To obtain a usable signal from this sensor, both the geometry and material choices are important, as described below.

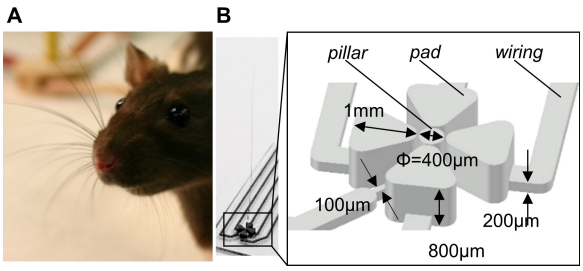

Figure 5.1. The inspiration and design of the sensor
(A) A photograph of a rat and its whiskers. **(B)** A photograph of the sensor and a close-up schematic of the sensing region. The dimensions and names of features within the sensing region are labeled.

5.2.1. Materials preparation

Two composite materials were used in the present study:

- *Material I*: consistent with preliminary work (Charalambides and Bergbreiter, 2017), *Material I* used polydimethylsiloxane (PDMS) (Sylgard 184, Dow Corning) as the base dielectric layer and carbon nano-tubes (CNT) (Multi Walled Carbon Nanotubes, SKU 030103, outer diameter: 10-20 nm; length: 10-30 μm) mixed with PDMS as the material for conductive features. Materials were mixed by a speed mixer (DAC 150, FlackTek Inc.) at 2000 rpm for 90 s.
- *Material II*: Other studies (Chen et al, 2017; Li et al., 2017) have shown that creating a porous structure in the CNT-PDMS mixture before curing increases sensitivity to strains. We followed the approach of (Chen et al., 2017) to determine if adding sugar lowers the effective modulus of the conductive material and increase its surface conductivity. Powdered sugar was selected for its grain size (<10 μm), suitable for homogeneous distribution. To avoid added materials from store-bought powdered sugar, cane sugar was ground into powder by a mortar and pestle.

5.2.2. Mechanical simulation on sensor deformation

To tailor the sensor for contact-resisitve sensing, there are three important design features—one "pillar" to which the rat whisker is attached, some "pads" surrounding the pillar that come into contact with the deflected pillar when the whisker is displaced, and the gaps between the pillar and pads. The minimum width of the pillar is constrained by the tool diameter of the micro-mill. The height of the pillar needs to be sufficient to hold a typical whisker, with a length of $\sim$35 mm and a diameter of $\sim$150 μm. The gap widths are determined by the repeatability of the micro-mill. The geometry of the pads is less constrained, but still must be larger than the smallest tool diameter used.

Here, we carry out theoretical derivation using beam bending theory and computational simulation using FEA to find advantageous designs for the pads. A design is considered advantageous if it results in greater reaction force between the contacting features. In the computational simulation performed in Abaqus, the two raw materials—PDMS and CNT-PDMS have a Young's modulus of 1.5 MPa and a Poissons ratio of 0.49 (Charalambides and Bergbreiter, 2015; Johnston et al., 2014).

5.2.3. Fabrication

The fabrication procedure is consistent with the work described in (Charalambides and Bergbreiter, 2017) with some deviations. A 0.25" thick acrylic sheet was milled using a bench-top micro-mill (Roland MDX-540SA) with two end mills: 406 μm and 100 μm diameters. The milled features were then filled with one of the conductive materials described above. An automatic hydraulic heated laboratory press (model 3895, Carver, Inc.) was used to apply a normal force equivalent a weight of 500 kgf (4905N) to ensure complete refill of the material. Excessive material was next removed using a squeegee that is typically used for T-shirt graphic printing. The acrylic mold along with the refilled conductive material were cured in a convection oven (Oster TSSTTV0001) at 200°F for 30 minutes (including preheating time). Once the acrylic cooled down to room temperature, a dielectric PDMS layer was poured on top of the acrylic and conductive material. The mold with CNT-PDMS and PDMS was then placed into a vacuum chamber to vacuum at 0.08 atm (-27.5 $inHg$) for 30 minutes. Finally, the whole workpiece was cured for a second time in the same convection oven at 200°F for 60 minutes (including preheating

time). After curing, the sensor was removed from the oven to cool for at least one hour before the sensing features along with the PDMS layer are peeled off manually.

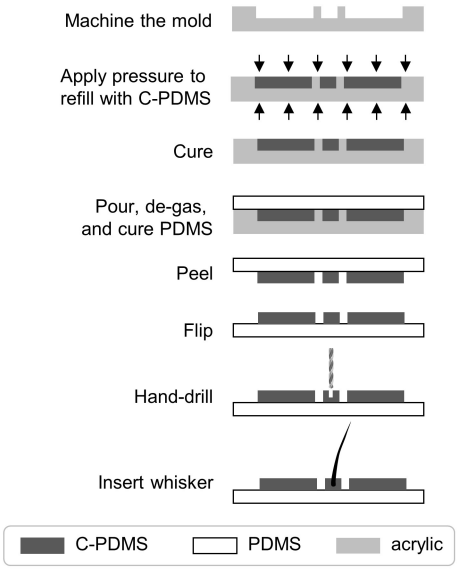

Figure 5.2. The fabrication flow chart of the sensor.
The number of procedures remains the same for any number of sensors in the array.

5.2.4. Whisker attachment

A real rat whisker was attached to the sensor using a clearance fit. The whisker was cut off with scissors from a rat. A micro drill-bit of diameter 150 microns (High-speed steel micro-size drill bit 0.0059" size, MacMaster-Carr) was held using a pair of tweezers and inserted at the center of the pillar along its height. The drill-bit was detached from the sensor when the hand-drilling was completed. Similarly, the whisker was held by the tweezers and inserted into the pillar within the drilled hole.

The whisker remained fixed in the sensor because the diameter of the whisker is slightly larger than that of the drill-bit. Glues were avoided in this process as it would have caused an insulation layer at the surface of the conductive material.

5.2.5. Voltage divider for contact resistive sensing

The sensor transduction is based on contact resistive sensing, which simplifies the electronic interface required to pick up signals when features come into contact. The pillar is connected to a $5V$ supply (V_0), and each pad is a voltage output from the sensor (V_{out}). The resistance to be measured between the pillar and each pad is denoted as R_1. In addition, a reference resistor, R_2, is connected between voltage output (V_{out}) and ground. The voltage output from each pad of the sensor therefore has the following relationship with the supply voltage and resistances:

$$V_{out} = \frac{R_2}{R_1 + R_2} V_0 \tag{5.1}$$

When the sensor is at rest, because the pillar and a pad are not in contact, the resistance (R_1) is ∞, maintaining the output voltage V_{out} at 0. As soon as contact occurs between the pillar and a pad, the resistance (R_1) becomes a finite value, and a non-zero V_{out} will then be recorded. The reference resistor (R_2) is selected to be similar to that of the features on the sensor (R_1), typically at the scale of $\sim$10 $k\Omega$. The higher the reference resistance, the higher the sensitivity and the noise. To record these voltage outputs, each V_{out} is connected to an ADC channel on an Arduino UNO connected to a computer through USB.

5.3. Results

5.3.1. Geometry and contact quality

We applied beam theory to determine what kind of sensor geometry provides the largest reaction forces between parts of the sensor when the whisker is bent. A schematic of one sensing direction of the sensor is shown in Fig. 5.3. In the left panel, two cantilever beams represent the center pillar and the surrounding pad spaced by a gap distance d. The two beams have area moments of inertia of I_1 and I_2, respectively. Both beams have the same length, L, and Young's modulus, E. An external force P is applied at the end of the first beam. The first beam then deflects and touches the second beam, subsequently causing the second beam to also deflect.

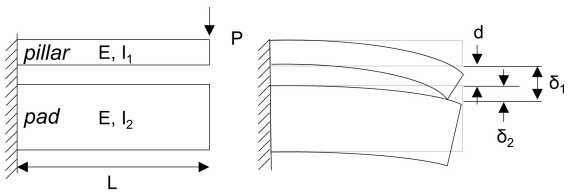

Figure 5.3. An illustration accompanying beam theory derivation
A rotated view of the pillar and a pad, modeled as two cantilever beams of length L spaced by a gap of size d, with moments of inertia I_1, I_2. The initial condition before a load P is applied is illustrated on the left. The deflected condition under the applied load is shown on the right. The tips of the two beams deflect by δ_1 and δ_2, respectively.

Under the deflected condition, the reaction force to be maximized in this derivation, R, takes place of equal magnitude and in opposite directions to the two beams. As a result, the two beams experience total forces of $(P - R)$ and R, respectively. From established beam bending equations (Hibbeler, 2014) the tip deflections of cantilever beams, δ_1 and δ_2, have the following relationship with P, R, L, E, and I:

$$\delta_1 = \frac{(P-R)L^3}{3EI_1}, \quad \delta_2 = \frac{RL^3}{3EI_2} \tag{5.2}$$

To satisfy the condition of compatibility, as illustrated in the right panel of Fig. 5.3, the relationship between the two tip deflections, δ_1 and δ_2, and the spacing between two beams can be described as:

$$\delta_1 = \delta_2 + d \tag{5.3}$$

Substituting (5.2) into (5.3), the compatibility equation can be rewritten as:

$$\frac{(P-R)}{3EI_1} = \frac{R}{3EI_2} + \frac{d}{L^3} \tag{5.4}$$

The last term in equation (5.4) is infinitesimal compared to the other terms because in our design, the spacing between features d is much less than the length of beam L ($d << L$).

The equation can thus be simplified as:

$$I_2(P-R) = I_1 R \tag{5.5}$$

Finally, after rearranging equation (5.5), the force occurring between the center pillar with a mass moment of inertia of I_1 and a surrounding feature with a mass moment of inertia of I_2 is proportional to the external input force P by the following equation:

$$R = \frac{I_2}{I_1 + I_2} F \tag{5.6}$$

The equation suggests that with a fixed geometry of the pillar (constant I_1), the greater the moment of inertia of the pad I_2 is, the greater the reaction force will be between the pillar and the pad when the pillar is deflected by a set amount of force. Therefore, a wedge geometry was chosen over a cylinder given its much greater moment of inertia. The width of the wedge increases radially from the pillar, which adds stability and prevents buckling.

In addition, an Abaqus simulation introduced in section 5.2.2 shows results that validate the theoretical derivation. In the simulation, the top half of one side of the drilled hole in the center pillar undergoes a pressure, driving the pillar towards the pad.

When constrained by the same pressure, $10kPa$, the resultant elemental displacements are shown in the middle row of Fig. 5.4. The pillar displaces towards the cylinder pad (left) more than towards the wedge (right). Besides, the cylindrical pad displaces slightly when contacted by the pillar, while the wedge does not. Smaller displacement means a greater portion of the mechanical work ended up as strain energy.

When constrained by the same displacement control, 40 μm, the resultant von Mises stresses, shown in the bottom row of Fig. 5.4, demonstrate that the wedge design leads to greater contact stress between features, in line with the analytical derivation at the beginning of this section.

5.3.2. Tactile signals and bending moment conversion

Two versions of sensors with three and four pads, respectively, were fabricated using *Material I*. Each version has its advantages and disadvantages.

The sensor with three pads is only applicable in scenarios where the source of stimuli is constrained to a certain range. Nonetheless, the lack of a fourth pad frees up space for wiring of the pillar. The

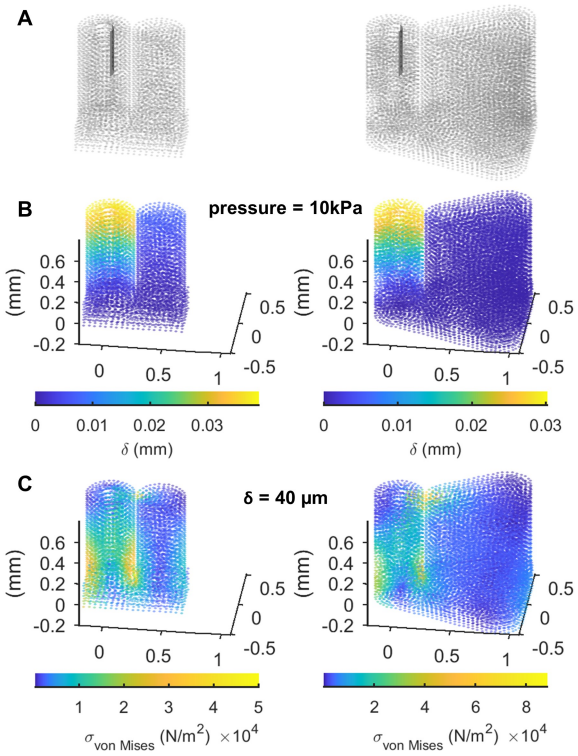

Figure 5.4. FEM simulation results explain the choice of sensor geometry
(A) A pressure is applied to the pillar on the top half of a curved surface within the hole for whisker, as the shaded area in the illustration. **(B)** FEA simulations in Abaqus showed the overall displacements magnitude (δ) under the same pressure for two geometric designs of pads– cylinder (left) and wedge (right). **(C)** Abaqus output the von Mises stress under the same displacement control.

wiring can thus be as wide as the pillar diameter, which can be machined using the same tool used for the rest of the sensor.

The sensor with four pad covers the full 360° range within the surface normal to the whisker. The drawback is that it requires an undesirable tool change. Tool change is necessary when the wiring space for the pillar is taken up by the pads, constrained by a 400-μm tool diameter (ϕ_{tool}) and a 30 μm gap (D_{gap}) between pads. In the four-pad design, between two adjacent pads that are angularly spaced out by 90°, the maximum spacing between two pads remained for pillar wiring (D_{wire}) calculated by equation (5.7) is 208 μm, which only fits the 100-μm end-mill, not the 400-μm.

$$D_{wire} = (\phi_{tool} + D_{gap})/\sin 45^\circ - \phi_{tool} \tag{5.7}$$

Raw voltage signals (V_{out}) recorded from the two versions (with different numbers of pads) are plotted in Fig. 5.5. Data were sampled from each pad at a rate of 125 Hz. The recorded voltages were less than the supply voltage, $5V$, in all cases, suggesting that none of the signals were saturated. The peak voltages within each plateau occurred in the direction of bending as expected.

During low responses, signals are not absolutely zero due to electronic noise. On the other hand, within each plateau of non-zero responses, signals oscillates at a frequency that is visually distinct from electronic noise. The oscillation within each plateau is primarily due to perturbation within the manually-delivered stimulus. It is also worth noting that below the maximum trace within each plateau, a secondary signal took place (e.g. orange under blue and blue under yellow traces). The primary and secondary signals are in-phase, inferring that the secondary signals are likely the result of slight deviation in the direction of stimuli from the principle axes, .

The raw output voltages from the sensor can be converted by the following equations into voltages corresponding to bending moment magnitude (M_B) (5.8) and direction (M_D) (5.9):

$$M_B = \sqrt{\sum_{i=1}^{N} V_{out,i}^2} \tag{5.8}$$

$$M_D = \arctan \frac{\sum_{i=1}^{N} V_{out,i} \sin \theta_i}{\sum_{n=1}^{4} V_{out,i} \cos \theta_i} \tag{5.9}$$

where N is the number of wedges, and $\theta_i = [90, 180, 270, 0]^\circ$.

The value of M_B, converted from voltages, is positively correlated with the bending moment. A calibration curve is needed to quantify the accurate scale. In the present work, M_B inherits the same unit as voltage. Results of converted mechanical signals are also shown in Fig. 5.5. On the other hand,

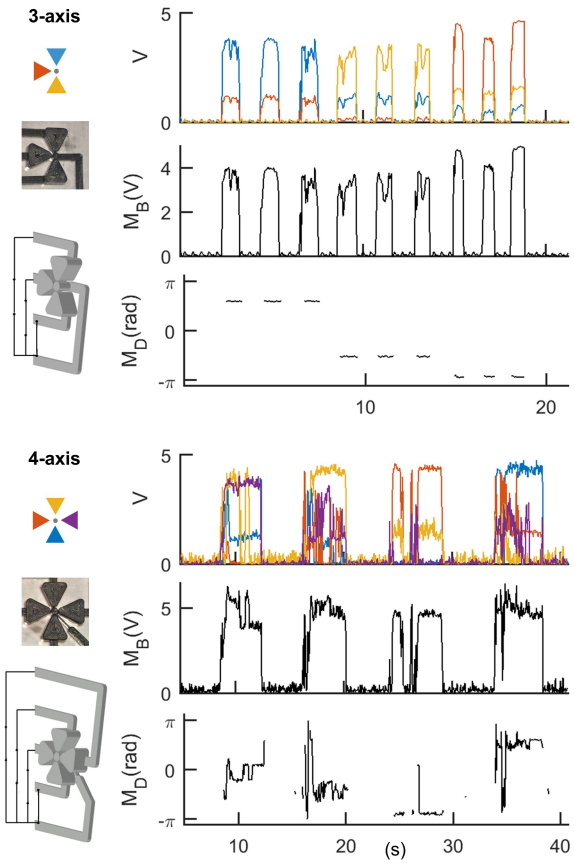

Figure 5.5. The three- and four-axis versions of the sensors were fabricated and tested
The whisker was deflected towards one direction at a time. Each half of the figure includes a legend labeling the pad each voltage port is connected to, a top-down stereoscope image, a schematic showing measured resistances, raw voltage signals, and converted bending moment magnitude M_B and direction M_D. Only M_D during non-zero M_B are shown.

M_D is directly related to the actual bending direction in *deg*. Results after conversion are presented as the black traces in Fig. 5.5.

The three-pad results of M_B align with the maximum voltage at each time point, suggesting that the magnitude of secondary signals have a similar effect on all three directions. The resting voltages are also consistently at zero, indicating the absence of obvious hysteresis post-contact. The M_D data are clearly consistent within each triplet.

Likewise, converted mechanics for the four-pad sensor are shown also in Fig. 5.5. The four-pad sensor behaves in a similar manner as the three-pad sensor with regard to both M_B and M_D. However, the

four-pad data are much more noisy than the three-pad data. One cause of the noise is that the pillar's wiring is four times narrower than its diameter, making the pillar structurally less stable. Consequently, the pillar in four-pad sensor does not maintain or revert to resting position following bending as well as in the three-pad sensor does.

5.3.3. Response to airflow

In a separate series of experiments, we investigated the sensor's response to airflow. To better characterize possible dynamic oscillations, the sampling rate had been increased to $1039Hz$. The data in this section were acquired using a sensor fabricated with *material II*. Since the focus here is irrelevant to bending direction, only one pad was connected. The reference resistance on the voltage divider is 780 $k\Omega$.

The setup and results are shown in Fig. 5.6. Airflow were generated from an air valve on a conventional lab bench (not shown in the picture) flowing through a tubing with an inner diameter of 7.6 mm. The center of the cross-section of the tubing was fixed at a height of 22.5 mm from the base layer of the sensor, targeting a position approximately one quarter of the whisker length from the tip.

In the first trial, the sensor responded to airflow of a constant speed of 10.0 m/s. The airspeed was measured 7.5 cm from the tubing at 24.1 $°C$ with a hot wire anemometer by Omega Engineering Inc. The end of the tubing was moved from afar to be next to the whisker (at a distance of 30 mm from the whisker), held at the same position for about one minute, and then moved away. The blue trace in Fig 5.6B illustrates the velocity of air the whisker underwent. Signals from the sensor are shown in black in the same subplot. The voltage response remained constant throughout the whole duration and reverted back to zero timely with the departure of the air supply.

The second trial tested the sensor's response to airflow of varying speeds. Throughout this trial, the end of the tubing was constrained at a horizontal distance of 22 mm from the whisker. The airflow was manually operated to gradually go up from zero to a maximum velocity of approximately 10.0 m/s and then go back down to zero, as illustrated by the blue trace in Fig. 5.6C. Raw data from a single trial are depicted in the same subplot. The voltage response exhibits changes with the variation of airspeed, though not perfectly correlated. During the ramp-up phase (5-17s), the first non-zero voltages took place

after the first non-zero airspeed, implying a bending magnitude threshold for detection. The non-zero voltage went through a steep and noisy ramp up before more steadily increasing with airspeed. Similarly, during the ramp-down phase (22-34s), voltage started decreasing later than airspeed did. The signal then goes through a steep variation before steadily decreasing with airspeed. The sensor stopped responding when airspeed dropped below a certain value.

We further processed these data via Fast Fourier Transform (FFT) into a single-sided amplitude frequency spectrum. However, no obvious resonance has been observed, even though whiskers of similar sizes typically vibrate with a first-mode resonance within ($\sim$50-100 Hz) in airflow, as reported through imaging techniques in a previous study (Yu et al., 2016b). Possible reasons for the absence of resonance are discussed in section 5.4.

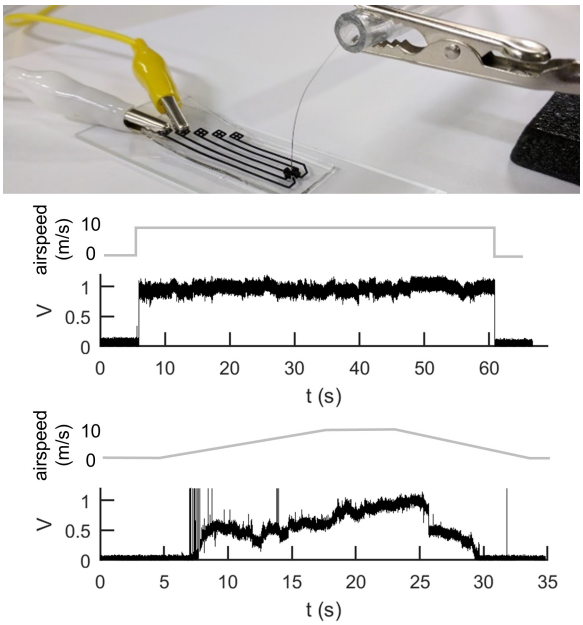

Figure 5.6. A single axis responds to an airflow of constant and varying airspeeds.
(A) A picture of the sensor, connecting wires, and the clamped air tubing. **(B)** The sensor's response to a constant airspeed. The blue trace illustrates when the source of airflow is near the whisker. **(C)** The sensor's voltage response to airflow in a close-up view between 0 and 1.2V.The blue trace illustrates the estimated airspeed based on manual control.

5.4. Discussions

Calibrations are ongoing to quantify the correlation between the normalized voltage in the M_B plots in Fig. 5.5 and the actual bending moment magnitudes. In addition, future work is needed to improve the current design and sensing regime:

- Exploration on different geometries is also worthwhile, since in the current design, the stress that occurs within the sensing material in response to whisker deflections are highly restrained to a small area and magnitude. More consistent control of the fabrication process is needed to achieve sufficient sensitivity for all sensing axes. So far airflow sensing has been conducted in only one axis.
- Alteration of the materials will potentially further improve the performance. Based on empirical observations, adding powered sugar, as done for *Material II* in section 5.2.1, appears to solve the problem of reduced conductivity for the top surface but not the sides. Nevertheless, the side surfaces of the tall parts of the sensor (the pillar and the pads) have much lower electrical sensitivity compared with the top. Such height is necessary to provide sufficient contact area for the whisker mechanics to transmit to the pillar. Possible explanations for different local sensitivities include the inhomogeneous distribution of materials within the composite due to gravity and applied pressure. Characterization of surface finish is needed to investigate and enhance the material behaviors.
- The sensor is expected to capture whisker vibration in airflow following a few modifications. First of all, the noise in the circuit will be reduced by replacing the breadboard and alligator clamps with printed circuit board and soldering. More importantly, the sensor currently has a limited range for magnitude variation. Bending has a minimum threshold for detection– it has to be sufficiently large to cause a pillar deflection greater than the size of the gap. Meanwhile, the signal has to be lower than a maximum before causing electrical signal saturation. A different transduction method will be more applicable to airflows at magnitudes close to the rat's natural environment. One example is capacitive sensing (Charalambides and Bergbreiter, 2015), as it

uses the range between the pillar's resting position and its initial contact with surrounding pads. The air will serve as the dielectric layer in this case, such that the pillar's range of motion is not impeded. Lastly, it is important to know that whisker's primary direction of vibration not identical but orthogonal to that of bending (Yu et al., 2016a), so recording airflow with all four pads would provide more comprehensive results.

5.5. Conclusions

The present study demonstrated a time- and cost-efficient approach to acquire bending mechanics of a biological whisker. The highly scalable, streamlined fabrication process is favorable for setting up a large number of sensors to investigate the interconnected mechanics among all whiskers in the array. The same sensor can also be adapted for any whisker- or hair-like structures at similar scales to advance the knowledge of other biological systems. Last but not least, the soft materials throughout the sensor allows mounting to uneven surfaces, such as 3D-printed animal faces for bio-mimic sensing robots and human skins for wearable assistive technologies.

Acknowledgment

We thank David Collinson for helpful discussions and Hee-Sup Shin for assistance with machining. We thank the Advanced Materials Laboratory at Northwestern University for use of the vacuum chamber and heated press. We thank the Center for Innovation in Global Health Technologies at Northwestern University for use of the FlackTek mixer.

CHAPTER 6

Summary and Future Outlooks

6.1. Summary

In Chapter 2, mechanical properties and weight distribution were quantified for individual whiskers, aiding in accurate dynamic simulations. Comparing bending due to a whiskers' weight with different hypotheses supported the idea that the existence of medulla in whiskers is structurally advantageous. Also, the dimensionless parameter associated with bending varies systematically across the array, even though the parameter associated with geometry does not.

In Chapters 3 and 4, simulated whisker mechanics in 3D was applied to two sorts of neuroscience experiments. In Chapter 3, simulation results provided an evidence that rats have mechanisms to obtain information about their surroundings based solely on quasi-static mechanical signals at a single whisker base in a "pseudo-2D" environment. Similar simulations also showed that the characteristic kinematics (roll and elevation) of whisking contributed to the uniqueness of these localization mappings. Moreover, a subset of the data supported the behavioral observation that rats are more capable of retaining localization capability with all but one column of whiskers trimmed than with all but one row of whiskers trimmed. In Chapter 4, the same mechanical model was employed to simulate the mechanics of whiskers when stimulated along four directions by piezoelectric manipulators. The results exhibited unintuitive variability in the mechanical responses to the seemingly identical stimuli. The variability was a result of geometry, angle of emergence, and angular tuning. The results also predicted neural responses to stimuli recorded from neurons associated with identified mechanoreceptors types at a success rate of 93%.

In Chapter 5, a robotic tactile sensor was built "from" and "for" neuroscience. Inspired by whisker base mechanics and how rats implement it to acquire spatial information, a sensor was designed and fabricated to extract bending signals from the base of a biological rat whisker. Preliminary data demonstrated

the efficacy of tactile and airflow signal magnitudes and directions. In addition to validating and quantifying mechanics in the biological system, the sensor has great potential for wearable, health-monitoring devices.

6.2. Future outlooks

6.2.1. Future work on mechanical properties

Future studies should implement these newly quantified properties for mechanosensory signals correlated with neural activities. The way in which geometry scales quasi-static bending is important to explore. In addition, quantifying whisker cuticle distribution will crucially improve the accuracy of material and dynamic properties and likely better explain the average density variation from whisker base to tip. Comparing the locations of cuticle thickness change point, medulla termination point, and the whisker's out-of-plane transition would provide insight into the whisker's unique geometry.

6.2.2. Future work on head-centered localization

Analyzing how rats combine the mechanical signals explored in Section 3.3.2 and an estimation of whisker position upon contact as a localization mechanism would be informative for understanding more about the proprioception. Indeed, open questions remain, such as how trigeminal ganglion neurons process localization information, how the mechanism differs between protraction and retraction, how rats determine heights (potentially using a third mechanical variable), and the effect of friction, etc. Finally, continued exploration of mappings with varying head pitches expanding on the results of simulations conducted here is recommended.

6.2.3. Future work on mechanoreceptor mechanics

Questions remain unsolved regarding mechanoreceptor's steady-state responses. The difference (asymmetry) (Section 4.2.5) between ON and OFF responses in each stimulation direction on each whisker is also challenging to explain. Incorporating the following features will potentially enable predictions of the steady-state and/or asymmetric responses. The features include but are not limited to– the dynamic

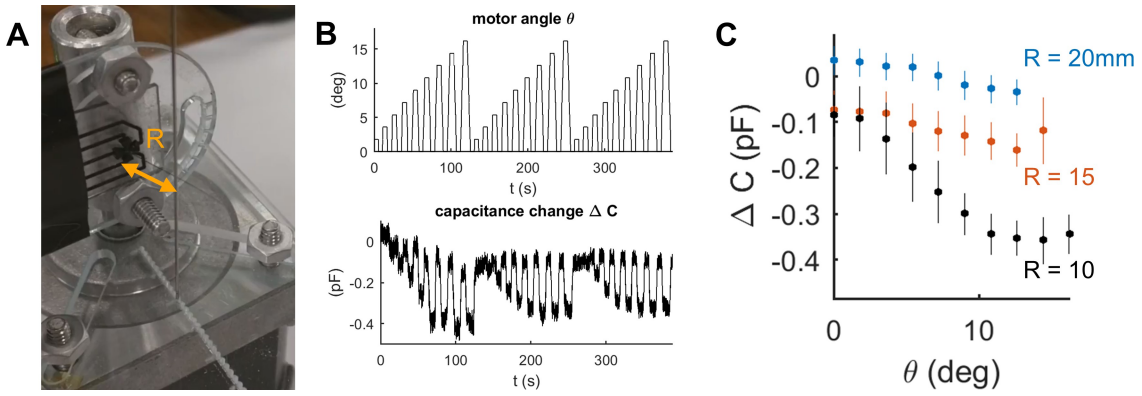

Figure 6.1. Preliminary data from capacitive sensing
(A) A whisker sensor is mounted on a stepper motor. As the motor shaft rotates, the whisker pushes against the peg orthogonally. The shortest distance between the peg and the base of whisker is denoted as R. **(B)** The variations motor angle *(top)* and capacitance change *(bottom)* with time throughout one continuous trial with three repetitions of increasing angles. **(C)** The average and standard deviation of the correlation between motor angle and capacitance change. Each color represents one radial distance of contact, R.

effects of collision and vibration, the geometries and longitudinal locations of mechanoreceptors, verified boundary condition of the whisker base inside the follicle, and consideration of whisker base translation relative to the follicle entrance, etc.

6.2.4. Future work on whisker sensor

As mentioned in Chapter 5, exploration of different geometric designs and materials have great potential for improving the sensitivity of the sensor in contact-resisitve mode. The noise from the circuitry could also be further reduced by consolidating the wiring. More importantly, capacitive sensing with the existing whisker sensor will have improved sensitivity and make a better candidate for airflow sensing. Work is in progress to implement capacitive sensing based on circuitry designed by Rishabh Agarwal from the University of Maryland, College Park. Preliminary data in Fig. 6.1 depict the correlation between whisker push angle, radial distance of contact, and capacitance change. Ultimately, installing an array of sensors on an artificial to-scale rat head will shed light on the inter-whisker effect of airflow across the array. Mounting whisker sensors onto geometries customized with animal facial features will enable quantification of airflow dynamics across the animal head.

Conclusion

Through the implementation of mechanical modeling, the complexity of a real-world biological system of rat whiskers was quantified and analyzed with great precision and accuracy. This work stresses the need for continued collective efforts and conversations at the unique intersection of various disciplines. Advancement in neuroscience and robotics is expedited by the understanding and application of mechanical principles. Neuroscience knowledge enables neural rehabilitations, and robotic technologies monitor health and provide assistive devices. Ultimately, advancement in these two fields both directly contribute to humans' health and can enhance overall welfare.

References

[1] Abraira, V.E., and Ginty, D.D. (2013). The sensory neurons of touch. Neuron 79, 618-639.

[2] Adineh, V.R., Liu, B., Rajan, R., Yan, W., and Fu, J. (2015). Multidimensional characterisation of biomechanical structures by combining Atomic Force Microscopy and Focused Ion Beam: A study of the rat whisker. Acta Biomaterialia 21, 132-141.

[3] Ahissar, E., and Knutsen, P.M. (2008). Object localization with whiskers. Biol Cybern 98, 449-458.

[4] Ahl, A.S. (1986). The role of vibrissae in behavior - a status review. Veterinary Research Communications 10, 245-268.

[5] Bagdasarian, K., Szwed, M., Knutsen, P.M., Deutsch, D., Derdikman, D., Pietr, M., Simony, E., and Ahissar, E. (2013). Pre-neuronal morphological processing of object location by individual whiskers. Nature Neuroscience 16, 622.

[6] Bautista, D.M., and Lumpkin, E.A. (2011). Perspectives on: information and coding in mammalian sensory physiology: probing mammalian touch transduction. Journal of General Physiology 138, 291-301.

[7] Belli, H.M., Yang, A.E.T., Bresee, C.S., and Hartmann, M.J.Z. (2017). Variations in vibrissal geometry across the rat mystacial pad: base diameter, medulla, and taper. Journal of Neurophysiology 117, 1807-1820.

[8] Berg, R.W., and Kleinfeld, D. (2003). Rhythmic whisking by rat: Retraction as well as protraction of the vibrissae is under active muscular control. Journal of Neurophysiology 89, 104-117.

[9] Bermejo, R., Vyas, A., and Zeigler, H.P. (2002). Topography of rodent whisking - I. Two-dimensional monitoring of whisker movements. . Somatosens Mot Res 19, 341-346.

[10] Birdwell, J.A., Solomon, J.H., Thajchayapong, M., Taylor, M.A., Cheely, M., Towal, R.B., Conradt, J., and Hartmann, M.J.Z. (2007). Biomechanical models for radial distance determination by the rat vibrissal system. Journal of Neurophysiology 98, 2439-2455.

[11] Bosman, L., Houweling, A., Owens, C., Tanke, N., Shevchouk, O., Rahmati, N., Teunissen, W., Ju, C., Gon, G., Koekkeok, S., et al. (2011). Anatomical pathways involved in generating and sensing rhythmic whisker movements. Frontiers in Integrative Neuroscience 5:53, 10.3389/fnint.2011.00053.

[12] Boubenec, Y., Shulz, D.E., and Debregeas, G. (2012). Whisker encoding of mechanical events during active tactile exploration. Frontiers in Behavioral Neuroscience 6, 16.

[13] Brecht, M., Preilowski, B., and Merzenich, M.M. (1997). Functional architecture of the mystacial vibrissae. Behavioural Brain Research 84, 81-97.

[14] Bush, N.E., Schroeder, C.L., Hobbs, J.A., Yang, A.E.T., Huet, L.A., Solla, S.A., and Hartmann, M.J.Z. (2016). Decoupling kinematics and mechanics reveals coding properties of trigeminal ganglion neurons in the rat vibrissal system. eLife 5, e13969.

[15] Bush, N.E., Solla, S.A., and Hartmann, M.J.Z. (2016). Whisking mechanics and active sensing. Current Opinion in Neurobiology 40, 178-188.

[16] Campagner, D., Evans, M.H., Bale, M.R., Erskine, A., and Petersen, R.S. (2016). Prediction of primary somatosensory neuron activity during active tactile exploration. eLife 5.

[17] Carvell, G.E., and Simons, D.J. (1990). Biometric analyses of vibrissal tactile discrimination in the rat. Journal of Neuroscience 10, 2638-2648.

[18] Charalambides, A., and Bergbreiter, S. (2015). A novel all-elastomer MEMS tactile sensor for high dynamic range shear and normal force sensing. Journal of Micromechanics and Microengineering 25, 095009.

[19] Charalambides, A., and Bergbreiter, S. (2017). Rapid manufacturing of mechanoreceptive skins for slip detection in robotic grasping. Advanced Materials Technologies 2, 1600188-n/a.

[20] Chen, H., Miao, L., Su, Z., Song, Y., Han, M., Chen, X., Cheng, X., Chen, D., and Zhang, H.-X. (2017). Fingertip-inspired electronic skin based on triboelectric sliding sensing and porous piezoresistive pressure detection. Nano Energy 40.

[21] Chernova, O.F. (2003). Architectonic and diagnostic significance of hair cortex and medulla. Biology Bulletin 30, 53-62.

[22] Coste, B., Mathur, J., Schmidt, M., Earley, T.J., Ranade, S., Petrus, M.J., Dubin, A.E., and Patapoutian, A. (2010). Piezo1 and Piezo2 are essential components of distinct mechanically activated cation channels. Science 330, 55-60.

[23] Curtis, J.C., and Kleinfeld, D. (2009). Phase-to-rate transformations encode touch in cortical neurons of a scanning sensorimotor system. Nature Neuroscience 12, 492-501.

[24] Deutsch, D., Pietr, M., Knutsen, P.M., Ahissar, E., and Schneidman, E. (2012). Fast feedback in active sensing: Touch-induced changes to whisker-object interaction. PLoS One 7, 12.

[25] Dong, Y., Mihalas, S., Kim, S.S., Yoshioka, T., Bensmaia, S., and Niebur, E. (2013). A simple model of mechanotransduction in primate glabrous skin. J Neurophysiol 109, 1350-1359.

[26] Ebara, S., Kumamoto, K., Matsuura, T., Mazurkiewicz, J.E., and Rice, F.L. (2002). Similarities and differences in the innervation of mystacial vibrissal follicle-sinus complexes in the rat and cat: A confocal microscopic study. J Comp Neurol 449, 103-119.

[27] Fee, M.S., Mitra, P.P., and Kleinfeld, D. (1997). Central versus peripheral determinants of patterned spike activity in rat vibrissa cortex during whisking. Journal of Neurophysiology 78, 1144-1149.

[28] Gao, P., Bermejo, R., and Zeigler, H.P. (2001). Whisker deafferentation and rodent whisking patterns: behavioral evidence for a central pattern generator. The Journal of Neuroscience 21, 5374-5380.

[29] Gao, P., Ploog, B., and Zeigler, H. (2003). Whisking as a "voluntary" response: operant control of whisking parameters and effects of whisker denervation. Somatosensory & motor research 20, 179-189.

[30] Gibson, J.M., and Welker, W.I. (1983). Quantitative studies of stimulus coding in 1st order vibrissa afferents of rats. 2. Adaptation and coding of stimulus parameters. Somatosensory Research 1, 95-117.

[31] Grant, R.A., Mitchinson, B., Fox, C.W., and Prescott, T.J. (2009). Active touch sensing in the rat: Anticipatory and regulatory control of whisker movements during surface exploration. Journal of Neurophysiology 101, 862-874.

[32] Grant, R.A., Sperber, A.L., and Prescott, T.J. (2012). The role of orienting in vibrissal touch sensing. Frontiers in behavioral neuroscience 6.

[33] Guicrobles, E., Valdivieso, C., and Guajardo, G. (1989). Rats can learn a roughness discrimination using only their vibrissal system. Behavioural Brain Research 31, 285-289.

[34] Haidarliu, S., Golomb, D., Kleinfeld, D., and Ahissar, E. (2012). Dorsorostral snout muscles in the rat subserve coordinated movement for whisking and sniffing. Anatomical Record-Advances in Integrative Anatomy and Evolutionary Biology 295, 1181-1191.

[35] Haidarliu, S., Kleinfeld, D., and Ahissar, E. (2013). Mediation of muscular control of rhinarial motility in rats by the nasal cartilaginous skeleton. Anatomical Record-Advances in Integrative Anatomy and Evolutionary Biology 296, 1821-1832.

[36] Haidarliu, S., Simony, E., Golomb, D., and Ahissar, E. (2010). Muscle architecture in the mystacial pad of the rat. Anatomical Record-Advances in Integrative Anatomy and Evolutionary Biology 293, 1192-1206.

[37] Haidarliu, S., Simony, E., Golomb, D., and Ahissar, E. (2011). Collagenous skeleton of the rat mystacial pad. Anatomical Record-Advances in Integrative Anatomy and Evolutionary Biology 294, 764-773.

[38] Harada, S., Honda, W., Arie, T., Akita, S., and Takei, K. (2014). Fully printed, highly sensitive multifunctional artificial electronic whisker arrays integrated with strain and temperature sensors. ACS Nano 8, 3921-3927.

[39] Hartmann, M.J.Z. (2009). Active touch, exploratory movements, and sensory prediction. Integrative and Comparative Biology 49, 681-690.

[40] Hartmann, M.J.Z. (2015). Vibrissa mechanical properties. Scholarpedia 10, 6636.

[41] Hausman, L.A. (1930). Recent studies of hair structure relationships. Scientific Monthly 30, 258-278.

[42] Hibbeler, R.C. (2014). Mechanics of Materials, 9th edn (Boston: Prentice Hall).

[43] Hill, D.N., Bermejo, R., Zeigler, H.P., and Kleinfeld, D. (2008). Biomechanics of the vibrissa motor plant in rat: rhythmic whisking consists of triphasic neuromuscular activity. The Journal of Neuroscience 28, 3438-3455.

[44] Hill, D.N., Curtis, J.C., Moore, J.D., and Kleinfeld, D. (2011). Primary motor cortex reports efferent control of vibrissa motion on multiple timescales. Neuron 72, 344-356.

[45] Hires, S.A., Pammer, L., Svoboda, K., and Golomb, D. (2013). Tapered whiskers are required for active tactile sensation. Elife 2.

[46] Hires, S.A., Schuyler, A., Sy, J., Huang, V., Wyche, I., Wang, X., and Golomb, D. (2016). Beyond cones: an improved model of whisker bending based on measured mechanics and tapering. Journal of Neurophysiology 116, 812-824.

[47] Hobbs, J.A., Towal, R.B., and Hartmann, M.J.Z. (2015). Probability distributions of whisker-surface contact: quantifying elements of the rat vibrissotactile natural scene. Journal of Experimental Biology 218, 2551-2562.

[48] Hobbs, J.A., Towal, R.B., and Hartmann, M.J.Z. (2016). Evidence for functional groupings of vibrissae across the rodent mystacial pad Plos Computational Biology in press.

[49] Hobbs, J.A., Towal, R.B., and Hartmann, M.J.Z. (2016). Spatiotemporal patterns of contact across the rat vibrissal array during exploratory behavior Frontiers in Behavioral Neuroscience in press.

[50] Hua, Q.L., Liu, H.T., Zhao, J., Peng, D.F., Yang, X.N., Gu, L., and Pan, C.F. (2016). Bioinspired electronic whisker arrays by pencil-drawn paper for adaptive tactile sensing. Advanced Electronic Materials 2.

[51] Huet, L.A., and Hartmann, M.J.Z. (2014). The search space of the rat during whisking behavior. Journal of Experimental Biology 217, 3365-3376.

[52] Huet, L.A., and Hartmann, M.J.Z. (2016). Simulations of a vibrissa slipping along a straight edge and an analysis of frictional effects during whisking. IEEE Transactions on Haptics in press.

[53] Huet, L.A., Rudnicki, J.W., and Hartmann, M.J.Z. (2017). Tactile sensing with whiskers of various shapes: Determining the three-dimensional location of object contact based on mechanical signals at the whisker base. Soft Robotics 4, 88-102.

[54] Huet, L.A., Schroeder, C.L., and Hartmann, M.J.Z. (2015). Tactile signals transmitted by the vibrissa during active whisking behavior. Journal of Neurophysiology 113, 3511-3518.

[55] Iggo, A., and Muir, A.R. (1969). The structure and function of a slowly adapting touch corpuscle in hairy skin. The Journal of Physiology 200, 763-796.

[56] Ikeda, R., Cha, M., Ling, J., Jia, Z., Coyle, D., and Gu, J.G. (2014). Merkel cells transduce and encode tactile stimuli to drive Abeta-afferent impulses. Cell 157, 664-675.

[57] Johnston, I.D., McCluskey, D.K., Tan, C.K.L., and Tracey, M.C. (2014). Mechanical characterization of bulk Sylgard 184 for microfluidics and microengineering. Journal of Micromechanics and Microengineering 24, 035017.

[58] Jones, L.M., Lee, S., Trageser, J.C., Simons, D.J., and Keller, A. (2004). Precise temporal responses in whisker trigeminal neurons. Journal of neurophysiology 92, 665-668.

[59] Kan, Q.H., Rajan, R., Fu, J., Kang, G.Z., and Yan, W.Y. (2013). Elastic modulus of rat whiskers-a key biomaterial in the rat whisker sensory system. Mater Res Bull 48, 5026-5032.

[60] Kaneko, M., Kanayama, N., and Tsuji, T. (1998). Active antenna for contact sensing. IEEE Transactions on Robotics and Automation 14, 278-291.

[61] Khatri, V., Bermejo, R., Brumberg, J.C., Keller, A., and Zeigler, H.P. (2009). Whisking in air: Encoding of kinematics by trigeminal ganglion neurons in awake rats. Journal of Neurophysiology 101, 1836-1846.

[62] Khatri, V., Bermejo, R., Brumberg, J.C., and Zeigler, H.P. (2010). Whisking in air: Encoding of kinematics by VPM neurons in awake rats. Somatosensory and Motor Research 27, 111-120.

[63] Kim, D., and Moller, R. (2007). Biomimetic whiskers for shape recognition. Robotics and Autonomous Systems 55, 229-243.

[64] Kim, S.S., Sripati, A.P., and Bensmaia, S.J. (2010). Predicting the timing of spikes evoked by tactile stimulation of the hand. J Neurophysiol 104, 1484-1496.

[65] Kleinfeld, D., and Deschnes, M. (2011). Neuronal basis for object location in the vibrissa scanning sensorimotor system. Neuron 72, 455-468.

[66] Knutsen, P., and Ahissar, E. (2009). Orthogonal coding of object location Trends Neurosci 32, 101-109.

[67] Knutsen, P.M. (2015). Whisking kinematics. Scholarpedia 10, 7280.

[68] Knutsen, P.M., Biess, A., and Ahissar, E. (2008). Vibrissal kinematics in 3D: Tight coupling of azimuth, elevation, and torsion across different whisking modes. Neuron 59, 35-42.

[69] Knutsen, P.M., Pietr, M., and Ahissar, E. (2006). Haptic object localization in the vibrissal system: behavior and performance. The Journal of neuroscience : the official journal of the Society for Neuroscience 26, 8451-8464.

[70] Leiser, S.C., and Moxon, K.A. (2007). Responses of trigeminal ganglion neurons during natural whisking behaviors in the awake rat. Neuron 53, 117-133.

[71] Lesniak, D.R., Marshall, K.L., Wellnitz, S.A., Jenkins, B.A., Baba, Y., Rasband, M.N., Gerling, G.J., and Lumpkin, E.A. (2014). Computation identifies structural features that govern neuronal firing properties in slowly adapting touch receptors. eLife 3, e01488.

[72] Li, L., Rutlin, M., Abraira, V.E., Cassidy, C., Kus, L., Gong, S., Jankowski, M.P., Luo, W., Heintz, N., Koerber, H.R., et al. (2011). The functional organization of cutaneous low-threshold mechanosensory neurons. Cell 147, 1615-1627.

[73] Li, Q., Li, J., Tran, D., Luo, C., Gao, Y., Yu, C., and Xuan, F. (2017). Engineering of carbon nanotube/polydimethylsiloxane nanocomposites with enhanced sensitivity for wearable motion sensors. Journal of Materials Chemistry C 5, 11092-11099.

[74] Lichtenstein, S.H., Carvell, G.E., and Simons, D.J. (1990). Responses of rat trigeminal ganglion neurons to movements of vibrissae in different directions. Somatosensory & motor research 7, 47-65.

[75] Lottem, E., and Azouz, R. (2011). A unifying framework underlying mechanotransduction in the somatosensory system. The Journal of neuroscience : the official journal of the Society for Neuroscience 31, 8520-8532.

[76] Lottem, E., Gugig, E., and Azouz, R. (2015). Parallel coding schemes of whisker velocity in the rat's somatosensory system. Journal of Neurophysiology 113, 1784-1799.

[77] Lucianna, F.A., Albarracin, A.L., Vrech, S.M., Farfan, F.D., and Felice, C.J. (2016). The mathematical whisker: A review of numerical models of the rat's vibrissa biomechanics. Journal of Biomechanics 49, 2007-2014.

[78] Lumpkin, E.A., and Caterina, M.J. (2007). Mechanisms of sensory transduction in the skin. Nature 445, 858-865.

[79] Maksimovic, S., Nakatani, M., Baba, Y., Nelson, A.M., Marshall, K.L., Wellnitz, S.A., Firozi, P., Woo, S.H., Ranade, S., Patapoutian, A., et al. (2014). Epidermal Merkel cells are mechanosensory cells that tune mammalian touch receptors. Nature 509, 617-621.

[80] Mameli, O., Caria, M.A., Pellitteri, R., Russo, A., Saccone, S., and Stanzani, S. (2016). Evidence for a trigeminal mesencephalic-hypoglossal nuclei loop involved in controlling vibrissae movements in the rat. Experimental Brain Research 234, 753-761.

[81] Mameli, O., Stanzani, S., Mulliri, G., Pellitteri, R., Caria, M., Russo, A., and De Riu, P. (2010). Role of the trigeminal mesencephalic nucleus in rat whisker pad proprioception. . Behavior and Brain Function 6, 1-12.

[82] Mehta, S.B., Whitmer, D., Figueroa, R., Williams, B.a., and Kleinfeld, D. (2007). Active spatial perception in the vibrissa scanning sensorimotor system. PLoS Biology 5, 0309-0322.

[83] Mitchinson, B., Grant, R.A., Arkley, K., Rankov, V., Perkon, I., and Prescott, T.J. (2011). Active vibrissal sensing in rodents and marsupials. Philosophical Transactions of the Royal Society B-Biological Sciences 366, 3037-3048.

[84] Mitchinson, B., Gurney, K.N., Redgrave, P., Melhuish, C., Pipe, A.G., Pearson, M., Gilhespy, I., and Prescott, T.J. (2004). Empirically inspired simulated electro-mechanical model of the rat mystacial follicle-sinus complex. Proceedings of the Royal Society B: Biological Sciences 271, 2509-2516.

[85] Moore, J.D., Lindsay, N.M., Deschenes, M., and Kleinfeld, D. (2015). Vibrissa self-motion and touch are reliably encoded along the same somatosensory pathway from brainstem through thalamus. Plos Biology 13.

[86] Oatis, C.A. (2004). Kinesiology : The mechanics and pathomechanics of human movement (Philadelphia: Lippincott Williams & Wilkins).

[87] O'Connor, D.H., Clack, N.G., Huber, D., Komiyama, T., Myers, E.W., and Svoboda, K. (2010). Vibrissa-based object localization in head-fixed mice. Journal of Neuroscience 30, 1947-1967.

[88] O'Connor, D.H., Hires, S.A., Guo, Z.V., Li, N., Yu, J., Sun, Q.-Q., Huber, D., and Svoboda, K. (2013). Neural coding during active somatosensation revealed using illusory touch. Nature Neuroscience 16, 958-965.

[89] Pammer, L., O'Connor, D.H., Hires, S.A., Clack, N.G., Huber, D., Myers, E.W., and Svoboda, K. (2013). The mechanical variables underlying object localization along the axis of the whisker. The Journal of neuroscience : the official journal of the Society for Neuroscience 33, 6726-6741.

[90] Polley, D.B., Rickert, J.L., and Frostig, R.D. (2005). Whisker-based discrimination of object orientation determined with a rapid training paradigm. Neurobiology of Learning and Memory 83, 134-142.

[91] Price, M.P., Lewin, G.R., McIlwrath, S.L., Cheng, C., Xie, J., Heppenstall, P.A., Stucky, C.L., Mannsfeldt, A.G., Brennan, T.J., Drummond, H.A., et al. (2000). The mammalian sodium channel BNC1 is required for normal touch sensation. Nature 407, 1007-1011.

[92] Quist, B.W., Faruqi, R.A., and Hartmann, M.J.Z. (2011). Variation in Young's modulus along the length of a rat vibrissa. Journal of Biomechanics 44, 2775-2781.

[93] Quist, B.W., and Hartmann, M.J.Z. (2012). Mechanical signals at the base of a rat vibrissa: the effect of intrinsic vibrissa curvature and implications for tactile exploration. Journal of Neurophysiology 107, 2298-2312.

[94] Quist, B.W., Seghete, V., Huet, L.A., Murphey, T.D., and Hartmann, M.J.Z. (2014). Modeling forces and moments at the base of a rat vibrissa during noncontact whisking and whisking against an object. The Journal of neuroscience : the official journal of the Society for Neuroscience 34, 9828-9844.

[95] Ranade, S.S., Woo, S.H., Dubin, A.E., Moshourab, R.A., Wetzel, C., Petrus, M., Mathur, J., Begay, V., Coste, B., Mainquist, J., et al. (2014). Piezo2 is the major transducer of mechanical forces for touch sensation in mice. Nature 516, 121-125.

[96] Reeder, J.T., Kang, T., Rains, S., and Voit, W. (2018). 3D, reconfigurable, multimodal electronic whiskers via directed air assembly. Advanced Materials 30.

[97] Richardson, F. (1909). A study of the sensory control in the rat. The Psychological Review: Monograph Supplements 12, i-124.

[98] Rutlin, M., Ho, C.Y., Abraira, V.E., Cassidy, C., Bai, L., Woodbury, C.J., and Ginty, D.D. (2014). The cellular and molecular basis of direction selectivity of Adelta-LTMRs. Cell 159, 1640-1651.

[99] Simons, D.J. (1978). Response properties of vibrissa units in rat si somatosensory neocortex. Journal of Neurophysiology 41, 798-820.

[100] Simons, D.J. (1985). Temporal and spatial integration in the rat si vibrissa cortex. Journal of Neurophysiology 54, 615-635.

[101] Simony, E., Bagdasarian, K., Herfst, L., Brecht, M., Ahissar, E., and Golomb, D. (2010). Temporal and spatial characteristics of vibrissa responses to motor commands. Journal of Neuroscience 30, 8935-8952.

[102] Solomon, J.H., and Hartmann, M.J. (2006). Robotic whiskers used to sense features. Nature 443, 525-525.

[103] Solomon, J.H., and Hartmann, M.J.Z. (2008). Artificial whiskers suitable for array implementation: Accounting for lateral slip and surface friction. Ieee Transactions on Robotics 24, 1157-1167.

[104] Solomon, J.H., and Hartmann, M.J.Z. (2010). Extracting object contours with the sweep of a robotic whisker using torque information. International Journal of Robotics Research 29, 1233-1245.

[105] Solomon, J.H., and Hartmann, M.J.Z. (2011). Radial distance determination in the rat vibrissal system and the effects of Weber's law. Philosophical Transactions of the Royal Society B-Biological Sciences 366, 3049-3057.

[106] Sripati, A.P., Bensmaia, S.J., and Johnson, K.O. (2006). A continuum mechanical model of mechanoreceptive afferent responses to indented spatial patterns. Journal of Neurophysiology 95, 3852-3864.

[107] Stanic, V., Bettini, J., Montoro, F.E., Stein, A., and Evans-Lutterodt, K. (2015). Local structure of human hair spatially resolved by sub-micron X-ray beam. Scientific Reports 5.

[108] Szwed, M., Bagdasarian, K., and Ahissar, E. (2003). Encoding of vibrissal active touch. Neuron 40, 621-630.

[109] Szwed, M., Bagdasarian, K., Blumenfeld, B., Barak, O., Derdikman, D., and Ahissar, E. (2006). Responses of trigeminal ganglion neurons to the radial distance of contact during active vibrissal touch. Journal of neurophysiology 95, 791-802.

[110] Takahashi-Iwanaga, H. (2000). Three-dimensional microanatomy of longitudinal lanceolate endings in rat vibrissae. J Comp Neurol 426, 259-269.

[111] The, L., Wallace, M.L., Chen, C.H., Chorev, E., and Brecht, M. (2013). Structure, function, and cortical representation of the rat submandibular whisker trident. Journal of Neuroscience 33, 4815-4824.

[112] Towal, R.B., and Hartmann, M.J. (2006). Right-left asymmetries in the whisking behavior of rats anticipate head movements. Journal of Neuroscience 26, 8838-8846.

[113] Towal, R.B., and Hartmann, M.J. (2008). Variability in velocity profiles during free-air whisking behavior of unrestrained rats. Journal of neurophysiology 100, 740-752.

[114] Towal, R.B., Quist, B.W., Gopal, V., Solomon, J.H., and Hartmann, M.J.Z. (2011). The morphology of the rat vibrissal array: A model for quantifying spatiotemporal patterns of whisker-object contact. Plos Computational Biology 7.

[115] Ueno, N., Svinin, M.M., and Kaneko, M. (1998). Dynamic contact sensing by flexible beam. IEEE-ASME Transactions on Mechatronics 3, 254-264.

[116] Vincent, S.B. (1912). The function of the vibrissae in the behavior of the white rat. Animal Behavior Monographs 1.

[117] Voges, D., Carl, K., Klauer, G.J., Uhlig, R., Schilling, C., Behn, C., and Witte, H. (2012). Structural characterization of the whisker system of the rat. IEEE Sensors 12, 332-339.

[118] Wallach, A., Bagdasarian, K., and Ahissar, E. (2016). On-going computation of whisking phase by mechanoreceptors. Nature Neuroscience 19, 487-+.

[119] Walsh, C.M., Bautista, D.M., and Lumpkin, E.A. (2015). Mammalian touch catches up. Current Opinion in Neurobiology 34, 133-139.

[120] Welker, W.I. (1964). Analysis of sniffing of the albino rat. Behaviour 22, 223-244.

[121] Whiteley, S.J., Knutsen, P.M., Matthews, D.W., and Kleinfeld, D. (2015). Deflection of a vibrissa leads to a gradient of strain across mechanoreceptors in a mystacial follicle. Journal of neurophysiology 114, 138-145.

[122] Williams, C.M., and Kramer, E.M. (2010). The advantages of a tapered whisker. PLoS One 5.

[123] Wineski, L.E. (1983). Movements of the cranial vibrissae in the golden-hamster (mesocricetus-auratus). Journal of Zoology 200, 261-280.

[124] Woo, S.H., Lukacs, V., de Nooij, J.C., Zaytseva, D., Criddle, C.R., Francisco, A., Jessell, T.M., Wilkinson, K.A., and Patapoutian, A. (2015). Piezo2 is the principal mechanotransduction channel for proprioception. Nature Neuroscience 18, 1756-1762.

[125] Woo, S.H., Ranade, S., Weyer, A.D., Dubin, A.E., Baba, Y., Qiu, Z., Petrus, M., Miyamoto, T., Reddy, K., Lumpkin, E.A., et al. (2014). Piezo2 is required for Merkel-cell mechanotransduction. Nature 509, 622-626.

[126] Yang, A.E.T., and Hartmann, M.J.Z. (2016). Whisking kinematics enables object localization in head-centered coordinates based on tactile information from a single vibrissa. Frontiers in Behavioral Neuroscience 10.

[127] Yu, Y.S.W., Graff, M.M., Bresee, C.S., Man, Y.B., and Hartmann, M.J.Z. (2016). Whiskers aid anemotaxis in rats. Science Advances 2, e1600716.

[128] Yu, Y.S.W., Graff, M.M., and Hartmann, M.J.Z. (2016). Mechanical responses of rat vibrissae to airflow. The Journal of Experimental Biology 219, 937.

[129] Zhang, J., Hao, L.F., Yang, F., Jiao, W.C., Liu, W.B., Li, Y.B., Wang, R.G., and He, X.D. (2016). Biomimic Hairy Skin Tactile Sensor Based on Ferromagnetic Microwires. Acs Applied Materials & Interfaces 8, 33848-33855.

[130] Zimmerman, A., Bai, L., and Ginty, D.D. (2014). The gentle touch receptors of mammalian skin. Science 346, 950-954.

[131] Zucker, E., and Welker, W.I. (1969). Coding of somatic sensroy input by vibrissae neurons in rats trigeminal ganglion Brain Res 12, 138-.

APPENDIX A

Method of superposition for mass moment of inertia (straight, taper cones with zero tip diameter, two slopes, and a hollow proximal portion)

Here we demonstrate the derivation of the mass moment of inertia using *superposition*. The approach is better suited for whiskers whose shapes are quantified by more than one slope, but it only works for straight whiskers.

This approach was applied in Section 2.2.2 of Methods because the piecewise slopes along whisker length were critical when comparing I_{Mass} for the real whisker against two hypothetical cases without a medulla. The three cases are shown in Fig. 2.4 of the paper.

Computing I_{Mass} for these three cases requires three steps, which are summarized here and then in more detail later in this appendix.

Step 1: We first derive the general expression for I_{Mass} of a cone rotating about the vertical axis at its base, as well as the general expression for I_{Mass} of a cone rotating about a vertical axis at a distance L from its base (Fig. A.1). The cone here and in the rest of the appendix is assumed to have negligible tip diameter.

Step 2: With these two general expressions, we then computed I_{Mass} for the four imaginary whisker sections shown in Fig. A.1b. Section (1) is a cone that represents the outer shape of the whisker, extrapolated as if the proximal taper continued all the way until the radius vanishes to zero. This imaginary whisker section has an extended arc length, S_{Extend}:

$$S_{Extend} = \frac{R_{Base} \cdot S_{Prox}}{(R_{Base} - R_{MedT})} \tag{A.1}$$

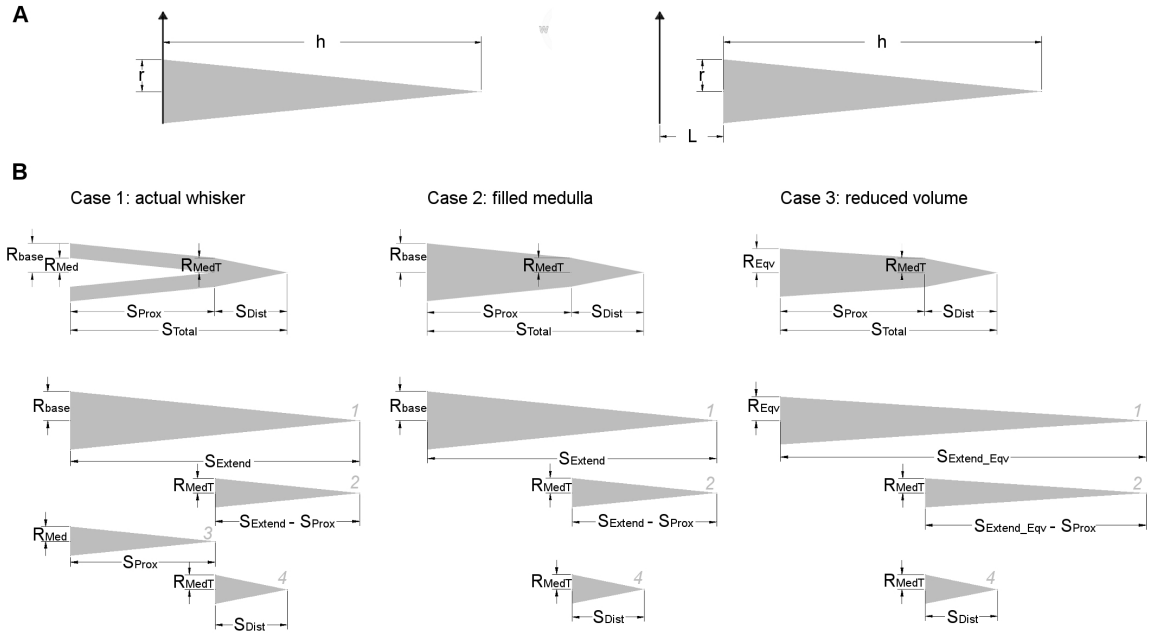

Figure A.1. Calculation of mass moment of inertia using superposition

(A) The first panel shows a schematic of a cone of radius r and length h rotating about its vertical axis at the base. The second panel shows a cone of radius r and length h rotating about its vertical axis at a distance L from the base. In both panels the axis of rotation is shown as a thick arrow. **(B)** The schematics show the geometry of the actual whisker (case 1) along with the hypothetical cases of a "filled medulla" (case 2) and "reduced volume" (case 3). Each case is shown with its corresponding imaginary whisker sections that are combined using superposition to determine the mass moment of inertia.

Section (2) is a cone the same shape as the distal portion of the extended whisker of section (1). Section (3) is a cone the same shape as the medulla. Finally, section (4) represents the distal geometry of the real whisker. Note that Case 3 is different, because we have squashed the whisker, so we end up with an equivalent radius R_{Eqv} and an equivalent extended arc length, S_{Extend_Eqv}]:

$$R_{Eqv} = \frac{1}{2}(-R_{MedT} + \sqrt{(-4R_{Med}^2 + (2R_{Base} + R_{MedT})^2)} \tag{A.2}$$

$$S_{Extend_Eqv} = \frac{R_{Base}S_{Prox}}{R_{Eqv} - R_{MedT})} \tag{A.3}$$

_*Step 3*: With these imaginary whisker sections defined in Fig. A.1b we can see that cases 1 through 3 are composed of the following sections:

$$I_{Case1} = I_1 - I_2 - I_3 + I_4 \tag{A.4}$$

$$I_{Case2} = I_1 - I_2 + I_4 \tag{A.5}$$

$$I_{Case3} = I_{1eqv} - I_{2eqv} + I_4 \tag{A.6}$$

A.1. General expression for I_{Mass} of a cone rotating about the vertical axis at it base, and rotating about the vertical axis at a distance L from its base

According to Hibbeler 2014, the mass moment of inertia of a cone (mass m, base radius r, and height h) rotating about the vertical axis that passes through its tip is:

$$I_{m,tip} = \frac{3}{5}m(\frac{r^2}{4} + h^2) \tag{A.7}$$

The center of mass (CoM) of a cone is $\frac{3}{4}h$ from its tip. Applying the parallel axis theorem and thereby offsetting the axis of rotation back to the COM, we obtain:

$$I_{m,COM} = I_{m,tip} - m\frac{3h}{4}^2 = \frac{3}{5}m(\frac{r^2}{4} + h^2) - \frac{9}{16}mh^2 = \frac{3}{80}m(h^2 + 4r^2) \tag{A.8}$$

Applying the parallel axis theorem a second time, we obtain the mass moment of inertia of a cone rotating about the vertical axis that goes through its base:

$$I_{m,base} = I_{m,COM} + m\frac{h}{4}^2 = \frac{3}{80}mh^2 + \frac{3}{20}mr^2 + \frac{1}{16}mh^2 = \frac{1}{20}m(2h^2 + 3r^2) \tag{A.9}$$

To calculate the mass moment of inertia about an axis at a distance L from the base of the cone:

$$I_{m,LfromB} = I_{m,COM} + m(\frac{h}{4} + L)^2 = (\frac{h}{4} + L)^2m + \frac{3}{80}m(h^2 + 4r^2) \tag{A.10}$$

When written in terms of the density, , the mass of a cone is, by definition:

$$m = \frac{1}{3}\pi r^2 h\rho \tag{A.11}$$

We can thus rewrite equations (A.8), (A.9), and (A.10) in terms of the density:

$$I_{m,COM} = \frac{1}{80}h\pi r^2(h^2 + 4r^2)\rho \tag{A.12}$$

$$I_{m,base} = \frac{1}{60}h\pi r^2(2h^2 + 3r^2)\rho \tag{A.13}$$

$$I_{m,LfromB} = \frac{1}{60}h\pi r^2(2h^2 + 10hL + 20L^2 + 3r^2)\rho \tag{A.14}$$

A.2. Calculating I_{Mass} for the four imaginary whisker sections

We now calculate I_{Mass} for each of the four sections shown in Fig. A.1b. All variables used in the equations that follow are illustrated in Fig. A.1b and are identical to the variables used in the paper.

For each of the four sections, we simply insert the appropriate dimensions (see Fig. A.1a) into the general expressions represented by equations (A.12), (A.13), and (A.14).

$$I_1 = I_{m,base} = \frac{1}{60}S_{Extend}\pi R_{Base}^2(2S_{Extend}^2 + 3R_{Base}^2)\rho \tag{A.15}$$

$$\begin{aligned} I_2 = I_{m,LfromB} = \frac{1}{60}(S_{Extend} - S_{Prox})\pi R_{MedT}^2(2(S_{Extend} - S_{Prox})^2 \\ + 10(S_{Extend} - S_{Prox})S_{Prox} + 20S_{Prox}^2 + 3R_{MedT}^2)\rho \end{aligned} \tag{A.16}$$

$$I_3 = I_{m,base} = \frac{1}{60}S_{Prox}\pi R_{Med}^2(2S_{Prox}^2 + 3R_{Med}^2)\rho \tag{A.17}$$

$$I_4 = I_{m,LfromB} = \frac{1}{60} S_{Dist} \pi R_{MedT}^2 (2S_{Dist}^2 + 10 S_{Dist} S_{Prox} + 20 S_{Prox}^2 + 3R_{MedT}^2)\rho \tag{A.18}$$

For case 3, however, we must use $S_{Extend_{E}qv}$ and R_{Eqv} in equations (A.13) and (A.14):

$$I_{1eqv} = \frac{1}{60} S_{Extend_{E}qv} \pi R_{Eqv}^2 (2S_{Extend_{E}qv}^2 + 3R_{Eqv}^2)\rho \tag{A.19}$$

$$\begin{aligned} I_{2eqv} = \frac{1}{60} (S_{Extend_{E}qv} - S_{Prox}) \pi R_{MedT}^2 (2(S_{Extend_{E}qv} - S_{Prox})^2 \\ + 10(S_{Extend_{E}qv} - S_{Prox}) S_{Prox} + 20 S_{Prox}^2 + 3R_{MedT}^2)\rho \end{aligned} \tag{A.20}$$

A.3. Superposition of I_{Mass} of the four imaginary whisker sections to compute I_{Mass} for each of the three whisker shapes shown in Results

, Now we write out the complete mass moment of inertia equations described in the overview of the calculations (Eq. A.4, A.5, and A.6) and seen in Fig. A.1b for each of the three cases in the analysis.

For case 1, which represents the actual whisker morphology with a medulla, I_{Mass} for rotating about the vertical axis that passes through its base is given by:

$$\begin{aligned} I_{Case1} = \frac{1}{60} \pi (3R_{Base}^4 S_{Extend} + 2R_{Base}^2 S_{Extend}^3 - 3R_{Med}^4 S_{Prox} - 2R_{Med}^2 S_{Prox}^3 \\ + 3R_{MedT}^4 (S_{Dist} - S_{Extend} + S_{Prox}) + 2R_{MedT}^2 (S_{Dist} - S_{Extend} + S_{Prox}) \\ (S_{Dist}^2 + S_{Extend}^2 + 3S_{Extend} S_{Prox} + 6S_{Prox}^2 + S_{Dist}(S_{Extend} + 4S_{Prox})))\rho \end{aligned} \tag{A.21}$$

Furthermore, I_{Mass} for the two hypothetical whiskers (case 2 and case 3) rotating about the vertical axis that passes through its base is given by:

$$\begin{aligned}(A.22)\quad I_{Case2} = \frac{1}{60}\pi(&3R_{Base}^4 S_{Extend} + 2R_{Base}^2 S_{Extend}^3 + 3R_{MedT}^4(S_{Dist} - S_{Extend} + S_{Prox}) \\ &+ 2R_{MedT}^2(S_{Dist} - S_{Extend} + S_{Prox})(S_{Dist}^2 + S_{Extend}^2 + 3S_{Extend}S_{Prox} + 6S_{Prox}^2 \\ &+ S_{Dist}(S_{Extend} + 4S_{Prox})))\rho\end{aligned}$$

$$\begin{aligned}(A.23)\quad I_{Case3} = \frac{1}{60}\pi(&3R_{Eqv}^4 S_{Extend_E qv} + 2R_{Eqv}^2 S_{Extend_E qv}^3 + 3R_{MedT}^4(S_{Dist} - S_{Extend_E qv} + S_{Prox}) \\ &+ 2R_{MedT}^2(S_{Dist} - S_{Extend_E qv} + S_{Prox})(S_{Dist}^2 + S_{Extend_E qv}^2 + S_{Extend_E qv}S_{Prox} \\ &+ 6S_{Prox}^2 + S_{Dist}(S_{Extend_E qv} + 4S_{Prox})))\rho\end{aligned}$$

APPENDIX B

Method of integral for mass moment of inertia (curved, tapered cones with zero tip diameter and one slope) for all three Cartesian axes.

On the other hand, the second approach is recommended when the curvature of the whisker is to be accounted for, but it is only practical to apply when the whisker shape can be illustrated with only one slope. In the end of this appendix we also provide an example to cross compare the approaches in the two appendicesa special case in which both approaches are applicable. We show that solutions from the two approaches– superposition and integral– converge.

B.1. Assumptions of the calculation

The whisker is assumed to be a tapered cone with zero tip diameter, a single linear taper (slope), and a curvature with which the tip of the whisker concaves downward in the negative direction of one of the axis of rotation (z_0-axis), as in Fig. B.1. Because curvature is not neglected, we calculate the mass moment of inertia for all three axes: x_0, y_0 and z_0. There is no curvature in the third dimension ($x_0 - y_0$ plane). The curvature along the longitudinal midline is parametrized by a second-order equation (Eq. B.1), where the coefficient of curvature, A, is constant,

$$z_0(x) = -Ax_0^2 \tag{B.1}$$

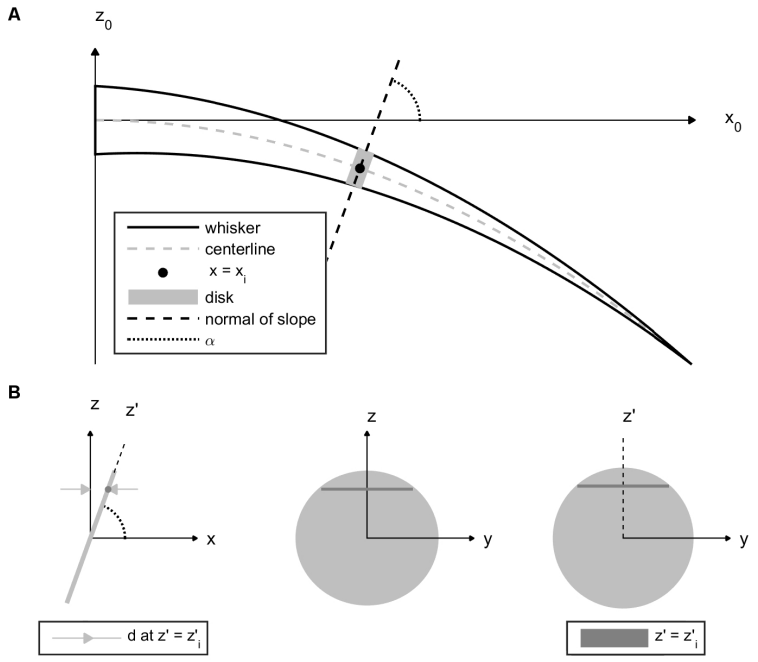

Figure B.1. Calculation of mass moment of inertia using integral
(A) A curved, tapered whisker is divided into thin cross-sections. The whisker shape is enclosed by black solid lines. The curvature of the centerline of the whisker (gray dashed line), is a second-order equation. In this figure the whisker rotates about a vertical axis (z_0) passing through its base. There is one cross-section disk (light gray area) with infinitesimal thickness at every given point (black dot) along the arc length. The direction normal to the slope (black dashed line) and the angle (black dotted line) at which the normal line is tilted from the x-axis are also shown in the figure. **(B)** Three alternative views of (A) are provided. For each cross-sectional disk, the mass moment of inertia is calculated by an area integral over the y-z plane. The integrand of the area integral at any z-location is an infinitesimally thin horizontal bar (darker gray). For rotation about the z_0 axis, the distance d from a given location along the z-axis to the vertical axis (z-axis) is also shown (distance between light gray arrows).

B.2. Dividing the whisker into disks and calculating the I_Mass of each

The integral is formulated by dividing the cone into infinitely many cross-sections with negligible thickness and integrating along the x-axis, where the most proximal segment of the whisker aligns.

A few properties of the tilted disks have to be addressed. First, the radii of the disks, r, vary with arc length. At an arbitrary point along the whisker length, the area of each disk is thus πr^2 and the unit mass is $\rho\pi r^2$, where ρ represents the whisker density. The distances from the centroid of each disk to the whiskers three axes of rotation are z, $\sqrt{(x^2+z^2)}$, and x, respectively. Moreover, by definition, the

tangent of is the slope of the normal (n) of the derivative of a given point along the curve. Therefore, along the curve defined by Eq. B.1, α can be expressed as a function of x given a coefficient constant A, as in Eq. B.2:

$$\alpha(x) = \arctan(-\frac{1}{slope}) = \arctan(-\frac{1}{z'(x)}) = \arctan(-\frac{1}{-2Ax}) = \arctan(\frac{1}{2Ax}) \tag{B.2}$$

Due to the tilt for each disk of a given radius r, we need to construct another integral to derive the mass moment of inertia of each cross-section as a disk tilted at an angle about a vertical axis passing through its centroid. Two critical expressions thus need to be explained.

First, we will formulate a double integral over the variables y and z', which correspond to the two major axes along the plane where the disk lies. Note that z is tilted at an angle $(\pi/2 - \alpha)$ from the z-axis. Also note that r varies with location along the arc length but is independent of y and z'. On the y-z plane, the circle which defines the boundary of the disk can be expressed as $y^2 + z'^2 = r^2$.Therefore, the upper and lower limits for one of the two variables, y, are $\sqrt{r^2 - z'^2)}$ and $-\sqrt{r^2 - z'^2)}$, respectively.

Second, when a disk tilted at an angle, $\alpha(x)$, is divided into infinitesimal horizontal bars parallel to the y-axis, the shortest distance, d, of each bar from the axes of rotation, x-, y-, and z-axes, are $z' \sin(\alpha(x))$, z', and $z' \cos(\alpha(x))$, respectively.

With the two expressions above, we can now integrate to acquire the moment of inertia of each disk, as in Eq. B.3,

$$\begin{aligned} I_{disk,x} &= \int d^2 dm = \rho \int d^2 dA = \rho \int (z'^2 \sin\alpha)^2 dy dz' = \rho \int_{-r}^{r} \int_{-\sqrt{r^2-z'^2}}^{\sqrt{r^2-z'^2}} z'^2 \sin(\alpha)^2 dy dz' \\ &= \rho \int_{-r}^{r} z' 2 \sin(\alpha)^2 (2\sqrt{r^2 - z'^2}) dz' = \left[\frac{1}{4} \rho \sin(\alpha)^2 (z' \sqrt{r^2-z'^2} (-r^2 + 2z'^2) + r^4 \arctan(\frac{z'}{\sqrt{r^2 - z'^2}})) \right]_{-r}^{r} \\ &= \frac{1}{4} \rho \pi r^4 \sin(\alpha)^2 = \frac{1}{4} \rho \pi r^4 \sin(\arctan(\frac{1}{2Ax}))^2 \end{aligned} \tag{B.3}$$

$$I_{disk,y} = \rho \int z'^2 dydz' = \rho \int_{-r}^{r} \int_{-sqrtr^2 - z'^2}^{sqrtr^2 - z'^2} z'^2 dydz' = \frac{1}{4}\rho\pi r^4$$

$$I_{disk,z} = \rho \int (z' \cos(\alpha))^2 dydz' = \rho \int_{-r}^{r} \int_{-sqrtr^2 - z'^2}^{sqrtr^2 - z'^2} z'^2 \cos(\alpha)^2 dydz'$$
$$= \frac{1}{4}\rho\pi r^4 \cos\alpha^2 = \frac{1}{4}\rho\pi r^4 \cos(\arctan(\frac{1}{2Ax}))^2$$

Last but not least, for each disk we apply the parallel axis theorem to calculate the mass moment of inertia at a distance from the axis of rotation passing through the whisker base, as described in Eq. B.4. Recall that the mass of the disk is $\rho\pi r^2$ and the parallel distances of the centroid of the disk from the three axes of rotation are z, $\sqrt{x^2 + z^2}$, and x, respectively.

(B.4)

$$I_{Disk_d,x} = I_{disk,x} + m_{disk}d^2 = \frac{1}{4}\rho\pi r^4 \sin(\arctan\frac{1}{2Ax})^2 + \rho\pi r^2 z^2 = \rho\pi r^2[\frac{1}{4}r^2 \sin(\arctan\frac{1}{2Ax})^2 + A^2x^4]$$

$$I_{Disk_d,y} = I_(disk, y) + m_{disk}d^2 = 1/4r^4 + r^2(x^2 + z^2) = r^2[\frac{r^2}{4} + x^2(1 + (Ax)^2)]$$

$$I_{Disk_d,} = I_{disk,z} + m_{disk}d^2 = \frac{1}{4}\rho\pi r^4 \cos(\arctan\frac{1}{2Ax})^2 + \rho\pi r^2 x^2 = \rho\pi r^2[\frac{1}{4}r^2 \cos(\arctan\frac{1}{2Ax})^2 + x^2]$$

B.3. Additional steps to set up the integral of disks over the whole whisker length

A2.3 Additional steps to set up the integral of disks over the whole whisker length Even though we have calculated the unit mass moment of inertia of each cross-section, within the expression remains the variable r, which should be substituted with a function of x in order to calculate the integral with respect to x. There are thus a few additional steps before the integral is set up over the length of the whisker.

While the integral will be calculated with respect to x, in the present work, whisker geometry was experimentally quantified by arc length, which curves out of the x-axis. As a result, we need to derive the relationship between a whiskers x-coordinate and arc length, $L(x)$, shown in Eq. B.5.

$$L(x) = \int_0^x \sqrt{1 + z'(x)^2}dx = \int_0^x \sqrt{1 + (2Ax)^2}dx = \frac{1}{2}x\sqrt{1 + 4A^2x^2} + \frac{arcsinh(2Ax)}{4A} \tag{B.5}$$

The cross-sectional radius of the whisker, r, is now going to be expressed in terms of $r(L)$, as a function of arc length $L(x)$ at a given location, and eventually $r(L(x))$, as a function of x at that location.

When the base diameter of the whisker is R_{Base} and the total arc length is S_{Total}, the radius $r(L)$ at a given point L along the arc length can be found by Eq. B.6

$$r(L) = R_{Base} - \frac{R_{Base}L}{S_{Total}} \tag{B.6}$$

Substituting L in Eq. B.6 with Eq. B.5,

$$r(x) = R_{Base} - \frac{R_{Base}}{S_{Total}}[\frac{1}{2}x\sqrt{(1 + 4A^2x^2)} + \frac{arcsinh(2Ax)}{4A}] \tag{B.7}$$

Furthermore, substituting r(x) in Eq. B.7 into Eq. B.4, the I_{Disk_d} for all three directions can now be functions of only x.

B.4. Integrating unit cross-sectional I_{Mass} over the entire whisker

Now that we have the expression for unit mass moment of inertia, $I_{Disk_d}(x)$, as a function of solely one variable, x, the limits of the integral can then be set from whisker base ($x = 0$) to tip ($x = x_f$). The upper limit, x_f, can be solved numerically from Eq. B.5 when x and L are substituted with x_f and S_{Total}, respectively.

By integrating the unit mass moment of inertia with respect to x, I_{Mass} of the entire whisker can be found,

$$I_{Mass}(x) = \int_0^{x_f} I_{Disk_d}(x)dx \tag{B.8}$$

Mathematica^{TM}was unable to solve for an analytic expression of the solution to the equation immediately above (Eq. B.8). Nevertheless, the same software is capable of obtaining a numerical solution.

B.5. Convergence of a whiskers two mass moments of inertia (I_{Mass}) derived using two different approaches

To cross-compare results calculated using one approach versus the other, we define an example whisker. The whisker has negligible curvature, one linear slope, and no medulla, ensuring both approaches are applicable.

The parameters that define the geometry of the example whisker are: curvature coefficient $A << 1mm^{-1}$ (note that the integrand would be non-existent by definition if A is exactly zero), density $= 1mg/mm^3$, arc length $S_{Total} = 35mm$, and base diameter $R_{Base} = 0.1mm$. The mass moment of inertia calculated using the superposition approach (Appendix A) yields 44.8986 while the integral approach (Appendix B) yields 44.8991 for z-axis, 44.8986 for y-axis, and 1.57×10^{-34} for x-axis. The relative error between the two approaches is smaller than 0.00012%.

Furthermore, we performed a sensitivity analysis on the error to the variation in R_{Base} and S_{Total} between superposition and integral approaches. Within a reasonable scale, the error increases as R_{Base} increases and/or as S_{Total} decreases. The growth in error with the increment and decrement of the two parameters is expected because the "chunkier" a whisker is, the more likely numerical errors are going to arise when an integral is applied; the whisker volume is divided longitudinally, and each cross-sectional sliced is approximated to be uniform.

Generally, for a curved whisker, the smallest among all three IMass is about the x-axis, since it has the least amount of material spread out from the axis of rotation. IMass about y-axis is bigger than that about z-axis because the distance of a given point mass along the whisker from y-axis is $\sqrt{x^2 + z^2}$ and, from z-axis, x.

APPENDIX C

Beam bending of a Maltese cross subject to a concentrated load under different boundary conditions

This document compares beam deflections from a concentrated load under two different boundary conditions– clamped on one end vs. clamped on both ends. The purpose of such comparison is to demonstrate the necessity of simultaneously considering the two opposing arms on a Maltese cross to reverse-engineer external forces from strains.

C.1. Background

Maltese cross has been part of the macro sensor developed by the Hartmann lab to quantify whisker base mechanics (Emnett et al., submitted to Robotics: Science and Systems, 2018). Here, a Maltese cross is a thin piece of elastic material in the shape of a cross, all of whose "arms" have equal lengths and constant widths. With the four ends of the cross clamped and a whisker mounted perpendicularly at the center of the cross, strain gages on the arms yields electrical signals when the whisker exerts an axial force and in turn deforms the Maltese cross. Signals are then post-processed to quantify the mechanics.

Strain gages are typically set up in a Wheatstone bridge. In a half bridge, for example, voltage outputs from two points in the circuit– between two strain gages of resistances R_1 and R_2, and between two reference resistances R_3 and R_4. The two strain gages, are mounted on the top and bottom surfaces of an arm, respectively, to compensate environmental noise such as temperature difference. Both strain gages havea gage factor of GF. The output voltage observes the following equation,

$$V_{out} = [\frac{R_3}{R_3 + R_4} - \frac{R_2(1 + \epsilon_{bottom}GF])}{R_1(1 + \epsilon_{top}GF]) + R_2(1 + \epsilon_{bottom}GF])}]V_{in} \tag{C.1}$$

When $R_1 = R_2$ and $R_3 = R_4$, equation (C.3) can be rewritten as follows,

$$V_{out} = [\frac{1}{2} - \frac{(1 + \epsilon_{bottom} GF])}{(1 + \epsilon_{top} GF]) + (1 + \epsilon_{bottom} GF])}]V_{in} \tag{C.2}$$

Theoretically, $\epsilon_{top} = -\epsilon_{bottom}$,

$$V_{out} = [\frac{1}{2} - \frac{(1 + \epsilon_{bottom} GF])}{2}]V_{in} = -\frac{\epsilon_{bottom} GF}{2} V_{in} \tag{C.3}$$

Currently implemented calculation in post-processing treats each one of the four arms independently. Nevertheless, all four arms are structurally interconnected. In this document we aim to demonstrate the interactions between two arms at opposing positions. Future work will then investigate the collective responses of all four arms.

C.2. Clamped on one end

A single arm of the Maltese cross is a beam with a length of $L/2$, Young's modulus of E, and area moment of inertia of I. The x-axis is defined along the length of the beam, and the y-axis along the whisker length. The beam is clamped on one end ($x = 0$) and free at on the other ($x = L$). After an external load F is exerted at the free end perpendicular to the length of the beam. We seek to quantify the strain ϵ at ($x = L/2$), the location where a strain gage is mounted in experiments. According to Euler-Bernoulli beam theory, the strain at any point is the product of the y-distance c of the point from neutral axis and the beam's longitudinal curvature (Hibbeler 2014), which can be approximated as $y''(x)c$. In this analysis, c is a constant since we are solving for the strains at the top of the beam.

Based on existing lookup tables in Hibbeler 2014, the y-deflection of the beam is the following function of x,

$$y(x) = \frac{Fx^2}{6EI}(\frac{3}{2}L - x) \tag{C.4}$$

Taking the derivative of equation (C.4) twice,

$$y''(x) = \frac{F}{EI}(\frac{L}{2} - x) \tag{C.5}$$

Euler-Bernoulli theory describes local bending moment $M(x)$ as,

$$M(x) = EIy''(x) \tag{C.6}$$

Strain is therefore in the following relationship with local bending moment $M(x)$, E, I, and c,

$$\epsilon(x) = y''(x)c = \frac{M(x)c}{EI} = \frac{F(L-2x)c}{2EI} \tag{C.7}$$

At $x = L$, $x = L/2$, and $x = 0$,

$$\epsilon(0) = \frac{FLc}{2EI}, \quad \epsilon(\frac{L}{4}) = \frac{FLc}{4EI}. \quad \epsilon(\frac{L}{2}) = 0 \tag{C.8}$$

The strain ϵ as a function of x is shown as the dashed line in Fig. C.2.

C.3. Clamped on both ends

Two opposing arms, each of length $L/2$ and the same material and geometric properties as in section C.2, has the following y-deflection function and second-derivative. Note that the external force here is of magnitude $2F$.

$$y(x) = \frac{2Fx^2}{48EI}(3L-4x), \quad y''(x) = \frac{2F}{8EI}(L-4x) \tag{C.9}$$

The strain can then be described as

$$\epsilon(x) = \frac{F(L-4x)c}{4EI} \tag{C.10}$$

At critical locations along the beam, the strains are as follows,

$$\epsilon(0) = \frac{FLc}{4EI}, \quad \epsilon(\frac{L}{4}) = 0, \quad \epsilon(L/2) = -\frac{FLc}{4EI} \tag{C.11}$$

The strain ϵ as a function of x is shown as the solid line in Fig. C.2.

The most important finding here is that strain is zero at the location where strain gages are typically mounted ($x = L/2$). The finding makes physical sense because the slope at whisker mounting location

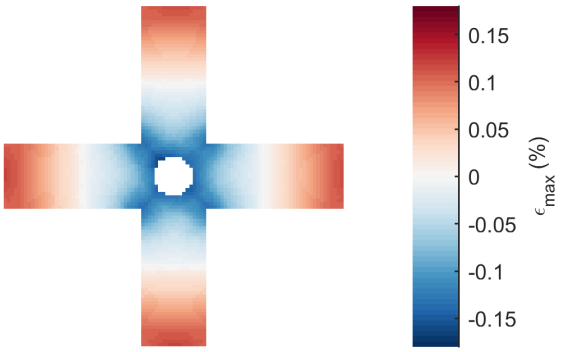

Figure C.1. Abaqus output of maximum principle strain (ϵ_{max}) of a Maltese cross under axial force

($x = L/2$) must be zero to form a symmetry between two arms about the y-axis to fulfill the geometric compatibility condition. Symmetry between two arms also means the displacement between two halves of each arm (0 to $L/4$ and $L/4$ to $L/2$)must be symmetric about the x-axis. The zero strain can sound counter-intuitive because displacements and deflections are often times mistaken as the same quantity when they are actually not.

In addition to analytical derivation, a simulation was run on Abaqus CAE– SIMULA^{TM}by Dassault Systmes®. The resultant maximum principle strain (ϵ_{max}) distribution is visualized in Fig. C.1. The distribution of strain along the length of each arm is in line with the analytical results (solid line in Fig. C.2).

C.4. Comparison between two boundary conditions

We next compare the strains (Fig. C.2) and deflections (Fig. C.3) as the result of the two boundary conditions. Under the same applied load P, the "clamped-free" boundary condition (section C.2) yields a base strain of $\epsilon(0) = \frac{FLc}{2EI}$. In contrast, the "clamped-clamped" boundary condition (section C.3) yields a base strain of $\epsilon(0) = \frac{FLc}{4EI}$. The magnitude of the latter is a half of that of the former. Moreover, assuming that the beam is clamped on both sides resulted in a negative tip strain, meaning that the material is under compression locally.

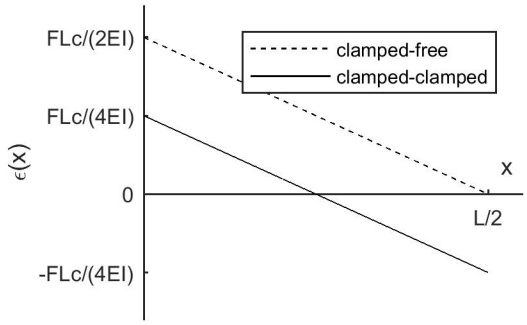

Figure C.2. Strains as a function of x-location under two different assumptions.

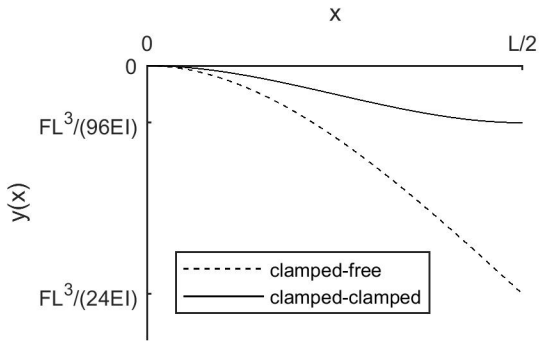

Figure C.3. Deflections as a function of x-location under two different assumptions.

The deflections calculated based on the two boundary conditions are shown in Fig. C.3. The two maximum deflections are different by a factor of four.

C.5. Conclusion

This document derived equations to describe the strains of a beam under two different boundary conditions. These equations showed that considering two opposing arms as independent leads to over-estimation of the maximum strains and the deflected shape. More crucially, considering both arms as dependent, the strain distribution of a beam fixed on two ends suggests that in order for a strain gage to experience strains it should not be mounted perfectly at the center along the longitudinal direction of an arm.